POLITECHNIKA LUBELSKA

Application of Computational Methods in Engineering Science

redakcja
Mirosław Szala
Katarzyna Falkowicz

MONOGRAFIE

Lublin 2019

Application of Computational Methods in Engineering Science

Monografie – Politechnika Lubelska

Politechnika Lubelska
Wydział Mechaniczny
ul. Nadbystrzycka 36
20-618 LUBLIN

Application of Computational Methods in Engineering Science

redakcja:
Mirosław Szala
Katarzyna Falkowicz

Wydawnictwo Politechniki Lubelskiej
Lublin 2019

Recenzent:
prof. dr hab. inż. Jerzy Lipski, Politechnika Lubelska

Publikacja wydana za zgodą Rektora Politechniki Lubelskiej

© Copyright by Politechnika Lubelska 2019

ISBN: 978-83-7947-385-4

Wydawca: Wydawnictwo Politechniki Lubelskiej
www.biblioteka.pollub.pl/wydawnictwa
ul. Nadbystrzycka 36C, 20-618 Lublin
tel. (81) 538-46-59

Elektroniczna wersja książki dostępna w Bibliotece Cyfrowej PL www.bc.pollub.pl

SPIS TREŚCI

Dominik Rybarczyk[1], *Andrzej Milecki*[2]

OBJECT RECOGNITION SYSTEM USING DETACHABLE-ANTENNA RFID PASSIVE TAGS

Keywords: public transport, seats occupancy, RFID, passenger localisation

Abstract

This paper describes the design of a new type of sensors used to check the presence of passengers in vehicles. The system was built based on UHF RFID tags. An ultra-high frequency (UHF) RFID technology allows reading tags from a long range. Each sensor is equipped with detachable antennas. Upon loading with a force generated by the mass of the passenger sitting down, the switch closes the antenna to RFID electronic circuit and the tag is picked up by the receiver. The key advantage of the invention is battery-lessness, which significantly increases its reliability and ease of implementation. The prototype of the sensor was built by the author and tested. The author was granted a patent no. P.419576 on the invention described in this paper.

1. Introduction

The first patent for an active Radio Frequency IDentification (RFID) solution was granted in the USA at the beginning of 1973. That solution incorporated tags with rewritable memory [1]. In the same year, a patent for a passive transponder for remote keyless system was assigned. In the 1980s the commercial expansion of the RFID technology was taking over Europe and the USA, starting with transportation systems for animals tracking. In 1990s RFID was already widely used by many companies. As a result, some standards in this area began to shape. Since the 2000s the RFID technology has been actively enhanced and improved, leading to miniaturisation and price reduction. Today RFID systems are found in many indoor applications for direct identification and tracking of products and in production and transport. In this technology, the data are stored in electronic RFID tags and can be repeatedly and wirelessly read, thus enabling products or devices to be identified in real-time.

Passive tags do not rely on batteries or power sources to operate. When a tag is in the range of a magnetic or electric field, generated by the RFID reader, the tag receives the power to transmit its data to the reader. This is an important advantage of the passive technology over its active counterparts, which require access to a power source. RFID tags (transponders) are small communication

[1] Poznan University of Technology, Institute of Mechanical Technology, Skłodowska-Curie Square 5, 60-965 Poznań, Poland, dominik.rybarczyk@put.poznan.pl

[2] Poznan University of Technology, Institute of Mechanical Technology, Skłodowska-Curie Square 5, 60-965 Poznań, Poland, andrzej.milecki@put.poznan.pl

devices in which desired information can be stored. They may have a different form, e.g. stickers (labels), tokens or rivets. The RFID tag consists of a dedicated integrated circuit and an antenna. There are LF, HF (13.56 MHz) and UHF (868 – 950 MHz) passive RFID systems, whose common feature is that they use magnetic coupling to transfer power and data. The type of coupling determines data rate, reading distance and environmental robustness. A special group called UHF RFID readers (ultra-high frequency RFID), denotes products with extended signal reading distance. This passive system consists of RFID transmitters (also known as transponders, labels, RFID tags) and an RFID reader equipped with an antenna. The RFID system works as follows:

- the reader generates a high electromagnetic wave using an antenna transmitter,
- the electromagnetic wave is read out by the tag using an independent antenna and converted to DC voltage which is used to charge the capacitor,
- using the capacitor's energy the tag generates the electromagnetic wave which transmits the requested data recorded in a tag to the reader,
- the received signal is obtained by a reader, filtered and decoded.

In the literature, the applications of RFID technology for localisation are also described. Most of them are based on trilateration and triangulation. The distance and angles between the reader and tag are necessary to know (in these methods). M. Bouet et al. [2] proposed a classification and survey of RFID application for localisation and positioning, including future trends in this domain.

A modified trilateration method applied in passive RFID indoor localisation system is presented by Savochkin [3]. Thanks to his trilateration method the training stage of measurement data collection was excluded. The modification uses a simple linear model of the distance v measurement data function, which enables to improve the localisation accuracy.

In a different study, a simple, low-frequency RFID-based localisation method was investigated with respect to measuring the RFID tags position recognition accuracy in the function of the reader velocity [4]. The RFID reader was installed on a small Cartesian robot. Two methods/paths of robot head movements were examined. The investigations showed that the measurements precision error was approx. ±2 mm.

2. RFID systems in vehicles

In modern public transport i.e. buses, coaches or trains, to ensure the optimal cost-effective control of devices such as the air conditioning system (HVAC), it is necessary to detect the number and position of passengers i.e. occupancy of seats by passengers. The producers are looking for cheap and energy-saving sensors mounted in the seats, which can be used for this purpose. Nowadays, the simplest and most commonly seat occupancy detection technology is the mat with piezoelectric sensors. The mats can work as simple on/off switches or as a pressure measurement element. In the latter case, the system may be able to distinguish an adult passenger from a child. In this sensor, a few piezoresistive elements were placed on the surface of the membrane and connected together [5].

Another seat occupancy detection solution employs capacity switches mounted on the seat. There are a number of methods to measure the capacitance between an electrode and its surroundings. The investigations to detect whether or not a seat is occupied have proven to be reliable with low power consumption. Therefore, this solution is suitable for the automotive industry. The capacitive occupancy detection sensors are used for airbag systems and for monitoring of drivers' vital signs. However, the capacitance sensor must be powered from a special capacity measurement system controller by use of a dedicated electronic unit. This unit requires an external power supply.

Because of problems with the supply of energy to the seats of public transport vehicles, engineers are trying to limit the amount of on-board wiring by equipping each sensor with an independent battery. It is also, expected that the data from the sensor will be transmitted wirelessly. If the sensor and its communication unit is supplied by the battery and assuming that the typical passenger seat is used for approx. 10-15 years, the capacity of the battery becomes a huge problem. In addition, the battery life is affected by different factors such as the effect of low temperature. Additionally, the battery-equipped sensor requires a proper service procedure for dismounting from a seat. For this reason, it is necessary to find new methods addressing these disadvantages.

A broad survey and examination of approaches proposed by scientists and companies for different applications of RFID systems is given in the work by Juels [6], which focuses on the privacy protection and integrity assurance in RFID systems. Onsemi company [7] proposed a solution that uses an RFID sensor in the passenger seat. The system allowed the passenger detection and weight measurement based on loading measurement. The sensor was referred to as a smart, passive device, however the type of reader was not specified. The study by Lima Fereira et al. [8] concerns a system for detecting the number of passengers in a vehicle using RFID cards. Also, in this solution, the unit does not include the use of detachable sensors. It was assumed that each passenger is equipped with their own card. The paper also describes the flow of information from the transport system. RFID transponders are the subject of numerous patents [9]. In one of the designs that transponders are mounted directly in the passenger seats. The detection is carried out using a pressure sensor and the force is transmitted by means of an elastomeric tank. Another patented technology is a passenger detection system based on the temperature model [10]. The system is battery-powered and is composed of pressure sensors, CO_2 sensors and microwave sensors.

In the solution developed at MIT [11], a special card had the ability to disconnect from the antenna, due to the power generated at the time of sitting down. The switch was controlled at the press of a button. The system is directed to mobile solutions (cards). There is no reference to sitting in the vehicle. The patent presented in the application [12] concerns belt fastening verification, and thus the presence of a child in a seat intended for them. The detection is performed by changing the parameters of the coil and thus the resonance circuit. Another patented solution [13] presents an RFID module implemented in the door of the vehicle. Opening the door is correlated with the button that opens the antenna contacts. The patent has no reference to the position of a passenger.

Systems for the identification of passengers on aircraft have also been developed [14, 15]. Devices described in [14] are based on RFID technology, but implemented a different way of identification. Finally, the patent filed by Meckesheimer et al. [16] described dynamic seat labelling and passenger identification system. The system based on the special placard for displaying customer-specific messages includes a receiver, a capacitor, and an electronic updateable static display. As compared to the solutions mentioned above, the system described in this paper is based on RFID tag with a detachable antenna.

3. The proposed system structure

Our solution enables load detection, it is the load that generates the force, e.g. the force of gravity. The system is presented in figure 1. Its crucial element is the RFID tag connected to an antenna. The connection broken and can be connected when the force, e.g. the gravity force, acts on the monostable switch. When the force is generated, the RFID tag sends a response to the reader. If there is no load above the sensor, the tag does not respond the reader. The most important advantage of the proposed solution is that the sensor does not require any power supply, which significantly increases its reliability and ease of use.

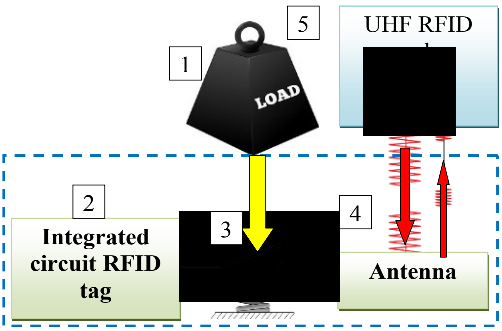

Fig. 1. The illustration of the proposed solution for load presence recognition by RFID tag with detachable antenna

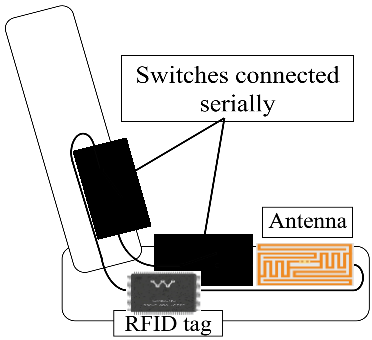

Fig. 2. Application of RFID tag in a vehicle seat

This solution may be used in many applications, such as the one considered in this paper, is the passenger presence detection on the seat of a bus, tram or other public transport vehicles. The design of the system of RFID tag-based sensor in a vehicle seat is presented in figure 2 and in figure 3. If not, the system warns the passenger and informs the staff about it.

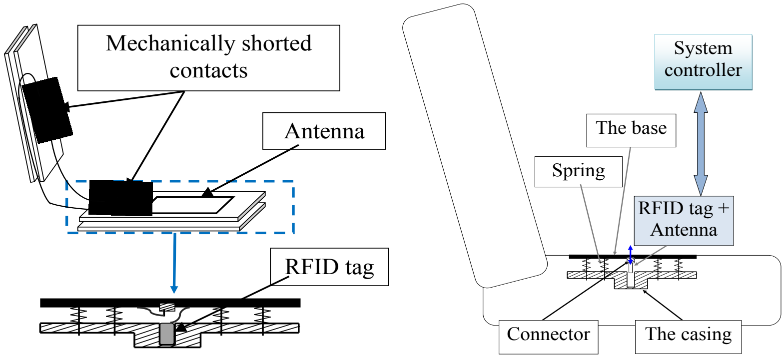

a) b)

Fig. 3. Location and system for seat occupancy detection design

The proposed solution consists of the RFID tag installed in the passenger seat and a UHF RFID reader with a built-in antenna. This type of reader handles multiple tags at the same time. The operating range for passive UHF RFID sensors is between 5 m and 15 m. In order to recognise individual RFID transceivers in the seats, in each of them different numbers (data) should be previously stored in the memory.

Every sensor consists of an RFID tag (integrated circuit – chip) connected with an antenna on contact. If the contact is not mechanically activated, which means that passenger is not present in the seat, it is open and the RFID circuit is not connected to the antenna and the RFID chip cannot communicate with the UHF reader.

When the passenger takes a seat, the gravity force causes closes the contact, thus switching it to. ON. In this state the antenna is connected to the RFID chip, which communicates with the reader in order to send the number of the occupied seat. In order to distinguish whether the place is occupied by a passenger or there is luggage on it, two contacts connected serially may be used, as shown in figure 2 and figure 3a. Alternatively, the antenna could be physically shortened by the contact activated by the passenger taking a seat. Additionally, the contact may be activated using a mechanical gear or mechanical switch, at the moment when the passenger sits on the seat. So, if the seat is occupied, the sensor is "visible" to the reader. The reader is connected to the master vehicle control system. In the developed solution, the base of the sensor (figure 3b) is made of durable non-ferromagnetic material e.g. ABS. The base moves when the passenger sits down. In the passenger seat, this base is assembled on a spring, which is placed in guideways. The casing was made of ferromagnetic material. The important advantage of the proposed solution is the low price of passive RFID tags.

4. Test set-up description

The test set-up incorporated the UHF RFID reader type PWSK 4MR connected to the PC computer via the RS232 interface (figure 4). For communication, the authors wrote a dedicated application in C# language using also, Visual Studio software. It enabled establishing a connection with the receiver, configuring its basic operating parameters and reading the RFID tag ID number. Additionally, the RSSI signal strength, number of counted tags and list of all tags located in the working space, can be displayed on the screen (see figure 5). The reading base time was 50 ms. The RFID reader enabled simultaneous counting of up to 100 tags.

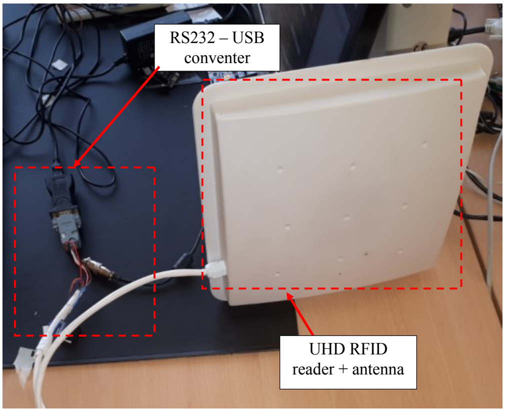

Fig. 4. Test stand structure

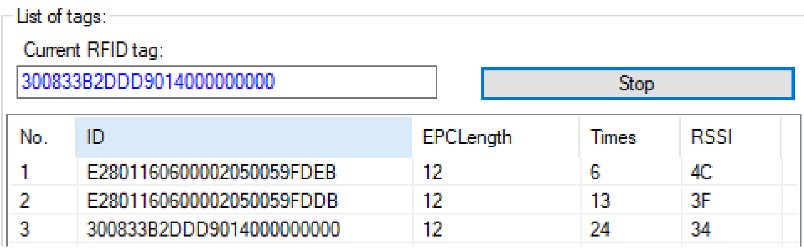

No.	ID	EPCLength	Times	RSSI
1	E2801160600002050059FDEB	12	6	4C
2	E2801160600002050059FDDB	12	13	3F
3	300833B2DDD9014000000000	12	24	34

Fig. 5. View from the written application to read data from sensors

The basic parameters of the receiver are summarised in table 1. From the point of view of its use, it is important to have a large signal gain, a compact design (antenna mounted inside the receiver) and a large signal gain that can be configured. The sensor prototype was built on the RFID tag (figure 6). It was modified by cutting off the antenna and soldering a monostable switch with a wire of about 100 mm length, thus becoming a new antenna. The length of the wire antenna was roughly calculated using the work [17]. Closing the contact (short circuiting) and opening it triggers the connection or disconnection of the antenna. As a result, the RFID tag is visible or not by the reader.

Tab. 1. RFID reader parameters

Parameter	Description
RFID protocol	EPC C1 GEN2, ISO18000-6B / 6C
Reader amplification	0-30 dB
Operating frequency	865 - 868 MHz
Antenna gain	8dBi
Polarisation of the antenna	linear
Communication interface	RS232, RS485
Leakproofness	IP55
Working temperature	-10C to 55C

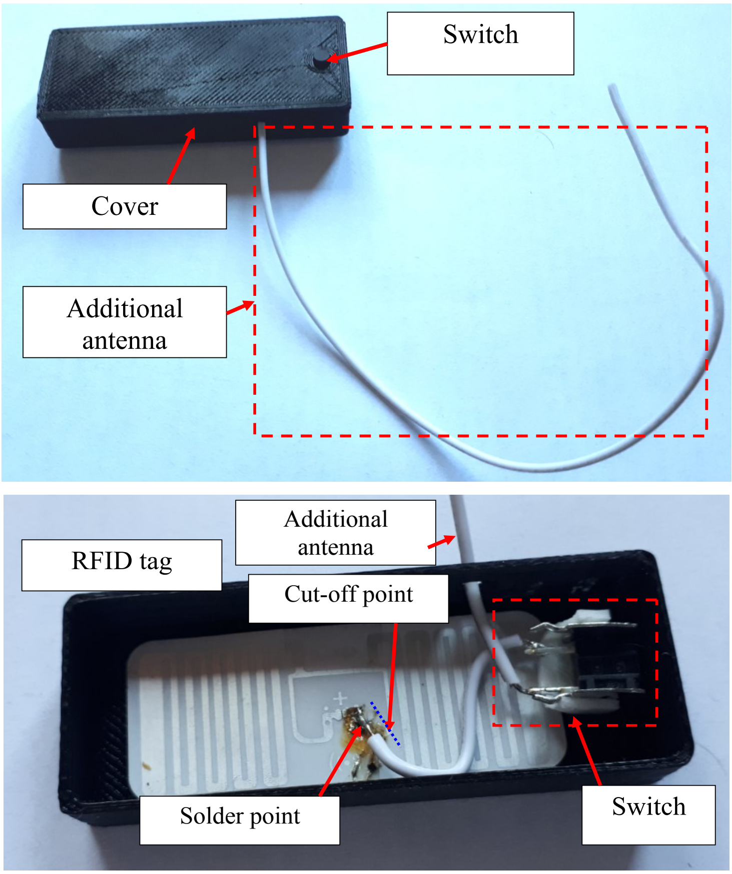

Fig. 6. View of the built prototype sensor

5. Experimental test

In order to verify the proposed solution, experimental tests were performed. At first, the range of operation for the original RFID tag and the modified RFID tag with an added antenna was checked. The results are collected and presented in figure 7. The signal quality was verified by means of the Received Signal Strength Indication (RSSI) value. For this article, a higher RSSI value meant better signal quality. The modified sensor was characterised by a larger gain, but its operating range (distance) was shortened from approx. 8.5 m to 5 m. It was most likely caused by the very simple shape and length of the additional antenna, which was a straight wire.

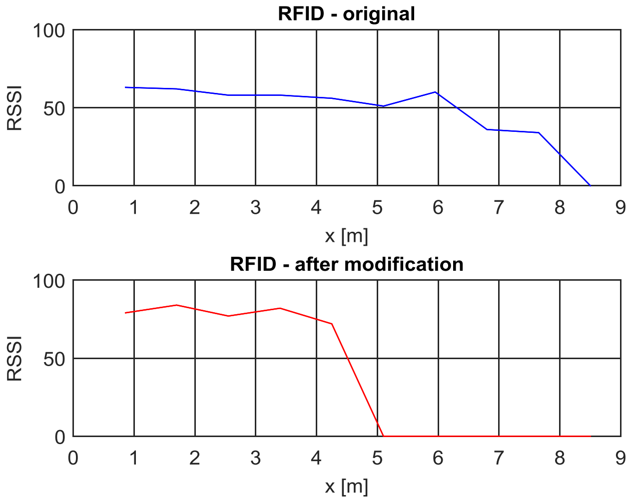

Fig. 7. Signal quality of the sensors after and before modification

In the second test, the signal quality was verified while maintaining a constant distance from the receiver. The results, presented in figure 8, showed that the RSSI parameter was higher for modified RFID. The change in the RSSI parameter results from the modified shape and length of the antenna in the modified tag. This parameter results from dependencies [18]:

$$P_T = \frac{P_{RWD} \cdot G_r \cdot G_t \cdot \lambda^2 \cdot \tau \cdot \chi}{(4\pi r^2)}$$

where: P_t – power received in the antenna identifier, P_{rwd} – power supplied to the terminals of the impedance matching antenna, G_r – gain of the impedance – matched antenna, G_t – the gain of the transponder antenna (the module – base and antenna impedance matching is assumed), χ – the polarisation matching factor for a given arrangement of radio communications antennas, λ – wavelength, r – distance between antennas, τ – the coefficient of power transfer from the antenna to the chip.

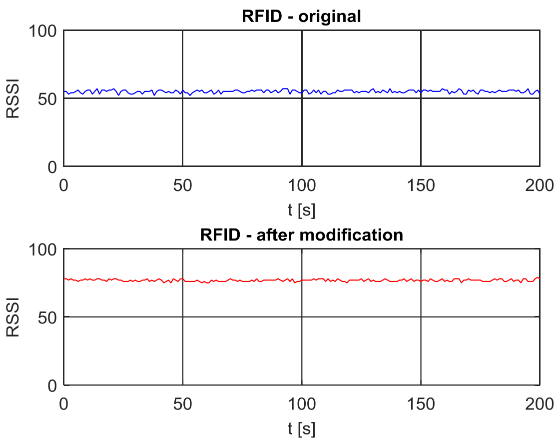

Fig. 8. Signal quality of the sensors after and before modification

In the last test reported in this paper, the complete system for passenger detection is validated. The recorded output signal from the reader is shown in figure 9.

In comparison to the original antenna, the new one had a greater length. This resulted in an increase of the signal gain to about 70%, which can be seen in the waveform. Nevertheless, the system worked properly and the quality of the signal didn't change significantly. The performed tests confirmed the initial assumptions. They were repeated several times and all the results are satisfactory.

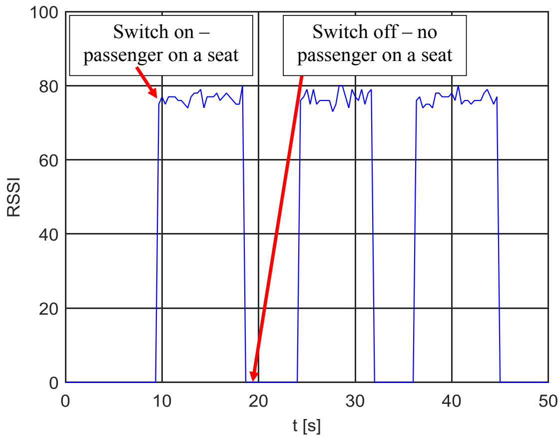

Fig. 9. Operation of the switch together with RFID sensor

6. Experimental test

The new application of RFID tag presented here can be successfully used in various scenarios when detecting elements which generate low force, e.g. gravity forces. In this paper, the application of such a sensor for seat occupancy detection in modern vehicles, such as buses, coaches or trains is proposed. The system provides information not only about the number of passengers but also, about their location. The most important advantage of this solution is that there is no need to use any additional power supply or wiring, which would be highly problematic in vehicles. There is no need to use batteries that are discharge and require replacement. The system with such a sensor may be used to check whether the passenger has a seatbelt fastened (with additional RFID sensor). After exceeding the specified passenger weight (approx. 20 kg), due to the microswitch used in the sensor, small movements of the passenger in the seat should not caused accidental disconnection of the system

The system could also, prove useful in production plants to verify the location of employees. Increasing reliability of readings and verification, could allow the driver to determine whether the seat is occupied by the passenger or his luggage. The author was granted a patent no. P.419576 on the invention described in this paper.

Acknowledgements

This work was supported by Polish Ministry of Science and Education grants no. 02/22/DSPB/1432.

References

[1] R. Want, "An introduction to RFID technology", *IEEE Pervasive Computing*, vol. 5(1), pp. 25–33, 2006.

[2] M. Bouet, L. Aldri dos Santos, "RFID Tags: Positioning Principles and LocalizationTechniques", *IEEE Explore, 1st IFIP Wireless Days*, Dubai, 2008.

[3] D.A. Savochkin, "Simple Approach for Passive RFID – based Trilateration without Offline Training Stage", *IEEE RFID Technology and Applications Conference (RFID-TA)*, 2014.

[4] T. Kapłon, A. Milecki, "Localization of Passive RFID Tags by Small Cartesian Robot, in: Lecture Notes in Mechanical Engineering", *Advances in Manufacturing II*, vol. 1 – Solutions for Industry 4.0, Springer 2019.

[5] J. Marek; M. Illing, "Automotive sensors", *Proceedings, MEMS Components and Applications for Industry, Automobiles, Aerospace, and Communication II*; vol. 4981, 2003, https://doi.org/10.1117/12.480769.

[6] A. Juels, "RFID Security and Privacy: A Research Survey", *IEEE Journal on Selected Areas in Communications*, vol. 24 (2), 2006, pp. 381–394, DOI: 10.1109/JSAC.2005.861395

[7] Web site: http://www.onsemi.com, 1.06.2019.

[8] L. Fereira M., Marte C. L., E. Leal de Medeiros J., Cledson Akio Sakurai, C. F. Fontana, “RFID for Real Time Passenger Monitoring”, *Recent Re–searches in Telecommunications, Informatics, Electronics and Signal Processing*, ISBN: 978-960-474-330-8.
[9] Patent: Vehicle passenger detection apparatus with wireless acquisition of passenger-related data, US 20060283651 A1.
[10] Patent: Occupant detection and temperature forewarn safety system and method, US 7348880 B2.
[11] Patent: Manually operated switch for enabling and disabling an RFID card, US 6863220 B2.
[12] Patent: RFID buckle closure and presence sensor system for safety childseat, US 20070096891 A1.
[13] Patent: Wireless powerless switch sensor, US 7466041 B2.
[14] C. Tan, W. Chen, M. Rauterberg, “Development of adaptive aircraft passenger seat system for comfort improvement”, *in Proceeding of International Conference for Technical Postgraduates*, 2009.
[15] A. Ayyagari, C. F. Battles, B. J. Smith, S. A. Uczekaj, K. Y. Ung, “System for automated aircraft seat floatation device inspection”, in *Fourth International Conference on Networking and Services*, pp. 13–17. IEEE., 2008.
[16] M. Meckesheimer, B. Ramzy, G Bruce Loosli, “Dynamic seat labeling and passenger identification system”, *U.S. Patent No. 8,060,015.15,* 2011.
[17] K.V.S. Rao, P. V. Nikitin, S. F. Lam, “Antenna design for UHF RFID tags: a review and a practical application”, *IEEE Transactions on Antennas and Propagation*, vol. 53 (12), 2005.
[18] P. Jankowski-Mihułowicz, M. Węglarski, “A method for measuring the radiation pattern of UHF RFID transponders”, *Metrol. Meas. Syst.*, vol. 23 (2), pp. 163–172, 2016.

Radosław Rutkowski [1], Remigiusz Iwańkowicz [2]

ASSEMBLY MANAGEMENT IN THE SHIPYARD USING A WELDING DATABASE

Keywords: management, quality, shipbuilding, large-size steel structures, assembly sequence

Abstract

The paper discusses the problem of increasing the dimensional quality of the ship's hull at the stage of assembly sequence planning. The specifics of assembly of welded structures and problems related to thermal distortions are described. The welded joints were classified and the influence of welding works on the structure was systematised. A computational control system of the assembly sequence based on expert assessment of the important dimensions of the welded structure has been proposed. The presented method is open and allows for the extension with additional criteria for the optimisation of the assembly sequence. The article contains example calculations for the hull bottom section. Tests show the correctness of the algorithm and its sensitivity to control by weights of welding directions.

1. Introduction

One of the most geometrically complex and technologically difficult products are the hulls of modern sea and inland vessels. In order to ensure safe and economically viable transport of people and goods by waterways, the hull of the ship must meet a number of functional, hydrostatic, hydrodynamic, endurance, technological and ecological requirements.

The introduction of welded joints in ship hulls 100 years ago resulted in technological changes in shipyards around the world. Mastering the thermal joining of steel has led to the developments in the modular method of building hulls [1]. These modules are known as sections and blocks – the largest structures that a shipyard can move (figure 1).

In addition to changes in the processing of materials, ship production is also subject to widespread worldwide development towards industry 4.0 [2]. The authors [3] mention three main challenges facing the shipbuilding industry 4.0: increasing production efficiency, ensuring ship safety and balancing economic efficiency with ecological responsibility. Shipyard 4.0 is to be an enterprise that intelligently adapts to changes in the environment, efficiently manages resources, ergonomically ensuring close cooperation with the shipowner and suppliers. However, full development

---

[1] Maritime University of Szczecin, Faculty of Economics and Transport Engineering, ul. H. Pobożnego 11, 70-507 Szczecin, Poland, r.rutkowski@am.szczecin.pl

[2] Maritime University of Szczecin, Faculty of Economics and Transport Engineering, ul. H. Pobożnego 11, 70-507 Szczecin, Poland, r.iwankowicz@am.szczecin.pl

towards the automation of shipbuilding processes requires an even development of knowledge in key areas. In the first place, the dimensional quality of ship structures requires mastery. This is the basis for the ship production process –properly assembly and joining structures requires compliance of dimensions with the design. Given the size and complexity of the assembled structures, it is a highly complex and multifaceted task. Problems with dimensional quality already appear in the production of small vessels, and are critical for seagoing vessels.

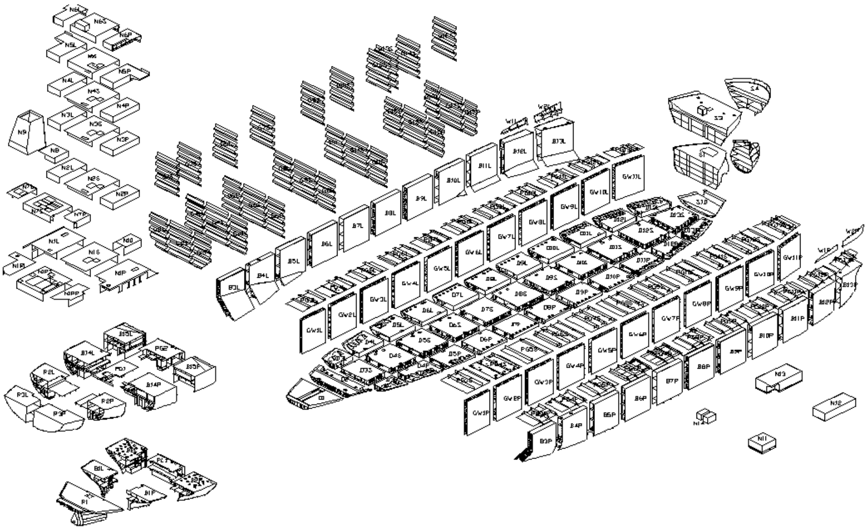

Fig. 1. An example of a subdivision of a commercial container ship

In the production process, virtually every technological operation affects the dimensional quality. Therefore, these operations should be carefully designed in a way that enables predicting distortions as much as possible, which will counteract their negative impact on the production process.

There are a number of measures for controlling the dimensional quality. The basic, generalised elements that make up the dimensional quality control processes are:

- issues of dimensioning, tolerance of dimensions and fitting of elements,
- control and measurement processes,
- issues related to welding distortions,
- structure assembly issues.

The experience of the authors shows that in shipyards of a medium technological advancement level, the overall increase in labour consumption resulting from the elimination of errors regarding the dimensional quality is at the level of 30÷40% of the total labour intensity of ship hull construction. Despite this, the problems of dimensional quality of large-size steel constructions are not widely discussed. Individual shipyards introduce own solutions to dimensional quality problems. It is purposeful to approach the problem comprehensively when developing quality control methods in the construction of large-size ship constructions. These methods should provide the foundation for individual dimensional quality control systems dedicated to specific shipyards.

2. Literature review

The important role of assembly planning automation for the shipbuilding industry is emphasised in numerous studies [4, 5, 6]. The demand for the methods of planning the assembly sequence of ship hulls was first noted already in 1979 [7], and many subsequent studies have approached assembly as one of the pivotal stages in the ship hull construction cycle [8, 9].

In the case of assembly of ship structures, in addition to the standard limitations of the geometry of the structure, the specificity of welding works should also be taken into account, and although it has been approached by several works [10, 11, 12], the proposed methods focus predominantly on the problems of modelling assembly and searching for solutions in extensive collections with the use of computational intelligence methods. The problems of minimising welding distortions during the optimisation of the assembly sequence of the hull have not yet been taken into account.

Forecasting welding strain and its impact on the hull structure is a relatively well-explored subject of scientific papers. Asian scholars [13, 14, 15, 16] for instance, propose a number of calculation and experimental methods for the determination of welding strains. The results of these works were used in determining the impact of individual welding works on the stiffness of the prefabricated structure.

Studies in the field of control and measurement [17, 18, 19, 20] describe the problem of welding distortions in assembly processes and analyse the susceptibility to distortions of various construction points of the hull.

The assembly sequence is included in the literature mainly in terms of its repeatability and statistical processing of data on welding distortions [21]. The analysis of structural susceptibility to deformation, the basic element of the presented method, is also analysed when designing measurement bases for assembly structures in the control and measurement processes. However, these analyses are carried out in a different scope – the assembly sequences are not investigated, but only the stiffness stages of individual elements and construction points with the given assembly procedure.

Literature analysis showed that the current knowledge enables the integration of ship hull assembly planning methods with the prediction of welding distortions. For this purpose, it is necessary to develop a mathematical model and its implementation in a programming environment, which has been assumed as the goal of this article.

3. Methodology

The hull section is a large-size welded construction that is a basic assembly unit in the hull construction process. The assembly process of the section is disturbed by the basic feature of steel materials, i.e. thermal expansion. This effect is very difficult to approach theoretically due to the sheer number of co-existing construction elements: a single section can incorporate hundreds of elements. One of the basic problems in this case is the computational complexity. The developed method is characterised by the speed of action allowing for application in real production in the execution of the primary objective: reducing the welding distortions of the structure.

On the basis of literature research and observation of shipyard processes, it was found that:

- when welding the fillet joint, the strongest thermal shrinkage occurs in the plane of sheathing perpendicular to the weld, while the structure is reinforced in the direction parallel to the sheathing,
- while welding the butt joint, the main thermal contraction occurs in the plane of the sheets perpendicular to the weld, while the construction reinforcement is negligible.

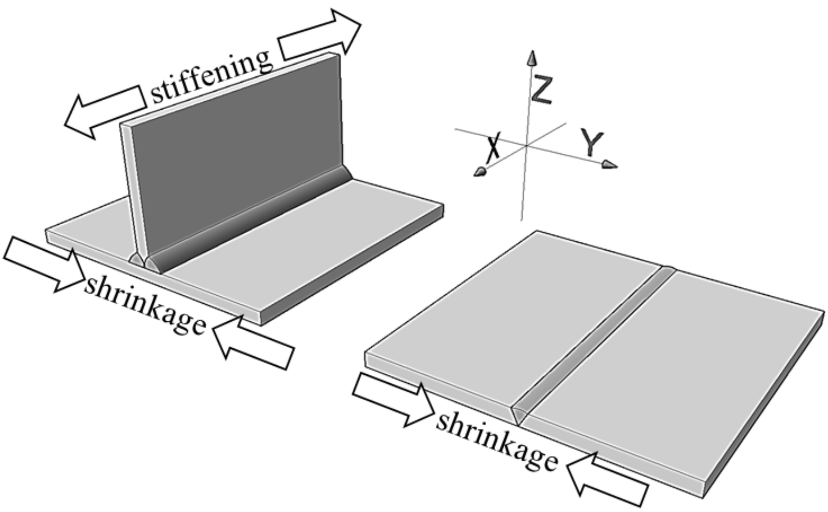

Fig. 2. The influence of basic types of joints on thermal distortion: the fillet joint causes shrinkage in the Y-direction and stiffens the structure in the X-direction, the butt joint causes shrinkage in the Y-direction

The proposed method of sequencing is based on the principle that the construction should be implemented at the beginning of the assembly, while the welded joints that deform the structure to the largest extent should be made possible at the latest.

4. Theoretical model

The proposed algorithm (figure 3) is based on the welded joints classification system which categorises any set of joints into separable subsets according to established criteria. These can be classes related to the geometry of the welded joint and the type of connected elements of the structure. In the case of hull sections, the basic division is the distinction between the fillet and butt joints.

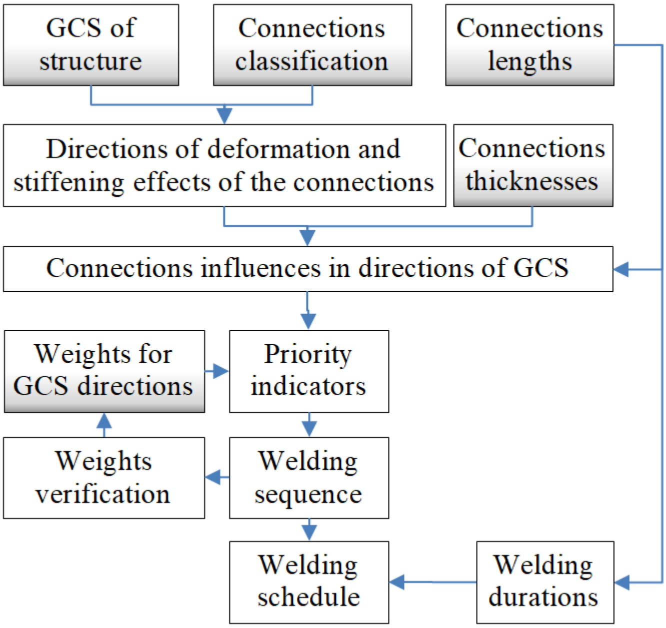

Fig. 3. Algorithm of conduct during sequencing and assembly scheduling

By joining welding sequencing and scheduling, the following construction information is obtained:

- classification of welded joints,
- lengths $l_1, l_2, \ldots, l_n$ and thicknesses $a_1, a_2, \ldots, a_n$ of joints,
- directions (X, Y or Z) of the deformation and stiffening effects of the welded joints.

Prior to calculations, the following weight factors must be specified:

$$w_X, w_Y, w_Z \in [0,1], w_X + w_Y + w_Z = 1 \tag{1}$$

where: w_X, w_Y, w_Z – weights for X, Y and Z directions respectively.

The higher the weight, the stronger the algorithm "avoids" deformations in a given direction.

The directions of shrinkage and stiffening of the structure are determined for each joint in accordance with the principle shown in figure 2. In the digital record, the numbers 1, 2, 3, respectively, are assigned to directions.

If the interaction of the welded joint i = (1, 2, ..., n) is of the stiffening nature in the direction j = (1, 2, 3), then the force of this interaction is determined by the indicator:

$$influence_{i,j} = l_i \cdot a_i \tag{2}$$

where: l_i – length and a_i – thickness of joint i.

If the joint causes shrinkage, the indicator takes on a negative sign:

$$influence_{i,j} = (-1) \cdot l_i \cdot a_i \tag{3}$$

where: l_i – length and a_i – thickness of joint i.

A priority indicator shall be determined for each joint:

$$priority_i = \sum_{j=1,2,3} w_j \cdot influence_{i,j} \tag{4}$$

The lower the priority indicator, the stronger the negative impact of the welded joint on the geometry of the structure, taking into account the assumed weighting of the directions.

The welding sequence is represented by the binary square matrix S=$(s_{i,j})_{n\times n}$. Its elements are determined by comparing priority indicators. Joint i must be made before joint j, when the condition is met:

$$priority_i > priority_j \Leftrightarrow s_{i,j} = 1 \tag{5}$$

where: $s_{i,j}$X{0,1} – determine if joint i is welded before joint j in the assembly sequence.

On the basis of the assembly sequence and welding times, it is possible to carry out a critical path analysis and set boundary deadlines for starting operations. The space of acceptable schedules created in this way can be very large. The problem of searching for an optimal schedule in it is not the subject of this article. However, it should be noted that the optimisation of the schedule at a fixed sequence is a multi-criteria problem and an effective tool in its implementation are the evolutionary algorithms [22].

5. Example study

The example analysis includes the section of the double bottom consisting of outer and inner plating, stiffeners, longitudinal and transverse girders (figure 4).

Figure 5 presents the section broken down into elements. The black fields show the numbering of elements, the white ones – the numbering of welded joints between elements. The numbering of elements has been simplified by grouping the identical ones, assembled in one technological process. For example, stiffeners combined with the sheet metal plating number 7 are grouped under one number 23. Some elements are previously prefabricated assemblies, for example, girders no. 15 and 16.

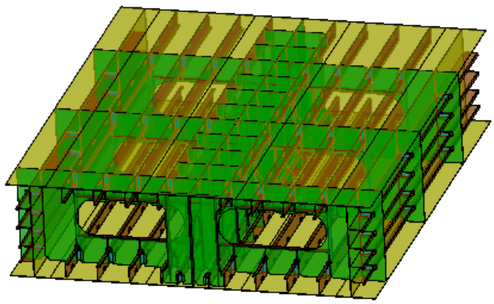

Fig. 4. Test section

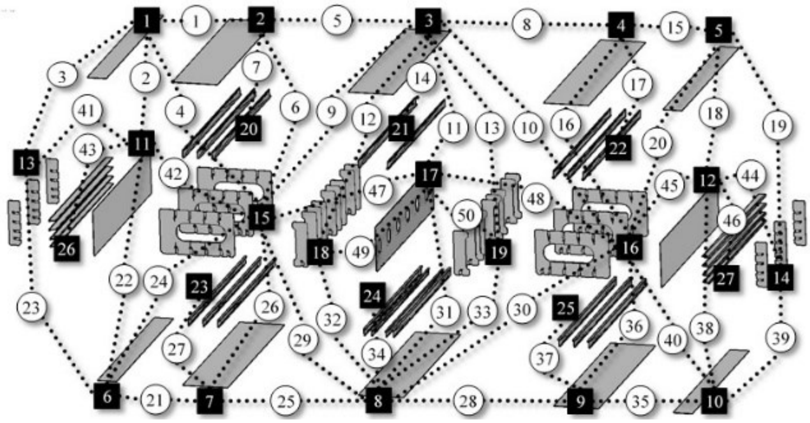

Fig. 5. The numbering of construction elements and welded joints

One of the main assumptions of the present method is the influence of individual directions of welded joints on the stiffness and deformability of the prefabricated structures. In order to illustrate the welding directions for the test section, a visualisation of the connection diagram shown in figure 6 was performed. It should be noted that the welded joints between the grouped elements are also represented symbolically as a single connection. The schematic representation of welded joints determines the orientation in the coordinate system and facilitates the definition of the effect of shrinkage and stiffening for each joint.

The diagram of joints is also a convenient presentation tool for tracking the progress of assembly of the structure according to a fixed sequence.

According to the algorithm shown in figure 3, it is necessary to determine the weights of the welding directions before starting the calculations. The Y-direction along stiffeners (w_2=1) was taken as the priority. The vertical joints

Z were considered to be secondary (w_3=0.8), while the X direction was considered the least significant for the geometry of the section (w_1=0.2). The weight factors selected in this way are in accordance with shipbuilding practice, where the stiffeners are welded to the plating before girders. The conducted analysis allowed to determine the sequence of assembly, the subsequent steps of which are illustrated in figure 7 – 10.

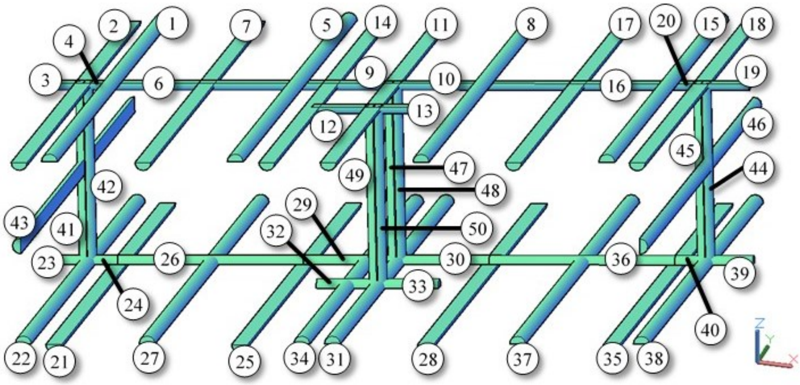

Fig. 6. Schematic representation of welded joints in the structure

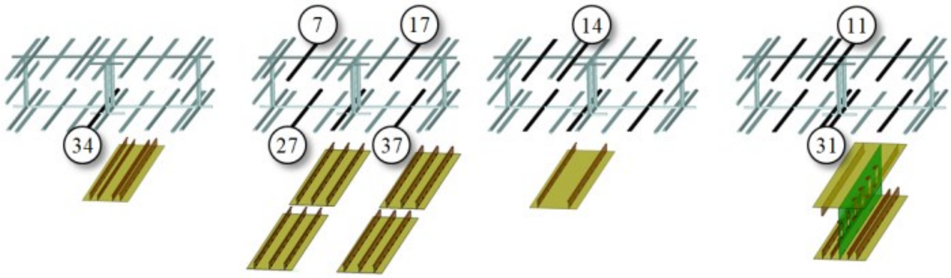

Fig. 7. Beginning of assembly – successive states of the structure – from left to right

The initial assembly stages include the prefabrication of stiffened pieces and the assembly of the central girder.

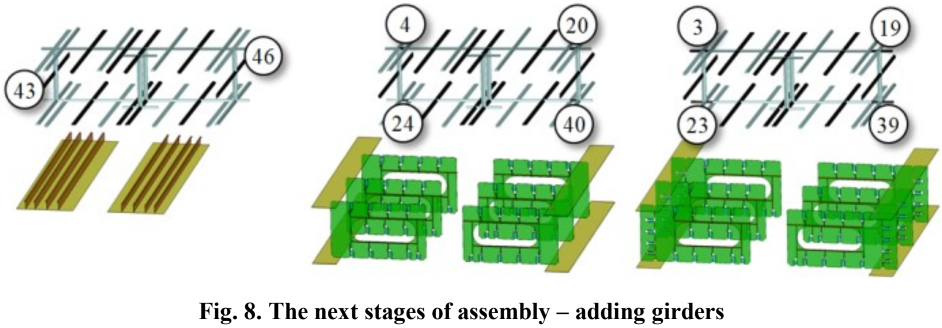

Fig. 8. The next stages of assembly – adding girders

Then, further stiffened pieces are prefabricated and rider plates are connected with narrow external and internal plating sheets. This is not a typical solution in shipbuilding practice due to the flaccidity of prefabricated elements. The next joints proposed by the algorithm add vertical girders. As a result, the assembly of girders in subsequent stages will be technologically difficult.

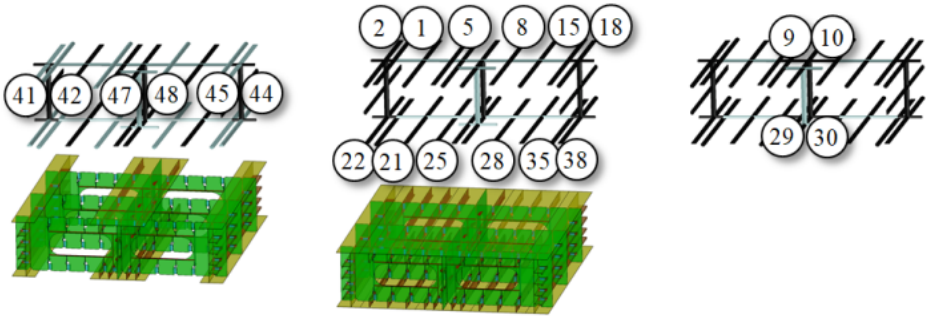

Fig. 9. The following stages of assembly – closing the structure and reinforcing welding

The plates are connected to the central and side longitudinal girders. Then, prefabricated plates are added. In the next stage, the missing joints are completed – as a result, the structure is strengthened.

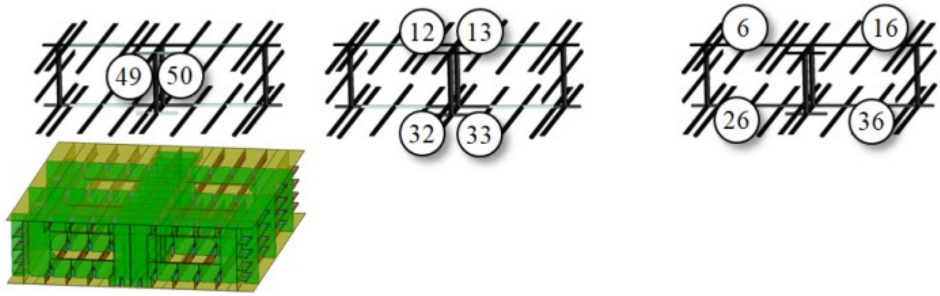

Fig. 10. Adding the last stiffeners and finishing the welding assembly

The vertical stiffeners of the central longitudinal girder are added in the end. The assembly process completes the welding of the remaining joints between the already installed elements.

6. Summary

The method of designing the assembly sequence proposed in the article, taking into account welding distortions, was developed as a result of many years of observation of ship design and production processes.

In shipyards with highly advanced technological facilities, the dimensional quality control is based mainly on advanced welding methods as well as repeatability and automation of works. This allows controlling the dimensional quality based on the results of control, measurements and statistical methods. Advanced control and measurement systems provide data for the design of technological surpluses minimising the negative impact of welding distortions. In shipyards with a medium and low level of technological facilities, the production process is so variable that the only method of limiting the impact of deformations is through assembly supplies and permanent dimensional control. After completing the welding, the stocks are removed and the remaining dimensional errors are repaired by thermal straightening. Such a procedure causes additional labour-intensive production and introduces additional stresses to the construction.

In highly-automated shipyards, assembly planning is a priority and includes the technological back-up facilities (automatic machines, welding robots). In less technologically advanced shipyards, the order of the assembly often results from common practices and experience.

The method of planning assembly presented in this article is based on the estimation of the negative and positive impact of joint welding on the geometry of the structure.

The test analyses showed the correctness of the calculation algorithm and the sensitivity of the obtained results to control by means of direction weights. Calculations conducted for weights $w1$=0.2; $w2$=1; $w3$=0.8 resulted in a non-typical sequence from the point of view of shipbuilding practice. Particularly the assembly of the side girders may be difficult, although not impossible. However, lowering the assembly flexibility is the expected phenomenon because the planning was focused on minimising structural deformation. Factors such as flaccidity of prefabricates, welding positions and availability of structures for welding machines were not taken into account.

The presented model is characterised by its development potential, e.g. expanding it with new welded joints classes and introducing additional rules for establishing priority relations between connections.

The developed calculation algorithm will be subsequently verified by the finite element method, upon which it is planned for laboratory tests on the actual structure.

In addition to the primary purpose – to systematise the order of assembly work from the point of view of welding distortion, the proposed method determines the degree of deformation resistance of particular points of the structure. Such data will be invaluable in the process of designing measurement bases, constituting the main element of the expanding matrix, necessary for the correct assembly of large-sized constructions.

Determination of the degree of stiffness of individual points of the matrix at individual stages of production is one of the biggest problems in the design of control and measurement systems. The solutions proposed in the article open a number of possibilities to improve the dimensional quality in the construction of ship structures.

References

[1] B. Metschkow, T. Urbański, "Prediction of a transverse shinkage of butt welded joints", *In 12th International Congress of the International Maritime Association of the Mediterranean – IMAM. Varna, Bułgaria, Taylor&Francis/Balkema*, pp. 483–487, 2007.

[2] Á. R. Rivas, "Navantia's Shipyard 4.0 model overview", *Ship Science & Technology*, vol. 11(22), pp. 77-85, 2018, https://doi.org/10.25043/19098642.165.

[3] V. Stanić, M. Hadjina, N. Fafandjel, T. Matulja, "Toward Shipbuiding 4.0 - an Industry 4.0 Changing the Face of the Shipbuiding Industry", *Brodogradnja*, vol. 69(3), 2018, https://doi.org/10.21278/brod69307.

[4] M.–G. Back, D.–K. Lee, J.–G. Shin, J.–H. Woo, "A study for production simulation model generation system based on data model at a shipyard", *International Journal of Naval Architecture and Ocean Engineering*, vol. 8(5), pp. 496–510, 2016.

[5] D. H. Yun, S. I. Choi, S. H. Kim, K. H. Ko, "Registration of multiview point clouds for application to ship fabrication", *Graphical Models*, vol.90, pp. 1–12, 2017.

[6] W. Zhao-Hui, D. Ji-Wang, Z. Ming-hua, F. Xiu-min, "Survey on Flexible Shipbuilding Technologies for Curved Ship-Blocks", *Procedia Engineering*, vol. 174, pp.800–807, 2017.

[7] S. K. Banerjee, "Shipyard production systems design: a statistical approach", *International Journal of Production Research*, vol. 6, pp. 541–555, 1979.

[8] Y. Chi, S. Jun, "Intelligentized work-preparation for ship hull construction with Optimized Assembly Planning System", *In Proceedings of the IEEE International Conference on Systems, Man and Cybernetics*, Istanbul, Turkey, vol. 10–13, pp. 2740–2744, 2010.

[9] S. Ghandi, E. Masehian, "Assembly sequence planning of rigid and flexible parts", *Journal of Manufacturing Systems*, vol. 36, pp. 128–146, 2015.

[10] K.-K. Cho, J.-G. Sun, J.-S. Oh, "An automated welding operation planning system for block assembly in shipbuilding", *International Journal of Production Economics*, vol. 60-61, pp. 203-209, 1999, https://doi.org/10.1016/S0925-5273(98)00151-0.

[11] R. Iwańkowicz, "An efficient evolutionary method of assembly sequence planning for shipbuilding industry", *Assembly Automation*, vol. 36(1), pp. 60–71, 2016.

[12] R. Iwańkowicz, M. Taraska, "Self-classification of assembly database using evolutionary method", *Assembly Automation*, vol. 38(1), 2017.

[13] H. Heeyoung, C. Hyun, P. Junggoo, W. Seokhee, "Compensation of welding shrinkage in ship production by integrating computer-aided design and computer-aided engineering in a design for assembly technique", *J Engineering for the Maritime Environment*, vol. 229(2), pp. 174–186, 2015, https://doi.org/10.1177/1475090213509610.

[14] H. Yun-Sok, "Development of thermal distortion analysis method on large shell structure using inherent strain as boundary condition", *Journal of the Society of Naval Architects of Korea*, vol. 45(1), pp. 93–100, 2008, https://doi.org/10.3744/SNAK.2008.45.1.93.

[15] H. Yun-Sok, S. Cho, T. Jang, "Development of Welding Distortion Analysis Method Using Residual Strain as Boundary Condition", *Materials Science Forum*, vol. 580–582, pp. 649–654, 2008, https://doi.org/10.4028/www.scientific.net/MSF.580-582.649.
[16] H. Murakawa, N. Ma, "Research on welding simulation methods and software development", *China Welding (English Edition),* vol. 23(1), pp. 19–26, 2014.
[17] R. Rutkowski, "Dynamical control of dimensional quality of large steel structures in production enterprises of low - level technological support", *Polish Maritime Research 1(64)*, vol. 17(1), pp. 80-88, 2010, https://doi.org/10.2478/v10012–010-0010-7.
[18] R. Varghese, D. Young Yoon, "Dynamic spatial block arrangement scheduling in shipbuilding industry using genetic algorithm", *In INDIN '05 2005 3rd IEEE International Conference on Industrial Informatics. Perth, WA, Australia*, pp. 444–449, 2005, https://doi.org/10.1109/INDIN.2005.1560417.
[19] Y. Okumoto, "Dimensional Error of Assembled Blocks", *Journal of Ship Production*, vol. 17(1), 2001.
[20] Y. Okumoto, "Optimization of Block Erection Using a Genetic Algorithm", *Journal of Ship Production*, vol. 18(2), 2002.
[21] H. Heeyoung, Ch. Hyun, "Stochastic assessment considering process variation for impact of welding shrinkage on cost of ship production", *International Journal of Production Research*, vol. 52(20), 2014, https://doi.org/10.1080/00207543.2014.911986.
[22] R. Iwańkowicz, "Metody sekwencjonowania i harmonogramowania montażu kadłubów statków morskich", *Wydawnictwo Uczelniane Zachodniopomorskiego Uniwersytetu Technologicznego w Szczecinie*, 2016.

Martyna Wawrzyk[1], *Małgorzata Plechawska-Wójcik*[2]

IT APPLICATIONS IN ATHLETE'S MENTAL TRAINING WITH THE EEG BIOFEEDBACK METHOD

Keywords: biofeedback EEG, sport, concentration training

Abstract

The purpose of this study was to apply the biofeedback EEG method as a tool to support concentration training among athletes. The training consisted of displaying stimulation information about changes in the power of the beta wave in real time during participation in game-target shooting. The value of beta power was received from electrode Cz by using Smart BCI amplifier. The study was divided into 2 sessions. Each session was subdivided into 2 stages (first stage – calibration the value of beta power, second stage – training concentration repeated three times). One woman and two men participated in the study. FFT spectral analysis and statistical analysis were performed on the data obtained. Statistically significant differences were observed between the first and second session for all participants. Also were observed an increase in the value of the beta power from C4 electrode and at the same time a decrease in the value of the beta power from C3 electrode. The one-way ANOVA analysis in some cases showed statistically significant differences between trails during one session.

1. Introduction

Nowadays the cooperation of a sport and exercise psychologist with athletes before competitions is essential. Support from a psychologist before major competitions is known to have positive effects on the final results of athletes. J. Blecharz and D. Nowicki propose a model consisting of three attributes: concentration, composure and self-confidence [1]. These attributes should be possessed by each athlete, and yet the central issue is that athletes should get proper concentration, composure and confidence just when they most need it. This is a complicated process, therefore athletes need support from a psychologist.

One of the methods used by sport and exercise psychologists is the biofeedback method, consisting of three stages: measurement of physiological parameters (data acquisition), data processing and display of simulations in real time, i.e. the changes of physiological parameters. Biofeedback helps to understand the psychology and motility of an athlete's own body. The main goal of the

[1] Lublin University of Technology, Faculty of Electrical Engineering and Computer Science, Institute of Computer Science, Nadbystrzycka 38 D Str., Poland, martyna.wawrzyk@pollub.edu.pl

[2] Lublin University of Technology, Faculty of Electrical Engineering and Computer Science, Institute of Computer Science, Nadbystrzycka 38 D Str., Poland, m.plechawska@pollub.pl

biofeedback system is the development of self-regulation [2], [3]. Monitoring parameter changes allows determining the emotional state of the person examined, who at the same time can observe the stimulus. This, in turn, may affect the behaviour of patients, which is the way a biofeedback loop is created. Depending on what kind of physiological parameter is measured, such as electroencephalography (EEG), electrocardiography (ECG), electromyography (EMG) and others, there are many kinds of commercially available biofeedback devices.

2. Electroencephalography

Electroencephalography is a non-invasive diagnostic method used for examination of brain activity. The potentials generated by millions of nerve cells are registered with the use of an electroencephalograph. The device consists of an amplifier, electrodes placed at the surface of the head and a cap, which is used to keep the electrodes in place. The 10-20 system recommended by the International Federation of Clinical Neurophysiology determines the distribution and nomenclature of the electrodes.

Tab. 2.1 Description of brain waves [5], [6]

Name	Frequency	Description
Gamma	Above 30 Hz	Gamma oscillations are associated with **cognitive activity,** e.g. intensely **focused attention**. Gamma oscillations are also observed during **working memory** maintenance and assist the brain in processing and binding information from different areas of the brain.
Beta	15–30 Hz	Mid Beta (16-20 Hz) is related to **active problem solving**, **intellectual activity**, outward **focus**, and **attention**. More Beta is required when **learning a task** than once it has been mastered. High Beta (19-22 Hz) can also be observed during negative ruminating in some individuals.
SMR*	12–15 Hz	SMR is associated with **relaxed attentiveness**, **decreased anxiety and impulsivity**. It may also correlate with a decrease in involuntary **motor activity.**
Alpha	8–12 Hz	Alpha, by adolescence, is the dominant rhythm in EEG and is generally associated with a **state of relaxation** and **self-awareness.**
Theta	4–8 Hz	Theta can be associated with **internal orientation,** intuition, drowsy states or **memory function**.
Delta	0.5–4 Hz	Delta is dominant **during deep sleep** and is associated with **memory consolidation**, while in wakefulness it is associated with learning disabilities, cognitive impairment, and brain injury.

*SMR- Sensorimotor Rhythm

The EEG signal presents five types of brain waves with unwanted registered noise known as artifacts. The artifacts are divided into two groups: biological artifacts and technical artifacts [4]. Biological artifacts are generated by every body movement, blinking eyes, muscle tension (in particular jaw tension). The noise from the power grid and problems associated with devices are the source of technical artifacts. Special algorithms and filters are used in order to eliminate the artifacts before processing the data.

There are two methods used for EEG data analysis. The first is the analysis in the time domain, although in practice the spectral analysis is used, which means analysis in the frequency domain. One of the algorithms used in the spectral analysis is the Fourier Transform, described by formula 2.1. However, calculating the transform directly from the formula is rather ineffective due to the high computational complexity. In order to speed up the process, a Fast Fourier Transform (FFT) is used, which gives a discrete Fourier transform (DFT).

$$X(\boldsymbol{f}) = \int_{-\infty}^{\infty} \boldsymbol{x}(\boldsymbol{t}) \boldsymbol{e}^{-\boldsymbol{j2\pi ft}} \, \boldsymbol{dt} \qquad (2.1), [7]$$

3. EEG biofeedback. Related work.

The period of athletes' preparation for specific competitions is a complicated process including numerous elements. Trainers know that good physical preparation is not enough to achieve the goal. In the athlete's training, the mental side is as important as the physical work. Trainers employ different methods to properly prepare the athlete for the most important competitions. One of them is the EEG biofeedback system, also known as neurofeedback (NFB). Psychologists use this method with an increasing frequency in the treatment of nervous system disorders and cooperation with athletes. By using this system, athletes can teach self-regulation skills and enhance their performance during competition. The mechanism of the biofeedback system is explained in figure 3. In the case of neurofeedback, brain activity is measured by selected electrodes. Subsequently, data are processed by filters and algorithms. Filtered data present a wave with a specific frequency. Consequently, it is possible to select a wave for visual or auditory simulations, e.g. alpha in simulations for reducing stress and anxiety. It is worth pointing out that selected electrodes must be from the area of the head associated with the chosen activity of the brain. In examinations, one or two electrodes are typically used [5].

Interest in the biofeedback method in sports has increased since 2006. That year the football World Cup was held, in which Italy defeated France. The press reported that several Italian players who played for AC Milan used biofeedback to help them with their mental preparation. It was reported that the team psychologist used biofeedback technology to create what he called the "Mind Room". In that room the football players were shown short video clips of successful and unsuccessful performances while receiving feedback about brainwaves and cardiovascular activity [8], [9].

The neurofeedback training stimulated the increase of the amplitude of SMR and beta1 (13–20 Hz) and the decrease of the amplitude of theta and beta2 (20–30 Hz) to improve cognitive performance [10]. The regulation of slow potentials from T3 and T4 electrodes can improve concentration and enhance self-confidence among archers [11]. Stimulation based on the alpha-theta coefficient (focus factor) from the Pz electrode can improve the performance of dance performances [12], [13], [14]. There is also the possibility of combining two types of biofeedback, such as HR and EEG biofeedback in one training session. The stimulation of the value of heart rhythm and alpha amplitude (from C3 and C4 electrodes) can influence the behaviour of patients in different stress situations [15]. However, the use of HR biofeedback with SMR and theta wave stimulation was shown to improve the balance in gymnastics [16]. The reduction of theta amplitude and stimulation of the alpha/theta ratio from the Fz electrode can support a golf player's skills [17], [18], and also stimulation of SMR amplitude from Cz electrode [19].

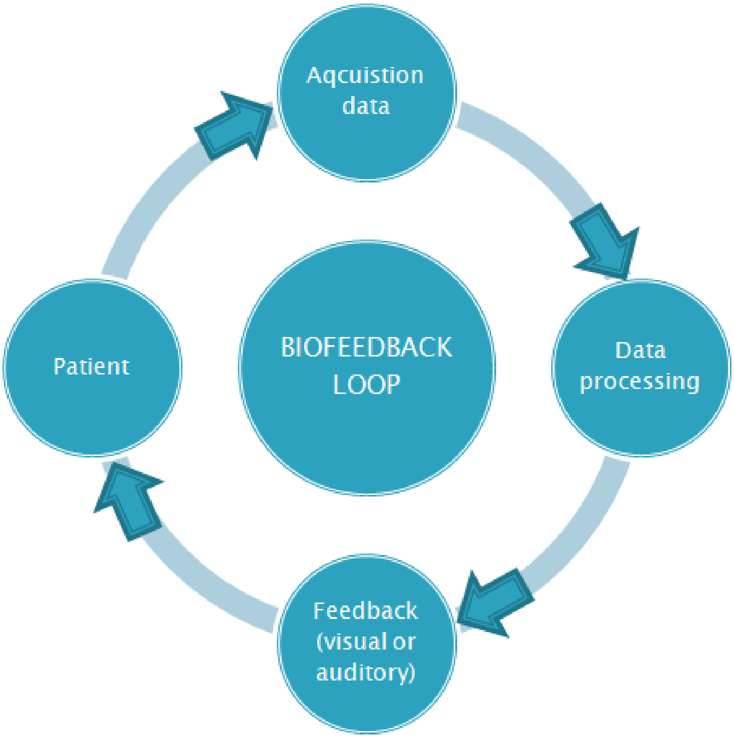

Fig. 1. Mechanism of the biofeedback system

4. The case study

4.1. The purpose of research

The aim of the research is to verify the training of NFB concentration among athletes on the basis of spectral analysis of collected data. The NFB training was based on stimulation of power beta in the range 16–24 Hz from the Cz electrode.

4.2. Research procedure

One woman and two men aged 23 took part in this study. All participants train athletics and swimming in the same sports club. The study was divided into two sessions with an interval of one week. During one session the calibration of the value of beta power was applied, then concentration training was repeated three times. The calibration and stimulation of beta power were performed in OpenVibe, free open-source software. The EEG signal was recorded with a 24–channel Smart BCI mobile amplifier.

4.3. Calibration

The value of the beta wave power was calibrated during the relaxation session. The participants were asked to look at the image displayed on the monitor for 30 seconds. The data for calibration was received by 5 electrodes: Fz, C3, Cz, C4 and Pz. The Laplacian filter was used to convert five channels into one channel (*LF_channel*). The signal was filtered in the 16–24 Hz range. Then, 1 s epochs were selected every 0.1 s and the power of beta was calculated and averaged. Finally, the mean and variance of the beta wave power were calculated. These values are used to estimate the range of power beta for an NFB session.

4.4. NFB session

Neurofeedback concentration training included the game-target shooting with simulations, which displayed the changes of power beta value in real time. The simulations changed the colour depending on the value of power beta. The participants played a game about 2–3 minutes with a 5-minute break. figure 2. point b) presents the neurofeedback scenario in OpenVibe software. The box *'Crop'* included the mean and variance of power beta values, which were calculated in the calibration process. Formula 4.1 and 4.2 were applied for assessment of the range of power beta value.

$$Min\_crop\_value = \bar{x} - 3\sqrt{\delta^2} \quad (4.1)$$

$$Max\_crop\_value = \bar{x} + 3\sqrt{\delta^2} \quad (4.2)$$

$\bar{x}$ – mean
δ^2 – variance

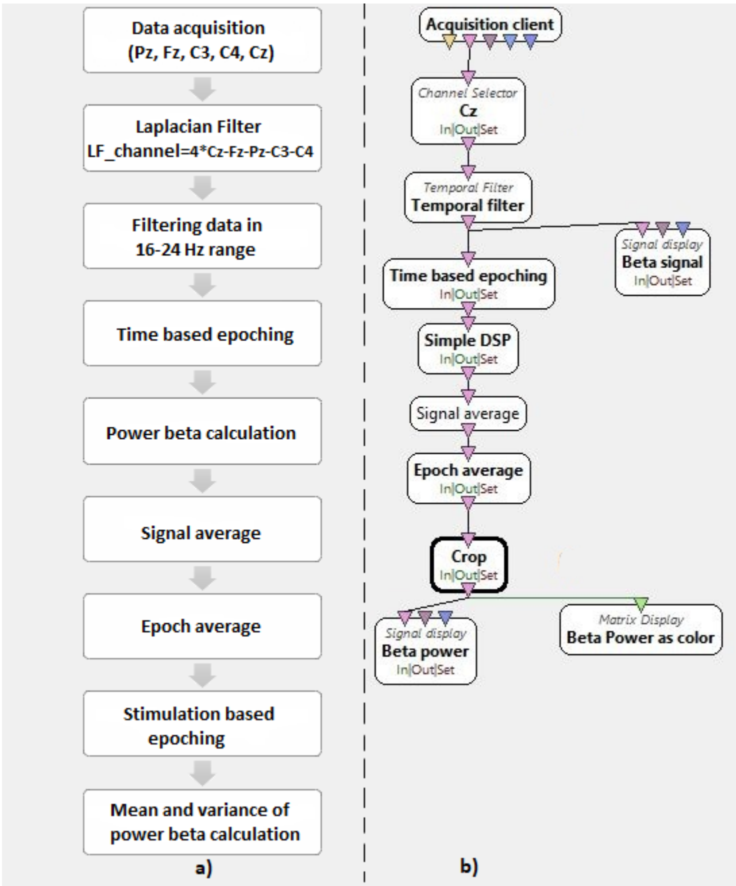

Fig. 2. a) Calibration process, b) Neurofeedback scenario

5. Data processing

The spectral analysis was performed for the obtained data. The FFT was conducted with the use of OpenVibe software. The data were divided into 1 s epochs with 0.00625 s intervals. The 70 s fragments in the frequency domain with about 12,000 samples were selected for statistical analysis. The Student's t-test and the one-way Anova analysis were applied in Statistica software.

5.1. Student's t-test

In order to compare the mean values from the two sessions, the student's t-test was used. The values from each NFB session were averaged (for Fz, Pz, C3, C4, Cz electrodes and for data from the Laplacian filter). As a result, the average values from the first and the second sessions were obtained. The Student's t-test was to verify whether the differences between the mean values of the two sessions were statistically significant, and therefore whether the student's t-test result would be significant at $p<0.05$. Separately for each participant, the box plots were compared on the same scale for the electrodes Fz, C3, Cz, C4 and Pz.

5.2. The one-way Anova analysis

The one-way Anova analysis of variance was used to compare the variance of power beta values from NFB training in a single session. Employing this method enabled a comparative analysis of the results from each sample and from each electrode and for the SF channel. As in the case of the Student's t-test, the purpose of the ANOVA analysis is to determine whether the differences between samples are statistically significant ($p<0.05$).

6. Results

6.1. Calibration results

Table 2 presents the calibration results of all the persons examined. In each session, the calibration was repeated at least three times in order to correctly verify the mean value and variance of power beta. Large differences in the power of beta between participants were noted, therefore, the final results of the statistical analysis were considered individually. In participant 2 during the calibration, much higher mean and variance values were observed compared to the values observed during the "neurofeedback" scenario. For this reason, the min_crop and max_crop values were set to reflect on the observations (empirical).

Tab. 2. The results of calibration

Participant	Session	Mean [μV^2]	Variance [μV^2]	Min_crop [μV^2]	Max_crop [μV^2]
1	I	10.55	4.61	4.10	17.00
	II	10.30	9.16	1.22	19.38
2	I	38.57	19.98	**6.50**	**22.00**
	II	35.54	22.98	**6.50**	**22.00**
3	I	2.83	0.64	0.45	5.25
	II	3.92	1.69	0.50	7.82

6.2. Student's t-test results

In the case of participant 1 and participant 3, the decrease in values of power beta in the second session was observed. Participant 2 presents higher values in the second session compared to the first one. Each person examined presents much lower power beta values from C3 in comparison with electrode C4. It must be noted that electrode C3 is placed at the left hemisphere of the brain, C4 at the right hemisphere. Only participant 1 presents statistically significant differences between the first and the second session in all cases.

Tab.3. ***p-value*** **calculated by T-student test**

Participant	Fz	C3	Cz	C4	Pz	LF_channel
1	**<0.05**	**<0.05**	**<0.05**	**<0.05**	**<0.05**	**<0.05**
2	>0.05	**<0.05**	>0.05	>0.05	**<0.05**	**<0.05**
3	>0.05	>0.05	**<0.05**	**<0.05**	>0.05	**<0.05**

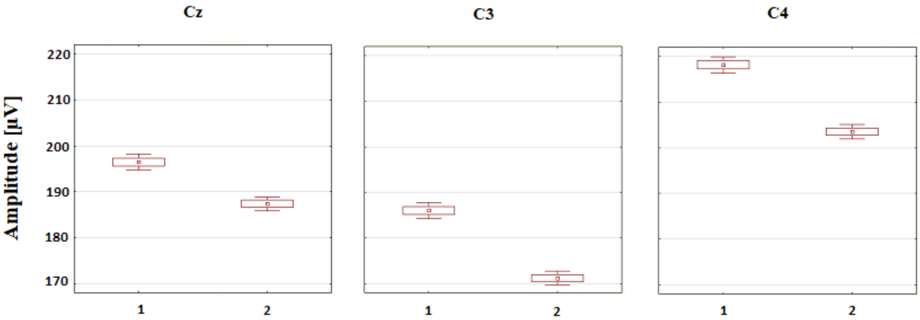

Fig. 3 Box plot Participant 1

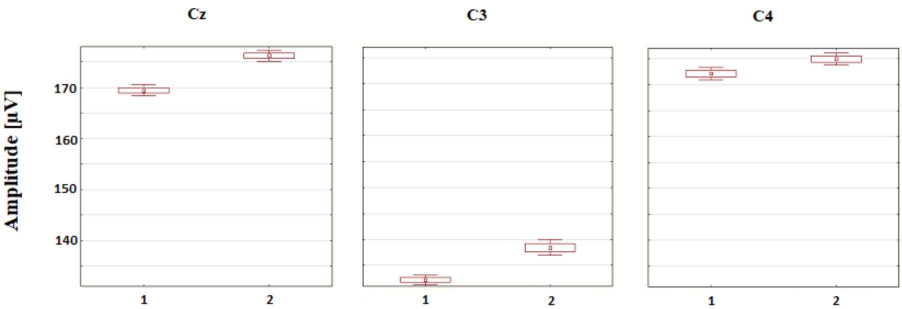

Fig. 4 Box plot Participant 2

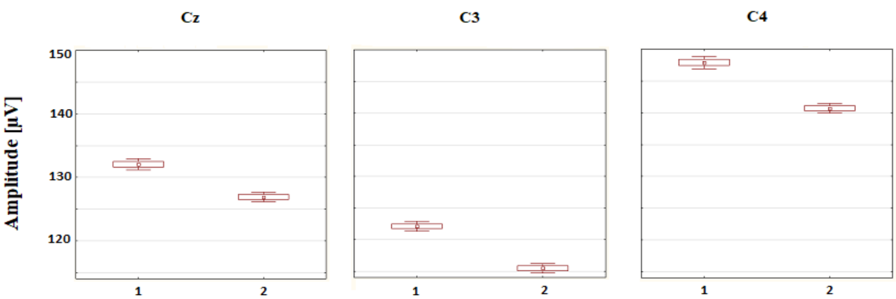

Fig. 5 Box plot Participant 3

6.3. The one-way Anova analysis results

The results of the Anova analysis present statistically significant differences in almost all cases. Exceptions occurred in the cases of electrode Fz and the *LF_channel* in the first session for participant 1, in the case of the *LF_channel* in the first and second session for participant 2. Figures 6 and 7 present the changes in the beta power value between NFB training sessions.

Participant 2 presents the same trend in two sessions. The third attempt in two sessions shows the highest values of the amplitudes of beta. Participant 1 and participant 3 do not show the same trend in two sessions.

Tab. 4 *p-value* calculated by Anova analysis

Participant	Session	Fz	C3	Cz	C4	Pz	LF_channel
1	I	>0.05	**<0.05**	**<0.05**	**<0.05**	**<0.05**	>0.05
	II	**<0.05**	**<0.05**	**<0.05**	**<0.05**	**<0.05**	**<0.05**
2	I	**<0.05**	**<0.05**	**<0.05**	**<0.05**	**<0.05**	>0.05
	II	**<0.05**	**<0.05**	**<0.05**	**<0.05**	**<0.05**	>0.05
3	I	**<0.05**	**<0.05**	**<0.05**	**<0.05**	**<0.05**	**<0.05**
	II	**<0.05**	**<0.05**	**<0.05**	**<0.05**	**<0.05**	**<0.05**

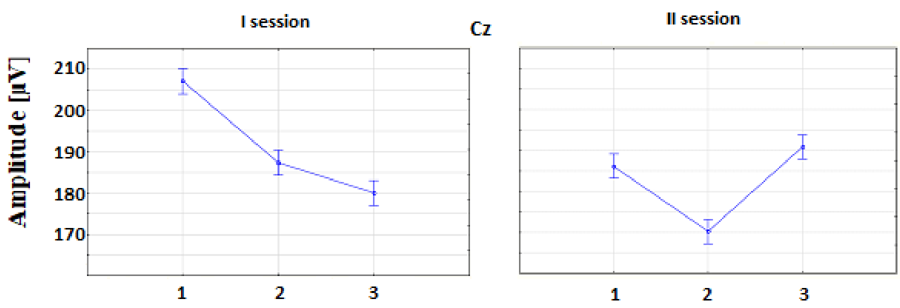

Fig. 6 Participant 1

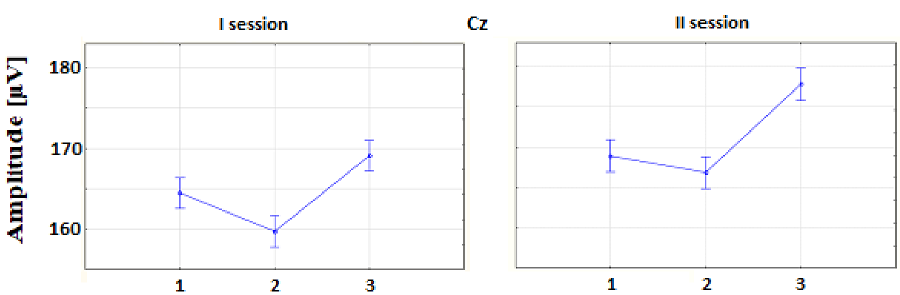

Fig. 7 Participant 2

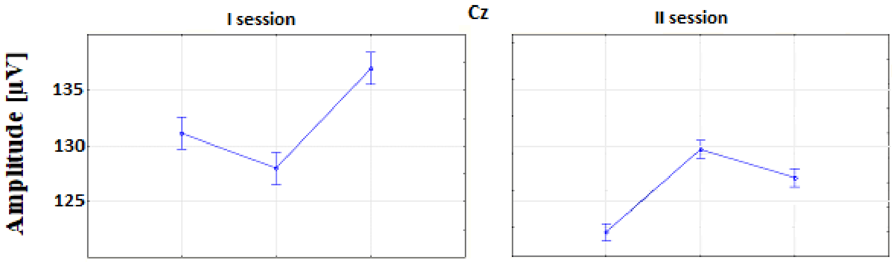

Fig. 8 Participant 3

7. Conclusion and discussion

The research results show that the use of the EEG biofeedback method influences the change of the beta wave value during the concentration training. In the case of all participants, the differences were statistically significant both between the NFB training and between the sessions. Changes that occurred between the trials and sessions did not occur in the same way among all examined persons. One of the common features found in all participants is the occurrence of large differences between the C3 and C4 electrodes. This indicates that the activity of the beta wave may have a different character due to the hemisphere of the brain. Also in all participants, the results of the student's t-test showed that the differences between sessions for the *LF_channel* are statistically significant.

However, it should be pointed out that this study was preliminary and further examination will be conducted with more participants to confirm the above results. In addition, the study can be carried out together with the participation of the control group to compare the results with the research group. In addition, the recorded resting signal before and after the session could illustrate the changes that took place after the end of the training session. What is more, recording the results obtained during the game could inform about the progress during the session and check whether this type of training, along with the display of the beta power value, improves the targeting ability.

In further research, the calibration procedure should be modified. During the calibration in the case of participant 2, the values were much higher compared to the values from the same Cz electrode. Therefore, it is necessary to calibrate by means of an amplifier with more channels or to calibrate the power beta only from the Cz electrode.

References

[1]. J. Blecharz i D. Nowicki, „Psychologiczne aspekty adaptacji sportowców do zmiennych warunków klimatycznych”, *Sport Wyczyn.*, no 7–8, pp. 427–428, 2000.

[2]. J. Blecharz, „Psychologia we współczesnym sporcie – punkt wyjścia i możliwości rozwoju”, *Przegląd Psychol.*, vol. 49(4), pp. 445–462, 2006.

[3]. S. J. Petruzzello, D. M. Landers, i W. Salazar, „Biofeedback and sport/exercise performance: Applications and limitations”, *Behav. Ther.*, vol. 22(3), pp. 379–392, 1991.
[4]. M. Kaczorowska, M. Plechawska-Wojcik, M. Tokovarov, i R. Dmytruk, „Comparison of the ICA and PCA methods in correction of EEG signal artefacts”, w *2017 10th International Symposium on Advanced Topics in Electrical Engineering (ATEE)*, 2017, pp. 262–267.
[5]. A. Mirifar, J. Beckmann, i F. Ehrlenspiel, „Neurofeedback as supplementary training for optimizing athletes' performance: A systematic review with implications for future research”, *Neurosci. Biobehav. Rev.*, vol. 75, pp. 419–432, kwi. 2017.
[6]. G. Cheron *i in.*, „Brain Oscillations in Sport: Toward EEG Biomarkers of Performance”, *Front. Psychol.*, vol. 7, pp. 246, 2016.
[7]. T. P. Zieliński, *Cyfrowe przetwarzanie sygnałów: od teorii do zastosowań*, 2. wyd. Warszawa: Wydawnictwo Komunikacji i Łączności, 2014.
[8]. L. Zaichkowsky, Red., „Psychophysiology and Neuroscience in Sport: Introduction to the Special Issue”, *J. Clin. Sport Psychol.*, vol. 6(1) , pp. 1–5, mar. 2012.
[9]. B. DeMichelis, „AC Milan's «Mind Room» and sport psychology”, zaprezentowano na 11th annual meeting of the Biofeedback Foundation of Europe, Berlin, 2007.
[10]. M. Mikicin, „The autotelic involvement of attention induced by EEG neurofeedback training improves the performance of an athlete's mind”, *Biomed. Hum. Kinet.*, vol. 7(1), cze. 2015.
[11]. D. M. Landers *i in.*, „The influence of electrocortical biofeedback on performance in pre-elite archers”, *Med. Sci. Sports Exerc.*, vol. 23(1), pp. 123–129, sty. 1991.
[12]. J. H. Gruzelier, „EEG-neurofeedback for optimising performance. I: a review of cognitive and affective outcome in healthy participants”, *Neurosci. Biobehav. Rev.*, vol. 44, pp. 124–141, lip. 2014.
[13]. J. H. Gruzelier, „EEG-neurofeedback for optimising performance. II: creativity, the performing arts and ecological validity”, *Neurosci. Biobehav. Rev.*, vol. 44, pp. 142–158, lip. 2014.
[14]. J. H. Gruzelier, „EEG-neurofeedback for optimising performance. III: a review of methodological and theoretical considerations”, *Neurosci. Biobehav. Rev.*, vol. 44, pp. 159–182, lip. 2014.
[15]. A. Ziółkowski, M. Graczyk, A. Strzałkowska, D. Wilczyńska, P. Włodarczyk, i Zarańska B., „Neuronal cognitive and social indicators for the control of aggressive behaviors in sport.”, *Acta Neuropsychol*, no. 10, pp. 537–546, 2012.
[16]. I. Shaw, L. Zaichkowsky, i V. Wilson, „Setting balance: using biofeedback and neurofeedback with gymnasts”, *J. Clin. Sport Psychol.*, no. 6, pp. 47, 2012.
[17]. S.-C. Kao, C.-J. Huang, i T.-M. Hung, „Neurofeedback Training Reduces Frontal Midline Theta and Improves Putting Performance in Expert Golfers”, *J. Appl. Sport Psychol.*, vol. 26(3), pp. 271–286, lip. 2014.
[18]. C. Ring, A. Cooke, M. Kavussanu, D. McIntyre, i R. Masters, „Investigating the efficacy of neurofeedback training for expediting expertise and excellence in sport”, *Psychol. Sport Exerc.*, vol. 16, pp. 118–127, sty. 2015.
[19]. M.-Y. Cheng, C.-J. Huang, Y.-K. Chang, D. Koester, T. Schack, i T.-M. Hung, „Sensorimotor Rhythm Neurofeedback Enhances Golf Putting Performance”, *J. Sport Exerc. Psychol.*, vol. 37(6), pp. 626–636, grudz. 2015.

Piotr Cheluszka[1], Jacek Gawlik[1], Grzegorz Głuszek[1], Piotr Sobota[1]

ASSESSMENT OF WEAR AND TEAR OF NEW GENERATION SPROCKET DRUM OF ARMOURED FACE CONVEYORS MADE OF ADI ALLOY CAST IRONS

Keywords: armoured face conveyor (AFC), sprocket drum, ADI alloy cast iron, wear and tear, measurements of the geometry of the seats

Abstract

Scraper conveyors are widely used in many industries for transport of bulk materials. In underground mining they belong to a group of basic transport devices. The critical elements in the powertrain for the chain are sprocket drums. The low durability of sprocket drums, which, so far, are made in a form of steel castings, means that they must be replaced many times during the operation. In order to improve the durability of sprocket drums, as a part of a research project carried out in the Department of Mining Mechanization and Robotisation at the Silesian University of Technology in cooperation with Ryfama (Famur S.A.), a new generation of sprocket drums has been developed. One of the innovative ideas was the use of ADI alloy cast iron for casting sprocket drums. In order to check their suitability, a sprocket drum was installed in an armoured face conveyor (AFC) operating in one of the Polish hard coal mines. It was exploited for 2 years until the conveyor was removed from use. This chapter presents the results of measurements of the geometry of seats of the sprocket drum made of ADI after its use in the AFC. The measurements were made using a structural light scanner installed on an industrial robot's arm. The aim of the work was to assess sprocket drum wear based on a comparison of its geometry with the new drum geometry.

1. Introduction

Scraper conveyors are widely used in many industries for transport of bulk materials (eg. in power stations and in heat and power stations for transport of solid fuels and slag, or in cement, chemical and fertilizer plants). In underground mining, including hard coal mining, they belong to a group of basic transport devices, which are an important element of the spoil haulage system. Thanks to their simple, modular construction, high resistance to environmental factors and the ability to work at high inclinations, they are widely used in particularly difficult operating conditions. In longwall mining systems for solid minerals used in hard coal mining or potassium salt, scraper conveyors – armoured face conveyor (AFC) and beam stage loader (BSL) are a part of mechanized complexes. The armoured face conveyor (figure1), located parallel to the face of a longwall, is used not only for transport of spoil, but also fulfills many important

[1] Silesian University of Technology, Faculty of Mining, Safety Engineering and Industrial Automation, Department of Mining Mechanization and Robotisation, 2 Akademicka Street, 44–100 Gliwice, Poland, Piotr.Cheluszka@polsl.pl

functions (including a track for a cutting machine and a kinematic bond for roof supports). In Polish hard coal mining, AFC of a length of about 250 meters are driven by electric motors with a total power *P* exceeding 1000 kW (most often 3×400 kW, 3×315 kW or 2×400 kW). The high-efficiency longwall systems are now equipped with AFC with engine power *P* exceeding 2500 kW [9]. The drive power of longwall conveyors designed for working in longwall works up to 500 m long and can reach up to 3×1800 kW. In this way, transport efficiency *Q* up to 6200 t/h [1] is assured.

The physicochemical properties of rock output with different grain size and the operating principle of the scraper conveyor (chain links equipped with scrapers are moved along the pans) make it subject to intensive abrasive wear [2],[8]. Sprocket drums are critical elements in transferring the drive onto the chain. The interaction of chain links with sprocket drums makes them wear out quickly. This leads to interference in tooth meshing process, as a result of which chain links may jam and, in extreme cases, jump over the teeth of the sprocket drum [11],[14]. The low durability of sprocket drums, which are, so far, made in a form of steel castings, means that they must be replaced many times during the operation of a conveyor. This generates additional costs, and in the event of a failure – unplanned shutdowns of the entire technological system.

In order to improve the durability of sprocket drums used in high–efficiency mining scraper conveyors, as a part of a research project carried out in the Department of Mining Mechanization and Robotisation of the Faculty of Mining, Safety Engineering and Industrial Automation at the Silesian University of Technology in cooperation with Ryfama (Famur S.A.), a new generation of sprocket drums has been developed. Due to the complicated stereometry resulting from the nature of the interaction of sprocket drum sockets with chain links, sprocket drums are currently made in the form of cast steel or forgings, in the form of uniform wreaths or split elements. One of the innovative ideas was the use of ADI alloy cast iron for casting sprocket drums. The ADI (Austempered Ductile Iron) is a construction material obtained as a result of heat treatment of ductile iron castings. This kind of treatment forms the base of the cast iron in such a way that a specific phase mixture consisting of plate ferrite and austenite is formed. It provides a good combination of strength and plastic properties and high wear resistance, giving the opportunity to replace cast steel and surface hardened steel [10],[15].

This chapter presents the results of measurements of the geometry of seats of the sprocket drum made of ADI after its use in the AFC for a period of two years. The measurements were made using a structural light scanner installed on an industrial robot's arm. The basis for assessing the wear and tear of the sprocket drum was to compare its geometry with the geometry of a new drum. The purpose of measurements was to determine the usefulness of ADI cast iron for the production of sprocket drums in terms of increasing their durability.

2. Interaction of the chain with the sprocket drum of the scraper conveyor

Among the AFCs used in the underground coal mining conveyors with head and tail drive dominate, equipped with two central chains (the right and the left one). Scrapers that move spoil are attached to horizontal links with clamps. Chain movement is caused by conveyor drives via sprocket drums (figure2). The interaction of sprocket drums with two central chains connected with scrapers is the source of additional loads on teeth and drums sockets resulting from the weight of moving scrapers, the mass forces acting on them during the rotation on the sprocket drum and side loads caused by the rigid connection of chains with scrapers.

The link chain in the aspect of interaction with sockets of a sprocket drum consists alternately of active horizontal and passive vertical links. Both the horizontal and vertical links have the shape of flattened rings, in which two toruses (front and back) and two rolls can be distinguished. When analyzing the interaction of the sprocket drum with the link chain, the most important parameters of links are the chain pitch *t* meaning the internal length of the link, and the thickness of the link *d* meaning the diameter of the rod from which the link is made. The shape of links of the chain means that the interlocking notches of the sprocket drum, which are adapted to this type of chain, have the form of sockets. The horizontal links of the chain are arranged in these sockets, while the vertical links occupy the position in tooth grooves. For this reason, sprocket drum teeth are not uniform, but consist of segments that rear toruses of the horizontal links are in contact with.

Fig. 1. A scraper conveyor (AFC) installed in the longwall of a coal mine [18]

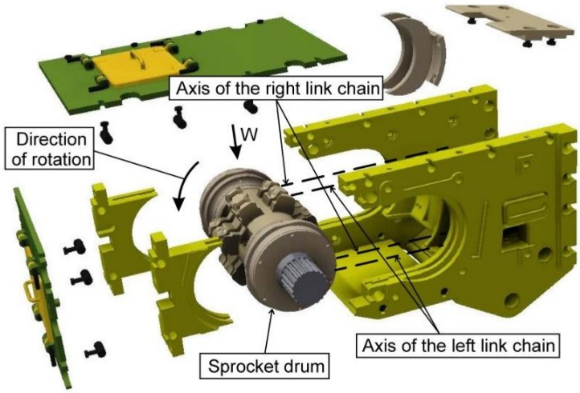

Fig. 2. The drive frame with visible sprocket drum (based on [13])

The bottom of the socket is also not uniform, as it is separated by a longitudinal tooth groove, in which vertical links of the chain are arranged. In addition, in the middle part of the bottom of the socket there is a transverse scraper groove. Practically, the bottom of the socket consists of four fragments of the plane, each with a small surface area (figure3). The front (non–working) flanks (1R, 2R, 1L & 2L) cooperate with the front torus of the horizontal link, while the rear (working) flanks of the tooth (3R, 4R, 3L & 4L) cooperate with the back torus of the horizontal link.

The conducted wear research in connection with the analysis of the dynamic load conditions and the stress in interlocking of the sprocket drum with the link chain clearly indicate that high stress concentrations and the accompanying abrasive wear occur in certain characteristic nodes of the sockets of the sprocket drums [4],[6],[7]. Their location results closely from the way these elements work together. The slipping of the front torus of the chain on the limited surface of the bottom of the socket is accompanied by high pressure and friction forces, which determine the abrasive wear of the front part of the bottom of the socket. The rear part of the bottom of the socket and the flank of teeth on the working side are also worn down in the point of contact of these elements with the back torus of horizontal links [12]. The direction of movement of the scraper chain transporting spoil determines the basic direction of rotation of the sprocket drum. This causes the asymmetrical wear of bottoms of sockets and flanks of teeth.

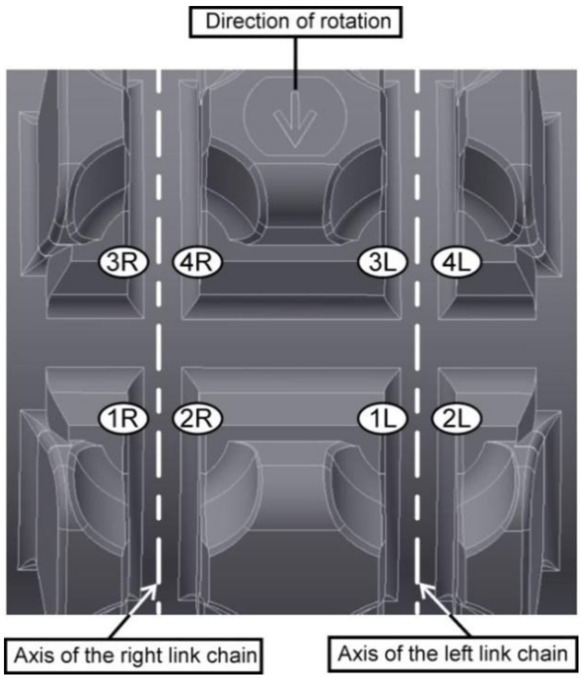

Fig. 3. View of two adjacent sockets of the sprocket drum (view "W" from Fig. 2) with tooth flank markings: 1 – front right, 2 – front left, 3 – rear right, 4 – rear left, R – right link chain, L – left link chain

The forces acting on the bottom of sockets and on the working flanks of teeth depend on the value of force in the branch of the chain running on the sprocket drum. The higher the value of the force transmitted by chain links running on the sprocket drum the higher the value of all reactions between the horizontal link entering into the meshing and the bottom of the socket and the flank of the tooth [6],[12].

3. Measurement of stereometry of sprocket drums with the use of a structural light scanner

The research object was a sprocket drum made of ADI cast iron. It was designed to cooperate with two center link chains, size 34×126 mm (with pitch t = 126 mm and thickness of the link d = 34 mm). In order to check the suitability of ADI cast iron, the sprocket drum was installed in an AFC operating in one of the Polish hard coal mines. It was exploited in three mining walls (in two of them in the head drive, and in the third wall in the ail drive until the conveyor was removed from use). During this time, this conveyor transported about 1,400,000 tonnes of coal.

For the purpose of analyzing the wear intensity of the sprocket drum made of ADI cast iron, its geometry was measured before and after its operation. Due to the complicated stereometry of sprocket drums, for the measurement of their geometry, or current monitoring of technical condition, non–contact methods based on the image analysis obtained, e.g. from the vision system are extremely useful [5]. Hence, determination of operational wear and tear of the new generation of the sprocket drum was based on the comparison of grids built on the surface of the new drum and after its exploitation, obtained as a result of 3D scanning.

The automated scanning process was carried out on a robotic measuring stand in the laboratory of the Department of Mining Mechanization and Robotisation at the Silesian University of Technology [3], which was equipped with a robot KR–16–2 on a linear unit KL 250–3 [20] (figure 4a) (manufactured by KUKA Roboter). A smartSCAN 3D–HE structural light scanner [21] (manufactured by Breuckmann–Aicon) was attached to the robot's arm. The scanning object was placed on a turntable with a vertical axis of rotation PEV–1–2500 (produced by ZAP Robotics), which changed its position as the scan progressed. Data acquisition and their initial processing after the completion of the scanning process was carried out in the OptoCAT – the dedicated software for Breuckmann–Aicon scanners (figure 4b).

For the purpose of scanning sprocket drums, a suitable program was developed, invoked from the internal memory of the robot control system. For each positioning of the turntable, 14 scans were performed with different robot's arm positions. These scans were automatically combined in the OptoCAT environment, as a result of which a grid was obtained that mapped the shape of the surface of the object being scanned. The surface of the sprocket drum reconstructed in this way was subjected to a treatment aimed, among other things, at cleaning it of unnecessary background elements and patching holes created in the scanning process. The obtained 3D model, for the needs of further processing, was saved in the "stl" format enabling its import into CAD and metrology programs. The analysis of the size and distribution of teeth and sockets of the sprocket drum wear and tear was carried out in the metrology software GOM Inspect Professional [19].

a) b)

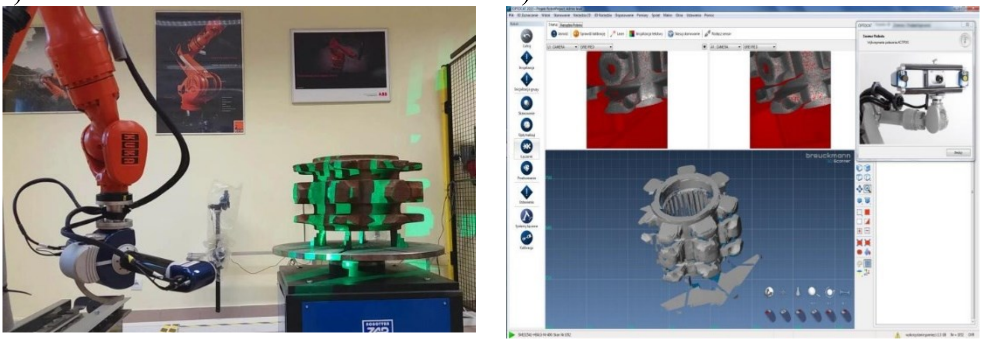

Fig. 4. Scanning the sprocket drum on a robotic stand equipped with a structured light scanner (a) and a window view of the dedicated OptoCAT software for data acquisition and processing (b)

4. Analysis of wear and tear of the new generation sprocket drum for AFC

The meshing of links of the chain with teeth of the sprocket drum and disengaging of links in the conditions of the slip of links on the tooth flank are accompanied by significant pressure and friction forces having a decisive impact on the drum teeth wear. Bottoms of sockets also undergo abrasive wear during the contact with toruses of links. The effect of the long–term interaction of horizontal links with bottoms of sockets is the deformation of the bottom of the socket and the flank of teeth. This is disclosed by tooth wear maps of sprocket drums (figure 5) obtained as a result of overlapping grids imaging the surface of the drum after removal from use and a new drum. There are visible areas of particularly high wear, reaching up to 10 mm. These areas (in red) concentrate on the bottom of sockets, especially on the side of the working part of the teeth and on the rear flank of the teeth (for the situation shown in figure 5 this is the right side of each of sockets).

From the point of view of the correct cooperation of link chains with sprocket drums and the preservation of sufficient meshing efficiency, in practice, two values determine the degree of abrasive wear of the drums:

- decrease in thickness of the teeth, which results in an increase in the length of sockets cooperating with horizontal links,
- lowering of the position of the bottom of the drum socket (decreasing the distance of the bottom of the socket from the axis of rotation of the drum), which results in reducing the length of sockets cooperating with horizontal links.

Other wear, corrosion and abrasive–corrosion defects in the practical operation of sprocket drums are of secondary importance and may either be omitted or taken into account when assessing the degree of wear and tear only on a subsidiary basis.

To determine the reduction in thickness of the teeth, values of sockets wear on rear flanks and front flanks of the teeth were determined. The rear (working) flanks of the teeth transfer the load to the back toruses of the horizontal links. The frontal (non–working) flanks come into contact with front toruses of horizontal links when the chain engages and disengages.

In order to determine the distribution of wear on the surface of sockets and flanks of the teeth, cross–sections were made in planes perpendicular to the axis of rotation of the sprocket drum, spaced every one millimeter. In a given section, wear was determined for each tooth flank as the distance between the outlines of new and used drum measured perpendicular to the cross–sectional line at a given location (measuring point). On this basis, average values were determined for wear of all seven sockets in a given cross–section of the sprocket drum, the rear flank and the front flank cooperating with the right link chain and the left link chain (figure 6). The continuous lines show the tooth flank wear curves cooperating with the right link chain and the dashed lines – the wear of flank teeth cooperating with the left link chain (see figure 3). The lines in blue refer to the wear of the rear flank of the tooth, while the lines in red refer to the wear of the front flank of the tooth.

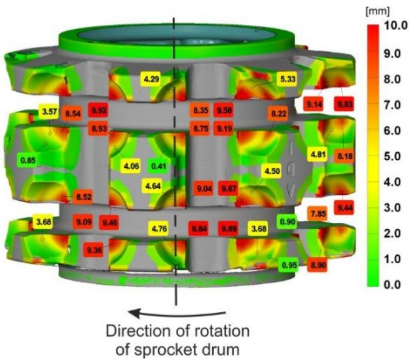

Fig. 5. Map of wear distribution of sockets and flanks of teeth of sprocket drum made of ADI cast iron

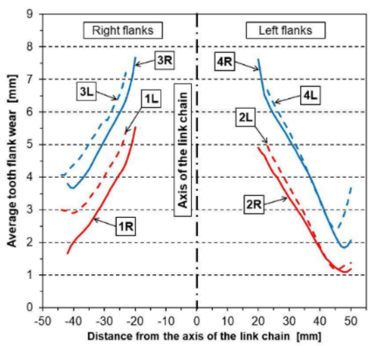

Fig. 6. The average wear of teeth of the sprocket drum made of ADI cast iron as a function of the distance of the cross–sections from the axis of the link chain

The highest values of teeth wear occur on their edge at the tooth groove in which the vertical links of the chain are located. As the analyzed section moves away from the tooth groove (link chain axis), the average consumption values decrease considerably. This is due to the geometrical relationship of drum sockets and horizontal links of the chain. To avoid the horizontal link jamming in the drum socket, the flank teeth have a larger radius of curvature from the radius of the link's torus (for the analyzed chain size 34×126 mm, the radius of curvature of the teeth segments is 55 mm with the width of tooth groove of the 45 mm, and the radius of the torus is 52 mm (according to standards: [16],[17]). This results in a point contact of the back horizontal link torus with tooth segments on the edge at the tooth groove in the new drum. As the wear increases, the curvature of the flank adjusts to the shape of the torus and contact of these elements becomes linear and the wear extends over the wider tooth width. The farther away from the tooth groove (the link chain axis), the smaller the wear. While at the edge of the tooth groove the wear on the rear flanks (3R, 4R, 3L & 4L) was about 6 ÷ 7.5 mm, at a distance of 10 mm from the groove it was about 5 mm, and at a distance of 20 mm from the groove it was less than 4 mm. The average wear of the front flank (1R, 2R, 1L & 2L), with less contact with links at the high load, is clearly smaller by 1.5÷2.0 mm. The wear of teeth cooperating with the left link chain has the same character as of those cooperating with the right link chain. However, while the average values of the left tooth flank wear (2R & 2L, 4R & 4L) are not much different for the right and the left link chain, the wear of the right flank of the teeth interacting with the left link chain (1L & 3L – dashed lines) is greater by about 1 mm than the wear of right flanks of teeth cooperating with the right link chain (1R & 3R – solid lines). This applies to both rear and front flanks of teeth. The reason for this situation may be the conveyor's operation in a transversely inclined wall, when the chain is pressed with the force of gravity to one side of the drum.

figure 7 shows distributions of teeth wear of the tested sprocket drum. All four flanks of seven teeth cooperating with the right link chain (a÷d) and the left link chain (e÷h) were analyzed separately (a total of approximately 1.8 million measurement points). The wear and tear distributions of front (non–working) and rear (working) flanks of the examined sprocket drum are clearly different. In addition, the share of wear in the specified variability ranges for right and left flanks is different. Certain differentiation can also be seen in the case of sockets cooperating with the right and the left link chain.

In the case of front flanks, the largest share was in the range of:

- from 2 to 3 mm – right flanks (1R & 1L) – 18% and 23%, respectively
- from 1 to 2 mm – left flanks (2R & 2L) – about 27 ÷ 28%.

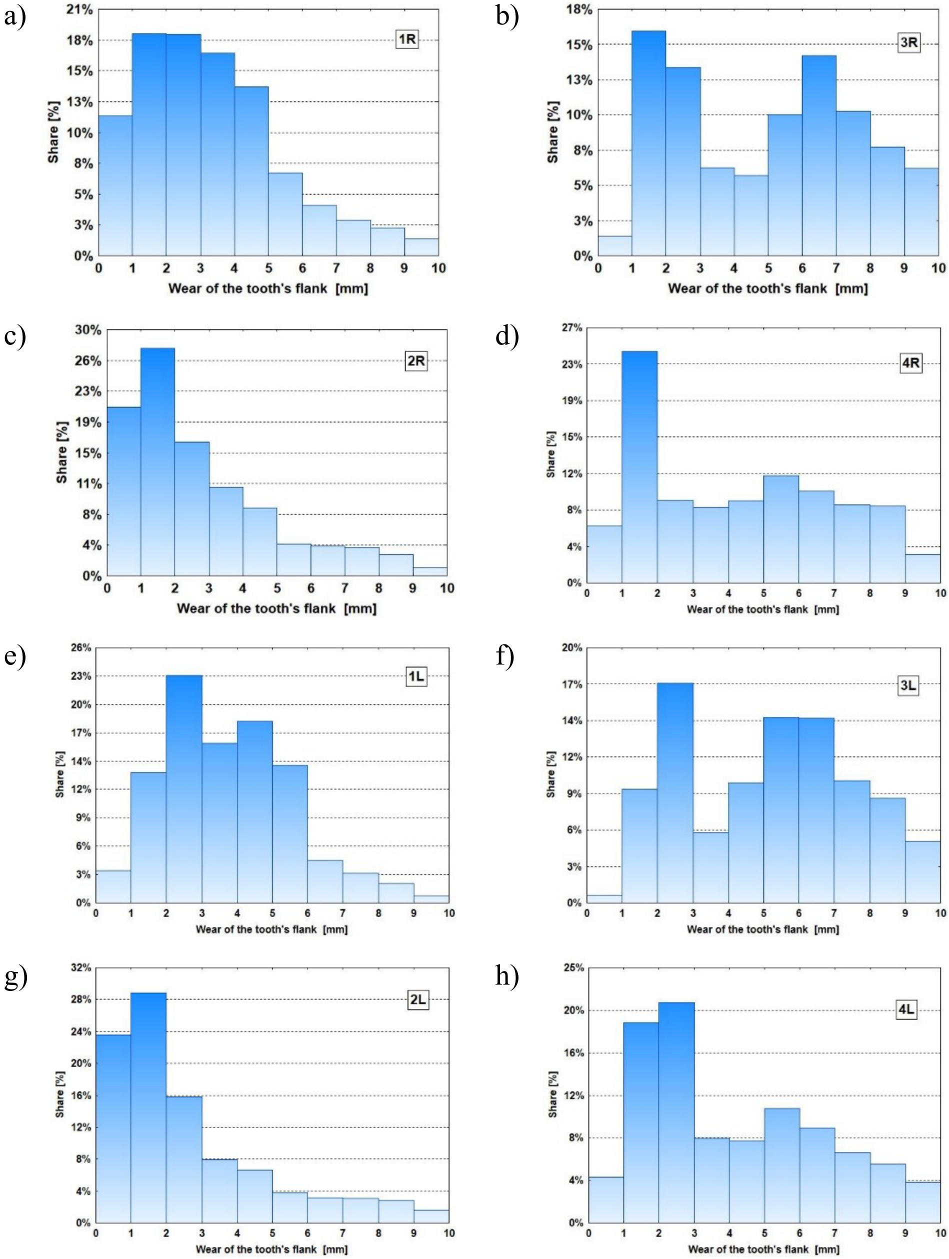

Fig. 7. Histograms of tooth flank wear of sprocket drum made of ADI cast iron: a) front right – right link chain, b) rear right – right link chain, c) front left – right link chain, d) rear left – right link chain, e) front right – left link chain, f) rear right – left link chain, g) front left – left link chain, h) rear left – left link chain

Distributions of wear values in both mentioned cases differ. In the case of right flanks, the wear of 1 to 5 mm or even 6 mm has the largest share. For approximately 70% of the measuring points located on the surface of these parts of drum sockets interacting with the right link chain (figure 7a) and the left link chain (figure 7e), the wear was within 1 to 5 mm. These distributions are asymmetrical (right–sided), which means that the wear is of a relatively small value. In the case of left flanks, for about 2/3 of the measuring points distributed on these surfaces of the drum socket, the wear did not exceed 3 mm (figure 7c & figure 7g). Distributions of the value of the examined quantity are similar to the exponential distribution.

The wear and tear distributions on working flanks (rear) of teeth have a completely different character (figure 7b, d, f, h). In the case of right flanks, the distribution of the surface area of sockets of the tested sprocket drum is bimodal. The share of points in which the wear was between 1 and 3 mm and between 6 and 7 mm (figure 7b & figure 7f) was clearly larger in relation to the share for the remaining separated wear of the surface of sprocket drum sockets' intervals. In turn, for the left flank of teeth the largest share of the wear was:

- from 1 to 2 mm – for sockets cooperating with the right link chain (~25%) – figure 7d,
- from 1 to 3 mm – for sockets cooperating with the left link chain (40%) – figure 7h.

The bimodal distribution of working (rear) flanks of teeth resulted from the fact that, apart from the small wear (<3 mm) of the sides of sockets on a relatively large surface, there was increased wear, especially in the area of the tooth groove (about 5 – 7 mm).

Tab. 1. Summary of basic values statistics of wear and tear for sockets of a sprocket drum made of ADI cast iron

Right link chain					Left link chain				
Name of the tooth's flank	MIN	MAX	Average	Std. dev.	Name of the tooth's flank	MIN	MAX	Average	Std. dev.
	[mm]					[mm]			
1R	~0	18.0	3.5	2,5	1L	~0	29.9	3.9	2.1
2R	~0	29.9	2.9	2,6	2L	~0	18.6	2.9	2.6
3R	~0	29.0	5.4	3,1	3L	~0	29.5	5.6	3.0
4R	~0	29.7	4.6	3,2	4L	~0	21.5	4.4	2.9

The average values of the wear of working (rear) flanks of sprocket drum teeth cooperating with both link chains were at the level of 5.4 – 5.6 mm (for the right flanks) and 4.4 – 4.6 mm (for the left flanks) (table 1). The standard deviation of the flank wear of teeth was approximately 3 mm. In turn, the average wear of flank surfaces of non–working (front) teeth flanks was in the range from 3.5 to 3.9 mm (right flanks) and up to 2.9 mm – in the case of left flanks. The standard deviation was somewhat smaller in this case, since it ranged from 2.1 to 2.6 mm. As it has already been stated, the higher average values of wear of right flank surfaces (cooperating with both the left and the right link chain) could be due to the transverse slope of the conveyor.

From the point of view of wear of sprocket drums, in addition to the thinning of teeth, wear of the bottom of sockets is of particular importance in practice. It causes the horizontal links to reposition in sockets, as a result of which they do not lie on the entire surface of the socket bottom but are inclined relatively to the bottom of the socket. The back torus links of the chain recline on rear flanks of drum teeth above the bottom of the socket. This increases the probability of the torus slipping of the back horizontal link on the rear tooth flank and prolongs the friction path during this slip, thus increasing the wear. The length of the socket decreases, which results in the possibility of blocking the horizontal links in the socket, forcing ejectors of the chain to support the disengagement of links. Forced link disengagement during the work of chain ejectors causes slippage of the horizontal link on both the rear and the front flank of the tooth, dramatically increasing the wear of these surfaces.

In order to assess the size of the wear and tear of the bottom of the socket, cross–sections of superimposed reconstructed surfaces of the sprocket drum were made with radial planes passing through the axis of rotation of the drum. The planes were led at angular intervals of 0.5°, which corresponds to the arrangement of subsequent cross–sectional lines of socket of 2.2 mm. In each cross–section, the average values of the socket bottom wear measured perpendicular to its surface were determined. The location of particular cross–sections is determined by the angular distance measured from the axis of the scraper groove (from –11° to –18° for the front part of the socket and from +11° to + 18° for the rear part of the slot) – figure 8. The continuous lines denote the wear of bottoms of the socket cooperating with the right link chain, and the dashed lines – the wear of the socket cooperating with the left link chain. Red lines refer to the wear of the right part of the socket, while the lines in green refer to the wear of the left part of the socket.

The largest values of the wear of bottoms of sockets occur on the edge of the bottom at the scraper groove. As the cross–section travels away from the scraper groove, the average wear values decrease rapidly in the front and the rear of the socket. While at the edge of the scraper groove, the average wear of the front part of the socket was about 7 ÷ 8 mm, and about 6 ÷ 7 mm in the rear part of the socket, at a distance of 10 mm from the scraper groove the wear of both parts of the socket did not exceed 5 mm. The average wear of the front part of the socket was larger at the edge of the scraper groove, and the wear at the base of the tooth was smaller than at the rear of the socket. The wear of bottoms of the sockets cooperating with the left link chain had the same character and similar value to the ones cooperating with the right chain.

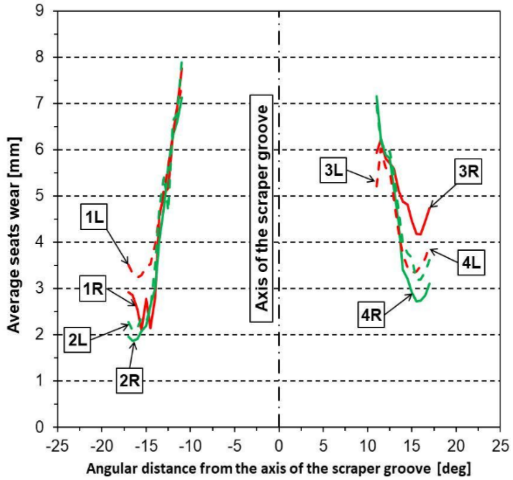

Fig. 8. Average wear of the teeth of the sprocket drum made of ADI cast iron as a function of the angular distance of the cross-sectional plane of the drum from the scraper groove

5. Conclusions

The results of measurements of the wear and tear of a new generation of sprocket drums for high efficiency armoured face conveyors presented in this paper have confirmed significant advantages resulting from the material used. The material properties of ADI cast iron, including an ability of the casting surface to cure under the influence of an external load, meant that the wear of sockets of the tested sprocket drum did not exceed the value requiring its replacement in a much longer period of use than for conventional drums. This drum was operated on the runway of three longwalls in the period of two years. The size and nature of the wear indicate that it could be used again.

Material losses at the rear working flank of tooth, which do not exceed 4 mm at a distance of 20 mm from the tooth groove, indicate that the sprocket drum can be further used in the next longwall work. The ability to cure the surface of the cast, made of ADI cast iron, under the influence of external forces, guarantees the wear of teeth at a similar rate to the current rate. Conventional drums made in the form of cast steel castings, after working for an average of 4 to 6 months, must usually be replaced with new ones due to excessive abrasion of sockets preventing their proper cooperation with the chain. Under the guarantee of the conveyor manufacturer for transporting 2 million tonnes of spoil, two sprocket drums are replaced on average, so that the guaranteed mass of transported material is carried out by three drums in each conveyor drive. On average, therefore, the durability of conventional drums allows to transport only about 400,000 ÷ 600,000 t coal mined. After the clash of the hardened layer, obtained as a result of the surface hardening to a depth of 5 ÷ 7 mm, the abrasive wear proceeds at a rapid pace. When using ADI cast iron, this problem does not occur due to the above–mentioned properties of this type of material. **Based on the analysis of the measurement results, it was found that the durability of the new generation of sprocket drums made of ADI cast iron is at least 3 times higher than in the case of conventional steel drums.**

References

[1] Caterpillar Performance Handbook. Edition 47, January 2017, Peoria, Illinois, U.S.A., pp. 2440 [https://www.macallister.com/parts-service/caterpillar-performance-handbook/] (access date: 18.06.2019).

[2] H. Chen and R. Wang, "Study on Wear of Scraper Conveyor Chute", *Proceedings of the International Conference on Intelligent Systems Research and Mechatronics Engineering* (ISRME 2015), , Zhengzhou, China, pp. 2254–2257, April 2015.

[3] P. Cheluszka and M. Nocoń, "Robotised digitalisation technology of roadheader working units for the purpose of manufacturing quality control", *Surface Mining*, vol. 56, no. 6, pp. 11–23, 2015 (in Polish).

[4] P. Cheluszka and B. Sygit, "Measurements of wear and tear of sprocket drum seats of high–performance armoured face conveyor", *Polish Mining Review*, vol. 72, no. 7, pp. 8–19, 2016 (in Polish).

[5] H. Ding, Y. Liu and J. Liu, "Volumetric Tooth Wear Measurement of Scraper Conveyor Sprocket Using Shape from Focus-Based Method", *Applied Sciences*, 9, 1084, 2019, DOI 10.3390/app9061084.

[6] M. Dolipski M., E. Remiorz E. and P. Sobota, "Determination of dynamic loads of sprocket drum teeth and seats by means of a mathematical model of the longwall conveyor", *Arch. Min. Sci.*, vol. 57, no. 4, pp. 1101–1119, 2012, DOI 10.2478/v10267-012-0073-7.

[7] S.B. Jiang, Q.L. Zeng, G. Wang; K.D. Gao, Q.Y. Wang and K. Hidenori, "Contact analysis of chain drive in scraper conveyor based on dynamic meshing properties", *Int. Journal of Simulation Modelling*, vol. 17, no. 1, pp. 81–91, 2018.

[8] J. Krawczyk and B. Pawłowski, "The analysis of the tribological properties of the armoured face conveyor chain race", *Arch. Min. Sci.*, vol. 58, no. 4, pp. 1251–1262, 2013, DOI 10.2478/amsc-2013-0086.

[9] K.B. Ramesh, S. Chandrasekhar and R.B Veera "Construction and operation of high capacity longwall project – Adriyala experience", *Proceedings of the conference on Recent Advances in Rock Engineering* (RARE 2016), pp. 56–63, Bengaluru, India, November 2016.

[10] B. Mrzygłód, A. Kowalski, I. Olejarczyk–Wożenska, T. Giętka and M. Głowacki, "Characteristics of ADI ductile cast iron with single addition of 1.56% Ni", *Arch. Metall. Mater.*, vol. 62, no. 4, pp. 2273–2280, 2017, DOI 10.1515/amm-2017-0335.

[11] F. Ren, A.Q. Shi and Z.J. Yang, “Research on load identification of mine hoist based on improved support vector machine”, *Trans. Can. Soc. Mech. Eng.*, vol. 42, no. 3, pp. 201–210, 2018.
[12] P. Sobota, “Determination of the friction work of a link chain interworking with a sprocket drum”, *Arch. Min. Sci.*, vol. 58, no. 3, pp. 805–822, 2013, DOI 10.2478/amsc-2013-0056.
[13] S. Tytko, M. Łabęcki, S. Gros, “State–of–the–art integrated fligt–bar conveyors manufactured by RYFAMA S.A.”, *Mining Machines*, vol. 30, no. 3, pp. 31–38, 2012 (in Polish)
[14] S.P. Wang, Z.J. Yang and X.W. Wang, “Wear of driving sprocket for scraper convoy and mechanical behaviors at meshing progress” *Journal of the China Coal Society*, vol. 39, no. 1, pp. 166–171, 2014, DOI 10.13225/j.cnki.jccs.2013.0125.
[15] A.N. Wieczorek, “Comparative studies on the wear of ADI alloy cast irons as well as selected steels and surface–hardened alloy cast steels in the presence of abrasive” *Arch. Metall. Mater.,* vol. 62, no. 1, pp. 119–128, 2017, DOI 10.1515/amm-2017-0016.
[16] PN–G–46701:1997, Łańcuchy ogniwowe górnicze.
[17] PN–G–46703:1997, Łańcuchy ogniwowe górnicze – Bębny i koła łańcuchowe gniazdowe – Wymagania.
[18] http://miningst.com/longwall-mining/equipment/armoured-face-conveyor/ (access date: 18.06.2019).
[19] https://www.gom.com/ (access date: 18.06.2019).
[20] www.kuka.com (access date: 18.06.2019).
[21] http://skanerybreuckmann.pl/skanery/3/smartscan (access date: 18.06.2019).

Witold Rzymowski[1]*, Agnieszka Surowiec*[2]

FRACTAL DIMENSION IN TIME SERIES ANALYSIS

Keywords: fractals, fractal dimension, Hölder exponent, exchange rates, computer modelling

Abstract

Time series can be used by the specialists in many sciences, not only mathematicians, physicists and computer scientists, recently, also specialists in the field of finance to modelling any processes and phenomena which involves temporal measurement e.g. weather forecasting, earthquake prediction, power demand forecasting or exchange rate prediction.

A concept of the fractal dimension as a measure of variability of a time-series graph of exchange rates is presented in this paper. Two methods of calculating the fractal dimension of time-series graph are described. The first method is the most known box method by Kolmogorov, the second one is a new method that uses the Hölder exponent. The paper contains the results of computer modelling the values of analysed exchange rates of some currencies with use the fractal dimensions obtained in above-mentioned methods in 2000-2016 period.

1. Introduction

The developments in science and computer technology improve the effectiveness of data analysis. However, an accurate prediction of the future course of events is still largely impossible. New and still relatively undeveloped theories suggest that determinism and an apparently random course of events are not mutually exclusive but co-exist [1]. Fractal geometry is one of these theories.

Benoit Mandelbrot, in his work "How long is the coast of Britain? Statistical self-similarity and fractional dimension" [2], introduced the concept of fractals and fractal dimension. He claimed that everything is a fractal and shapes such as rectangles, circles and triangles are artificially created in order to simplify the description of the surrounding world. The concept of the fractal dimension has been introduced as the measure of the complexity of the shapes surrounding us. The fractal dimension defines the curve winding level and, in some sense, the amount of space containing this curve that is filled [3]. In order to define the fractal's dimensionality Mandelbrot simplified the definition of a dimension formulated by Hausdorff in 1919. His definition strictly corresponds to the

[1] Lublin University of Technology, Fundamentals of Technology Faculty, Department of Applied Mathematics, Nadbystrzycka 38, 20-618 Lublin, Poland, w.rzymowski@pollub.pl

[2] Lublin University of Technology, Faculty of Management, Department of Quantitative Methods in Management, Nadbystrzycka 38, 20-618 Lublin, Poland, a.surowiec@pollub.pl

volumetric/capacitive definition of dimension developed by Kolmogrov in 1958 [4]. While, in the case of classic shapes, the dimension is an integer number, in fractal dimension it is usually a non-integer.

It was immediately revealed that the chaos theory and fractal geometry are applicable in many areas of life i.e. finances.

Recently, we observed a large variety of methods used in financial data analysis, especially in financial time-series analysis. There were many publications on the modelling of the financial time-series using selected fractal methods [5-14]. Conducting time-series analysis of e.g. prices of securities or currency exchange rates, where the plot of the price versus time usually transforms into double logarithmic plot, a scaled range analysis method is used [12]. Possible measures of the plot regularity are e.g. Hurst exponent [15-18] or Minkowski's dimension [18]. In our work, we do not apply the scaled range analysis method, as it was resolved that the Hölder exponent should be introduced as the measure of the variation of the currency exchange plot, which is a number in range (0, 1). The Hölder function and the Hölder exponent are frequently used in the works of Polish authors [12,19]. As the Hölder exponent approaches zero, the variability of a process is higher. Contrarily, the process is smoother for the exponent values closer to one. Given that the Hölder exponent is $\gamma \in (0,1)$ then the fractal dimension of the Hölder series $(x_t)_{t=1}^{\infty}$ is a number [21]:

$$\dim(x_t)_{t=1}^{n} = 2 - \gamma , \tag{1}$$

which follows that the fractal dimension of the plot is a number in the range (1, 2).

As the Hölder exponent determines the process properties, similarly, the fractal dimension is the measure of the process variability. The fractal dimension of the time-series plot gives the information on how frayed the plot is, in other words, the degree to which it fills the plane [4].

The aim of our paper is to present the potential of modelling the exchange rates of the selected foreign currencies based on the selected methods and concepts of fractal geometry. Using the fractal dimension, with the help of the chaos theory and the fractal geometry, we analyse the time development of the exchange rates based on the data from 2001-2016. The data collected in 2016 were used to verify the model based on the data from 2015 and the model obtained from the data recorded in the period from 2001 to 2015. The fractal dimension is defined by the Hölder exponent of the Hölder sequence using the "box-counting method" (procedure I) [4] and averaging method (procedure II). Moreover, we investigated which of the presented methods of determining the fractal dimension is more successful at modelling the currency exchange rates.

In the work, we analysed 13 foreign currencies: US dollar, Australian dollar, Canadian dollar, euro, Hungarian forint, Swiss franc, Pound sterling, Japanese yen, Czech koruna, Danish krone, Norwegian krone, Swedish krona and International Monetary Fund unit compared to Polish zloty. In the case of the Japanese yen and Hungarian forint, 100 units of these currencies are considered. Otherwise, 1 unit of the currency is analysed. The exchange rate data was retrieved from the National Polish Bank NBP archive [22].

2. Hölder sequences

The Hölder functions are one of the key construction elements of FRAMA models [12, 13, 19]. In this work, we use Hölder functions to model the deterministic trends of the irregular series of empirical data directly. An unusual similarity of the plots of some bi-Hölder functions (e.g. Weierstrass function) to the stock quotes is the premise for our approach [20]. We follow one of the rules of the book author [21]:

"Some models in economy and other subjects violate a basic rule: if the model does not work, then it should not be developed, but its foundation needs to be changed. In each case, the prediction boundaries of the given system must be defined first."

The function $f:[0,\infty)\to\mathbb{R}$ is called a bi-Hölder function with the exponent γ in the range $[0,T]$, if following criteria are met:

a) there exists $b>0$, such that

$$|f(t)-f(s)|\le b|t-s|^{\gamma} \text{ for } s,t\in[0,T].$$

b) there exists $a,\delta_0>0$, such that for each $\delta\in(0,\delta_0)$ and for each $t\in[0,T]$ there is $s\in[0,T]$ meeting the condition

$$0<|t-s|\le\delta \text{ and } |f(t)-f(s)|\ge a|t-s|^{\gamma}.$$

Example [20]. For each $\gamma\in(0,1)$ and sufficiently large $\lambda>1$ Weierstrass function given by

$$\sum_{k=1}^{\infty}\lambda^{(\gamma-2)k}\sin\left(\lambda^{k}t\right) \text{ for } t\ge 0$$

is a bi-Hölder function with the exponent γ in range $[0,1]$.

If $f:[0,\infty)\to\mathbb{R}$ is bi - Hölder function with exponent γ in range $[0,T]$ then [20]:

$$\dim_B \Gamma(f)=2-\gamma,$$

where

$$\Gamma(f)=\{(t,f(t)):\ t\in[0,T]\}.$$

It implies that determining the box-dimension of the function f plot, we simultaneously specify the exponent γ, and that by determining the exponent γ we simultaneously specify the box-dimension of the function f .

An irregular sequence of empirical data might, but does not have to, be a distorted sequence of the bi-Hölder function values.

A sequence $(x_t)_{t=1}^{\infty}$ is called a Hölder sequence, if there exist constants $b>0$, $\gamma\in(0,1)$ and sequences of positive numbers $(\varepsilon_t^-)_{t=1}^{\infty}$, $(\varepsilon_t^+)_{t=1}^{\infty}>0$, such that for each $k\in\mathbb{N}$:

$$bk^{\gamma}+\varepsilon_{t+k}^{-}\le|x_{t+k}-x_t|\le bk^{\gamma}+\varepsilon_{t+k}^{+},\ t\in\mathbb{N},$$

$$\lim_{n\to\infty}\mu(\varepsilon_{t+k}^{-})_{t=1}^{n}=\lim_{n\to\infty}\mu(\varepsilon_{t+k}^{+})_{t=1}^{n}=0,$$

where μ is the mean of the sequence.

Then for each $k\in\mathbb{N}$ we have:

$$bk^{\gamma}=\lim_{n\to\infty}\mu(bk^{\gamma}+\varepsilon_{t+k}^{-})_{t=1}^{n}\le\lim_{n\to\infty}\mu(|x_{t+k}-x_t|)_{t=1}^{n}\le\lim_{n\to\infty}\mu(bk^{\gamma}+\varepsilon_{t+k}^{+})_{t=1}^{n}=bk^{\gamma},$$

Therefore

$$\lim_{n\to\infty}\mu(|x_{t+k}-x_t|)_{t=1}^{n}=bk^{\gamma}, \tag{2}$$

where $\gamma\in(0,1)$ is a Hölder exponent.

3. Procedures for designating a Hölder exponent and fractal dimension

Procedures presented in this chapter are the modifications of the procedures described by K. Falconer [20]. The first procedure is a widely known method based on counting the number of "boxes" covering the analysed plot [4,21]. In our case it is the plot of the daily currency exchange values $(x_t)_{t=1}^{N}$ collected during one year in the 2000-2015 period, $N\in[251,256]$ depending on the analysis period or $N=4045$ for the 2000-2015 analysis period.

Procedure I:

Step 1

Let $k_{\min}=2$, $k_{\max}=21$.

For each $k=k_{\min},\mathrm{k}_{\min}+1,\mathrm{k}_{\min}+2,\ldots,k_{\max}$ we designate:

- $n_k = \left[\frac{N-1}{k}\right]$ (the integer part of the number of $\frac{N-1}{k}$),
- the ends of the ranges

$t_{k,j} = 1 + jk$, $j = 0,1,\dots,n_k$ and

$t_{k,n_{k+1}} = N$, when $t_{k,n_k} < N$,

- the extreme values and the range of the sequence $(x_t)_{t=1}^N$:

$\mu_{k,j}^+ = \max_{t\in[t_{k,j-1},t_{k,j}]} x_t$, $\mu_{k,j}^- = \min_{t\in[t_{k,j-1},t_{k,j}]} x_t$, $\rho_{k,j} = \mu_{k,j}^+ - \mu_{k,j}^-$ for $j = 1,2,\dots,n_k$,

$\mu_{k,n_{k+1}}^+ = \max_{t\in[t_{k,n_k},N]} x_t$, $\mu_{k,n_{k+1}}^- = \min_{t\in[t_{k,n_k},N]} x_t$, $\rho_{k,n_{k=1}} = \mu_{k,n_{k+1}}^+ - \mu_{k,n_{k+1}}^-$ when $t_{k,n_k} < N$

,

- surface filled by rectangles $[t_{k,j-1}, t_{k,j}] \times [\mu_{k,j}^-, \mu_{k,j}^+]$ covering the plot of the sequence $(x_t)_{t=1}^N$

$P_k = k\sum_{j=1}^{n_k} \rho_{k,j}$ or $P_k = k\sum_{j=1}^{n_k} \rho_{k,j} + (N - t_{k,n_k})\rho_{k,n_{k+1}}$ when $t_{k,n_k} < N$.

Step 2

The parameters of the linear model

$$\ln P_k = \beta + \gamma \ln k + \varepsilon_k,\ k = k_{\min},\ k_{\min}+1,\ k_{\min}+2,\dots,k_{\max},$$

are estimated with Least Square Method. The determinant coefficient R^2 is calculated.

Step 3

If $R^2 \geq 0{,}95$, then we assume that $(x_t)_{t=1}^N$ is a Hölder sequence with $b = e^\beta$ parameter, a Hölder exponent γ and a fractal dimension given by formula (1).

If $R^2 < 0{,}95$ then we scrub further research.

Procedure II:

The property (2) justifies the following procedure for parameters b, γ estimation for irregular sequences of empirical data.

Step 1

Let $k_{\max} = 20$. For each $k = 1, 2, \dots, k_{\max}$ we designate

$$\rho_k = \mu(|x_{t+k} - x_t|)_{t=1}^n.$$

Step 2

The parameters of the linear model

$$\ln \rho_k = \beta + \gamma \ln k + \varepsilon_k,\ k = 1, 2, \ldots, k_{\max},$$

are estimated with Least Square Method. The determinant coefficient R^2 is calculated.

Step 3

If $R^2 \geq 0.95$, then we assume that $(x_t)_{t=1}^{N}$ is a Hölder sequence with $b = e^{\beta}$ and γ parameters and fractal dimension given by formula (1).

If $R^2 < 0.95$ then we scrub the further research.

4. The currency exchange modelling procedure

Step 1

We assume that the model of currency exchange takes the following form:

$$x_t = \alpha_0 + \alpha_1 t + \alpha_2 t^{\gamma} + \varepsilon_t,\ t = 1,2,\ldots,N \tag{3}$$

where $N \in [251, 256]$ or $N = 4045$ depending on the study period. We carry out the calculations for:

a) each year in the 2000-2015 period and
b) full range of the data 2000-2015.

The parameters of the model (3) α_0, α_1, α_2 are estimated with the use of the Least Squares Method. The exponent γ is the Hölder exponent estimated in procedures I and II, ε_t, $t = 1,2,\ldots,N$ is the sequence of the residuals of model (3).

Step 2

We designate the standard deviation σ of the sequences of residuals ε_t, $t = 1,2,\ldots,N$, where $N \in [251, 256]$ or $N = 4045$ in the period of analysis in the case of a) and b).

Step 3

The following measures of quality of models are introduced:

- the number l is the percentage share of the currency exchange rate falling into $[-3\sigma, 3\sigma]$ range in the estimation period,
- the number $l_{1/2}$ is the percentage share of the currency exchange rate falling into $[-3\sigma, 3\sigma]$ range in the half-year period after estimation,
- the number l_1 is the percentage share of the currency exchange rate falling into $[-3\sigma, 3\sigma]$ range in one year period after estimation.

5. Results

The value of the determination coefficient meets the required criterion ($R^2 \geq 0.95$) regardless the applied procedure (I or II) for each currency and subperiod with one exception: the fractal dimension calculated according to procedure II for CHF currency based on the data from 2015, $R^2 = 0.901$. Having had excluded this exception, the model (3) was chosen, which, according to the procedure described in Section 3, showed that the model quality indicator (l number) obtained through both procedures I and II falls within the range [98.4%, 100%] for all analysed annual periods. In the case of Swiss franc in 2015 the l number is 94.1% and 95.3% for procedures I and II respectively. A percentage share of the CHF contained in the range $[-3\sigma, 3\sigma]$ is larger for procedure II than for procedure I, despite having a lower value $R^2 = 0.901$ that did not meet the criterion ($R^2 \geq 0.95$).

Tab. 1. The fractal dimension $dim(x_t)_{t=1}^{n}$, standard deviation σ of residuals of models (3), the percentage contribution of the currency exchange rates in range $\pm 3\sigma$ in half-year $l_{1/2}$ and annual l_1 period following the estimation obtained in procedure I. Shaded cells in both tables correspond to the values of $l_{1/2}$ and l_1 which are less than 50%

		2001	2002	2003	2004	2005	2006	2007	2008	2009	2010	2011	2012	2013	2014	2015
USD	dim	1.42	1.34	1.36	1.36	1.37	1.34	1.32	1.34	1.39	1.40	1.37	1.34	1.34	1.37	1.34
	σ	0.10	0.08	0.09	0.07	0.09	0.07	0.06	0.15	0.15	0.15	0.09	0.12	0.05	0.04	0.08
	$l_{1/2}$[%]	100	100	100	30.2	99.2	100	100	64.6	18.9	100	13.5	100	68.3	37.8	81.0
	l_1[%]	93.2	73.5	76.2	15.1	92.9	93.3	61.4	32.2	9.4	66.3	6.7	100	34.1	20.1	61.9
AUD	dim	1.37	1.42	1.31	1.31	1.39	1.38	1.29	1.37	1.36	1.43	1.36	1.33	1.35	1.38	1.37
	σ	0.07	0.04	0.05	0.07	0.05	0.03	0.05	0.06	0.06	0.06	0.05	0.09	0.07	0.04	0.08
	$l_{1/2}$[%]	100	29.4	66.4	42.1	100	74.6	100	0.0	63.8	97.6	23.0	89.6	46.0	96.9	98.4
	l_1[%]	92.4	14.6	33.2	21.0	69	55.6	91.7	0.0	31.8	89.7	11.5	45.4	23.0	78.3	75.8
CAD	dim	1.41	1.35	1.34	1.39	1.38	1.36	1.33	1.37	1.38	1.39	1.34	1.37	1.38	1.41	1.36
	σ	0.07	0.05	0.06	0.06	0.06	0.06	0.07	0.08	0.09	0.12	0.07	0.09	0.05	0.03	0.06
	$l_{1/2}$[%]	100	32.5	72.7	64.3	65.9	75.4	33.1	74.8	26.8	100	17.5	100	85.7	22.0	75.4
	l_1[%]	100	16.2	36.3	32.1	33.7	37.7	38.6	45.9	13.3	53.2	8.7	97.2	42.9	11.0	57.1
EUR	dim	1.37	1.40	1.35	1.34	1.38	1.38	1.37	1.35	1.40	1.46	1.36	1.32	1.40	1.36	1.33
	σ	0.13	0.11	0.06	0.05	0.07	0.06	0.04	0.14	0.13	0.08	0.08	0.08	0.05	0.03	0.04
	$l_{1/2}$[%]	100	100	83.6	41.3	66.7	100	100	68.5	72.4	100	8.7	94.4	100	33.9	42.9
	l_1[%]	100	100	41.8	20.6	33.3	71.4	68.1	40.0	36.1	69.0	4.4	94.4	82.9	46.1	21.4
HUF	dim	1.42	1.42	1.37	1.36	1.33	1.35	1.34	1.37	1.37	1.38	1.37	1.39	1.38	1.36	1.42
	σ	0.05	0.03	0.04	0.03	0.03	0.02	0.01	0.03	0.03	0.02	0.02	0.02	0.02	0.01	0.01
	$l_{1/2}$[%]	100	85.7	99.2	42.1	87.3	93.7	75.6	99.2	100	66.7	86.5	68.0	100	56.7	78.6
	l_1[%]	100	43.5	87.5	21.0	58.3	74.6	37.8	62.4	100	63.9	43.3	84.1	100	28.3	89.3
CHF	dim	1.35	1.38	1.39	1.37	1.38	1.40	1.37	1.35	1.40	1.42	1.36	1.33	1.42	1.35	1.31
	σ	0.09	0.08	0.05	0.04	0.05	0.04	0.04	0.12	0.10	0.09	0.11	0.07	0.04	0.03	0.10
	$l_{1/2}$[%]	88.8	100	100	41.3	73.8	100	85.8	77.2	66.9	100	16.7	99.2	100	6.3	100
	l_1[%]	73.7	100	58.6	20.6	36.9	87.3	63.8	43.9	33.3	90.1	8.3	99.6	76.6	3.1	99.2
GBP	dim	1.38	1.36	1.34	1.33	1.41	1.41	1.27	1.38	1.37	1.40	1.36	1.34	1.38	1.40	1.35
	σ	0.18	0.16	0.12	0.08	0.12	0.09	0.10	0.14	0.17	0.18	0.12	0.14	0.07	0.05	0.10
	$l_{1/2}$[%]	100	95.2	84.4	13.5	73.0	100	66.1	78.7	60.6	100	13.5	100	100	46.5	23.0
	l_1[%]	100	97.6	42.2	6.7	36.5	80.6	55.9	54.5	30.2	83.3	6.7	100	100	46.1	11.5

JPY	dim	1.36	1.39	1.36	1.36	1.35	1.39	1.37	1.35	1.41	1.43	1.37	1.30	1.41	1.32	1.34
	σ	0.12	0.11	0.09	0.06	0.08	0.04	0.06	0.23	0.17	0.16	0.12	0.21	0.08	0.06	0.06
	$l_{1/2}[\%]$	97.6	100	68.8	40.5	74.6	91.3	100	65.4	68.5	100	12.7	75.2	100	31.5	56.3
	$l_1[\%]$	98.8	71.9	34.4	20.2	37.3	52.0	70.5	32.5	34.1	72.6	6.3	78.5	73.0	15.7	49.2
CZK	dim	1.38	1.36	1.36	1.36	1.41	1.33	1.37	1.37	1.40	1.47	1.37	1.32	1.35	1.38	1.37
	σ	0.003	0.005	0.003	0.002	0.002	0.002	0.002	0.004	0.003	0.002	0.003	0.002	0.003	0.001	0.002
	$l_{1/2}[\%]$	98.4	100	100	38.1	48.4	100	94.5	81.9	69.3	100	11.1	89.6	100	66.9	49.2
	$l_1[\%]$	90.8	84	64.5	19.0	24.2	61.9	71.3	63.1	34.5	75.0	5.6	83.7	65.5	70.1	24.6
DKK	dim	1.36	1.40	1.35	1.35	1.38	1.38	1.37	1.35	1.40	1.46	1.36	1.32	1.41	1.36	1.33
	σ	0.02	0.02	0.01	0.01	0.01	0.01	0.01	0.02	0.02	0.01	0.01	0.01	0.01	0.00	0.01
	$l_{1/2}[\%]$	100	100	83.6	41.3	65.9	100	100	69.3	73.2	100	8.7	93.6	100	26.8	46.8
	$l_1[\%]$	100	100	41.8	20.6	32.9	70.6	67.3	40.4	36.5	69.0	4.4	93.2	79.0	18.9	23.4
NOK	dim	1.38	1.33	1.43	1.38	1.38	1.40	1.35	1.40	1.31	1.43	1.36	1.35	1.41	1.32	1.38
	σ	0.01	0.02	0.01	0.01	0.01	0.01	0.01	0.01	0.02	0.01	0.01	0.01	0.01	0.01	0.01
	$l_{1/2}[\%]$	100	92.9	87.5	50.0	81.0	23.0	100	7.9	68.5	100	11.1	100	29.4	96.9	48.4
	$l_1[\%]$	93.6	66.8	43.8	25.0	73.8	11.5	89.0	3.9	34.1	56.7	5.6	57.0	14.7	75.6	24.2
SEK	dim	1.36	1.39	1.38	1.37	1.41	1.38	1.38	1.38	1.37	1.39	1.38	1.39	1.43	1.34	1.39
	σ	0.01	0.01	0.01	0.01	0.01	0.01	0.01	0.01	0.01	0.01	0.01	0.01	0.01	0.01	0.01
	$l_{1/2}[\%]$	100	100	74.2	60.3	39.7	100	100	20.5	66.9	100	17.5	100	40.5	87.4	72.2
	$l_1[\%]$	98.4	98.8	37.1	31.0	19.8	98.4	76.0	60.4	33.3	85.3	8.7	89.2	22.2	85.0	36.1
XDR	dim	1.45	1.44	1.40	1.34	1.40	1.37	1.30	1.34	1.39	1.39	1.36	1.32	1.39	1.38	1.41
	σ	0.15	0.12	0.09	0.07	0.10	0.08	0.07	0.20	0.19	0.16	0.11	0.15	0.06	0.04	0.07
	$l_{1/2}[\%]$	100	100	93.0	28.6	95.2	100	100	70.1	58.3	100	11.9	100	97	62.2	62.7
	$l_1[\%]$	99	92.9	46.5	14.3	90.5	90.1	67.3	34.9	29.0	68.3	6.0	100	49.2	36.6	32.5

Source: own work

Tab. 2. The fractal dimension $dim(x_t)_{t=1}^{n}$, standard deviation σ of residuals of models (3), the percentage contribution of the currency exchange rates in range $\pm 3\sigma$ in half-year $l_{1/2}$ and annual l_1 period following the estimation obtained in procedure II. Shaded cells in both tables correspond to the values of $l_{1/2}$ and l_1 which are less than 50%

		2001	2002	2003	2004	2005	2006	2007	2008	2009	2010	2011	2012	2013	2014	2015
USD	dim	1.62	1.54	1.45	1.48	1.49	1.46	1.42	1.46	1.56	1.50	1.53	1.49	1.49	1.52	1.54
	σ	0.10	0.08	0.09	0.07	0.09	0.07	0.06	0.16	0.15	0.15	0.09	0.12	0.05	0.04	0.08
	$l_{1/2}[\%]$	100	100	100	38.1	94.4	100	100	69.3	18.9	100	15.1	100	73.0	48.8	88.1
	$l_1[\%]$	91.2	81.0	75.4	19.0	86.5	96.4	61.8	34.5	9.4	67.5	7.5	100	36.5	27.6	65.9
AUD	dim	1.50	1.65	1.46	1.39	1.56	1.60	1.47	1.52	1.49	1.58	1.54	1.46	1.44	1.52	1.51
	σ	0.07	0.04	0.05	0.07	0.05	0.03	0.05	0.06	0.06	0.06	0.05	0.09	0.07	0.05	0.08
	$l_{1/2}[\%]$	100	30.2	66.4	41.3	100	81.0	100	0.0	63.8	96.8	26.2	88.8	46.0	96.9	97.6
	$l_1[\%]$	95.6	15.0	33.2	20.6	100	61.9	96.1	0.0	31.8	89.7	13.1	45.0	23.0	74.4	72.2
CAD	dim	1.59	1.51	1.43	1.54	1.52	1.46	1.50	1.51	1.51	1.47	1.48	1.54	1.55	1.65	1.52
	σ	0.07	0.05	0.06	0.06	0.06	0.06	0.07	0.09	0.09	0.12	0.07	0.09	0.05	0.03	0.06
	$l_{1/2}[\%]$	100	33.3	71.9	65.9	64.3	75.4	30.7	72.4	26.0	100	21.4	100	91.3	23.6	73.8
	$l_1[\%]$	100	16.6	35.9	32.9	32.1	37.7	34.3	52.9	12.9	59.9	10.7	89.2	45.6	11.8	56.0
EUR	dim	1.47	1.54	1.52	1.44	1.47	1.46	1.48	1.48	1.58	1.63	1.50	1.46	1.53	1.53	1.45
	σ	0.13	0.11	0.06	0.05	0.08	0.06	0.04	0.15	0.13	0.08	0.08	0.08	0.05	0.03	0.04

	$l_{1/2}$[%]	100	100	82.8	41.3	69.8	100	100	63.8	73.2	100	9.5	95.2	100.0	36.2	47.6
	l_1[%]	100	100	41.4	20.6	34.9	84.1	67.7	41.2	36.5	69.0	4.8	95.2	93.3	56.7	23.8
HUF	dim	1.53	1.58	1.56	1.48	1.42	1.50	1.46	1.50	1.51	1.61	1.50	1.55	1.50	1.51	1.66
	σ	0.05	0.03	0.04	0.03	0.03	0.02	0.01	0.03	0.03	0.02	0.02	0.02	0.03	0.01	0.01
	$l_{1/2}$[%]	100	85.7	96.1	42.9	96.0	82.5	75.6	99.2	100	51.6	92.1	64.8	100	59.1	77.0
	l_1[%]	100	43.1	87.9	21.4	64.7	71.8	37.8	73.7	99.6	49.2	47.6	81.7	100	34.6	88.5
CHF	dim	1.44	1.55	1.60	1.49	1.50	1.50	1.47	1.52	1.58	1.52	1.60	1.46	1.60	1.51	1.55
	σ	0.09	0.08	0.05	0.04	0.05	0.05	0.04	0.13	0.10	0.09	0.11	0.07	0.04	0.03	0.10
	$l_{1/2}$[%]	94.4	100	100	42.9	73.8	100	85.8	75.6	66.9	100	16.7	99.2	100	6.3	100
	l_1[%]	78.1	100	62.1	21.4	36.9	97.6	63.8	45.5	33.3	91.3	8.3	99.6	85.3	3.1	97.2
GBP	dim	1.55	1.54	1.49	1.42	1.55	1.54	1.41	1.55	1.50	1.49	1.55	1.49	1.52	1.60	1.53
	σ	0.17	0.16	0.12	0.08	0.12	0.09	0.10	0.15	0.17	0.18	0.12	0.14	0.07	0.05	0.10
	$l_{1/2}$[%]	100	89.7	84.4	14.3	73.8	100	54.3	69.3	61.4	100	15.9	100	100	44.9	23.0
	l_1[%]	100	94.9	43.0	7.1	36.9	78.6	47.6	60.0	30.6	86.5	7.9	100	100	44.9	11.5
JPY	dim	1.51	1.50	1.47	1.45	1.50	1.51	1.47	1.47	1.66	1.56	1.52	1.44	1.54	1.48	1.56
	σ	0.12	0.11	0.10	0.06	0.08	0.05	0.06	0.24	0.17	0.16	0.13	0.22	0.08	0.06	0.06
	$l_{1/2}$[%]	96.8	100	69.5	40.5	88.9	96.0	100	72.4	67.7	100	12.7	68.8	100	42.5	42.9
	l_1[%]	98.4	76.3	34.8	20.2	51.2	55.2	71.3	36.1	33.7	80.2	6.3	62.5	77.4	21.3	31.7
CZK	dim	1.53	1.47	1.51	1.52	1.51	1.45	1.47	1.52	1.54	1.70	1.50	1.47	1.45	1.59	1.51
	σ	0.003	0.005	0.003	0.002	0.002	0.002	0.002	0.004	0.003	0.002	0.003	0.002	0.003	0.001	0.002
	$l_{1/2}$[%]	98.4	100	100	38.9	54.0	100	96.9	76.4	71.7	100	11.1	90.4	100	67.7	52.4
	l_1[%]	93.6	100	62.1	19.4	27.0	65.5	72.4	68.6	35.7	81.0	5.6	85.3	69.4	57.9	26.2
DKK	dim	1.47	1.54	1.52	1.44	1.47	1.46	1.48	1.48	1.58	1.63	1.50	1.45	1.54	1.53	1.45
	σ	0.02	0.02	0.01	0.01	0.01	0.01	0.01	0.02	0.02	0.01	0.01	0.01	0.01	0.00	0.01
	$l_{1/2}$[%]	100	100	83.6	41.3	69.8	100	100	63.8	73.2	100	9.5	93.6	100	27.6	52.4
	l_1[%]	100	100	41.8	20.6	34.9	84.5	68.5	41.2	36.5	69.0	4.8	93.2	85.7	29.1	26.2
NOK	dim	1.52	1.46	1.64	1.49	1.50	1.54	1.44	1.56	1.48	1.56	1.50	1.54	1.53	1.48	1.58
	σ	0.01	0.02	0.01	0.01	0.01	0.01	0.01	0.01	0.02	0.01	0.01	0.01	0.01	0.01	0.01
	$l_{1/2}$[%]	100	88.1	90.6	54.0	87.3	27.8	100	7.9	68.5	100	11.1	99.2	30.2	99.2	48.4
	l_1[%]	88.0	51.4	45.3	27.0	89.3	13.9	87.0	3.9	34.1	58.7	5.6	54.2	15.1	91.3	24.2
SEK	dim	1.50	1.54	1.51	1.47	1.53	1.48	1.56	1.56	1.51	1.54	1.48	1.56	1.58	1.50	1.49
	σ	0.01	0.01	0.01	0.01	0.01	0.01	0.01	0.01	0.01	0.01	0.01	0.01	0.01	0.01	0.01
	$l_{1/2}$[%]	99.2	100	75.0	61.1	40.5	100	99.2	13.4	66.9	100	20.6	100	64.3	89.8	79.4
	l_1[%]	95.2	99.6	37.5	31.3	20.2	93.3	76.0	56.1	33.3	90.1	10.3	86.9	37.3	82.3	39.7
XDR	dim	1.61	1.60	1.56	1.44	1.53	1.47	1.41	1.46	1.56	1.51	1.50	1.46	1.52	1.56	1.61
	σ	0.15	0.12	0.09	0.07	0.10	0.08	0.07	0.21	0.18	0.16	0.12	0.15	0.07	0.04	0.07
	$l_{1/2}$[%]	100	100	93.0	34.1	98.4	100	100	78.7	56.7	100	13.5	100	100	68.5	73.0
	l_1[%]	100	99.6	46.5	17.1	99.2	92.9	67.7	39.2	28.2	69.0	6.7	100	54.4	57.9	39.7

Source: own work

The results obtained for each considered currency based on the exchange rate data for years in the period 2001-2015 are shown in tables 1 and 2. There are: fractal dimension values, standard deviation values of residuals of models, σ, the percentage contribution of the currency exchange rates in range $[-3\sigma,3\sigma]$ in half-year $l_{1/2}$ and annual l_1 period following the estimation. Tables 1 and 2 show the results obtained on the basis of procedures I and II respectively.

Shaded cells in both tables correspond to the values of $l_{1/2}$ and l_1 which are less than 50%. Comparing the shaded areas in both tables we notice that they follow a similar pattern. Moreover, the number of shaded cells is identical in both cases. It might indicate that, although the fractal dimension values calculated according to procedure I are lower than the corresponding values calculated using procedure II, the different procedures of determining the fractal dimension yield models having similar quality indicators for every considered currency and time period.

Figure 1 presents a comparison between an average fractal dimension for all analysed currencies determined on the basis of a one-year observation period and fractal dimension values based on the full data range 2001-2015. The condition $R^2 \geq 0.99$ is met for the full data range for all analysed currencies independently of the procedure.

Figure 1 confirms the results involving the fractal dimension presented in tables 1 and 2. We may find that the fractal dimension obtained using both procedures are significantly different. However, the mean fractal dimension values determined for the consecutive years of the 2001-2015 period and the fractal dimension values calculated for the entire period using the same method are very similar.

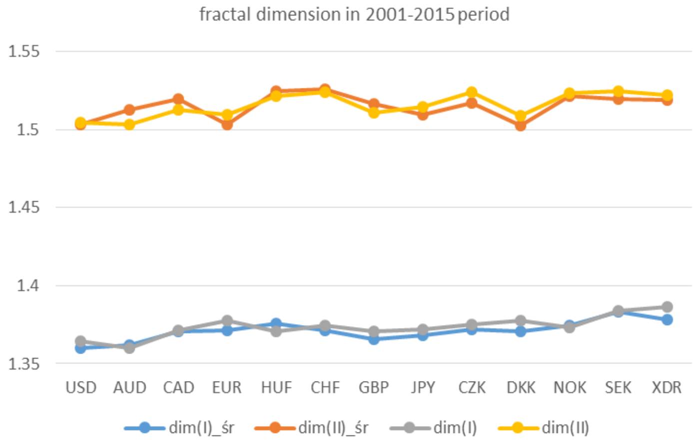

Fig. 1. An average fractal dimension for all analysed currencies determined on the basis of a one-year observation period and fractal dimension values based on the full data range 2001-2015. dim(I)_śr - An average fractal dimension value determined on the basis of a one-year observation period in procedure I, dim(II)_śr - An average fractal dimension value determined on the basis of a one-year observation period in procedure II, dim(I) - A fractal dimension value determined on the basis of full data range in procedure I, dim(II) - A fractal dimension value determined on the basis of full data range in procedure II (Source: own work)

The value of the fractal dimension of the currency exchange rate can be used to analyse trends of the investigated currency. Based on the plot shown in figure 1 we may find that the exchange rates of all currencies behave similarly. The fractal dimension determined for all considered currencies according to the same procedure remains almost at constant level. This demonstrates that all considered currencies have similar fluctuation levels. The dimension values for all analysed currencies fall within the range (1.36;1.39) for procedure I and within (1.50;1.53) for procedure II.

Figure 2 shows the exchange rates of the selected currencies: USD (figure 2a), EUR (figure 2b), CHF (figure 2c) and GBP (figure 2d) (black line) along with the theoretical values calculated from model (3), $\hat{x}_t$, over the 2001-2016 period. The red solid line corresponds to the results obtained from procedure I. The green dotted line corresponds to the results obtained from procedure II. Additionally, a range $\langle \hat{x}_t - 3\sigma, \hat{x}_t + 3\sigma \rangle$ is shown in the figure, the blue solid line denoting procedure I results and the purple dotted line – procedure II results. The model was based on the data from 2001-2015. Using the plots presented in figure 2, it can be stated that the results from both procedures I and II yield the models described by the functions following almost identical plots. Furthermore, currency exchange rates in 2016 fit into the predicted interval for each presented case. In this situation, the model quality indicator for the one-year forecast equals 100%.

a)

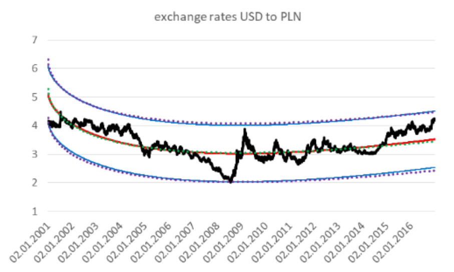

b)

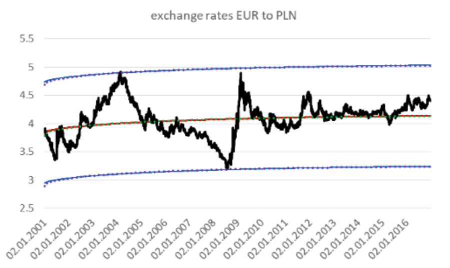

c)

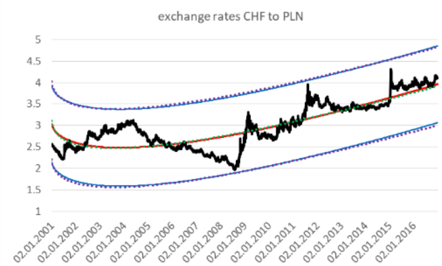

d)

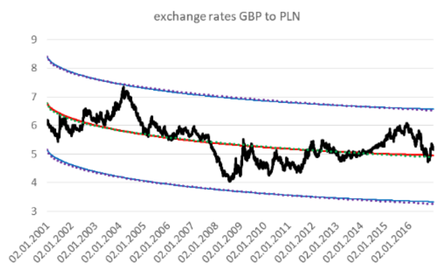

Fig. 2. The exchange rates of the selected currencies such as USD (Fig. 2a), EUR (Fig. 2b), CHF (Fig. 2c) and GBP (Fig .2d) in the 2001-2016 period (Source: own work)

Similarly to figure 2, figure 3 shows the exchange rates of USD in 2001-2016 period. However, the presented models given by the equation (3) and obtained using procedure I were only estimated on the basis of the annual observation along with a one-year forecast period. Similarly, a $\langle \hat{x}_t - 3\sigma, \hat{x}_t + 3\sigma \rangle$ range is shown. The blue line indicates periods when $l_{1/2} > 50\%$ and the red line indicated periods when $l_{1/2} \le 50\%$, see table 1.

Based on the charts in figure 3, we conclude that the proposed form of the model accurately reflects the exchange rate of the analysed currency in the estimation period. Note that the one-year models with prediction did not work with similar efficiency. The selected model quality indicator does not always correctly describe trend maintenance for all currencies and years. An example is the model obtained for USD from the data from 2008.

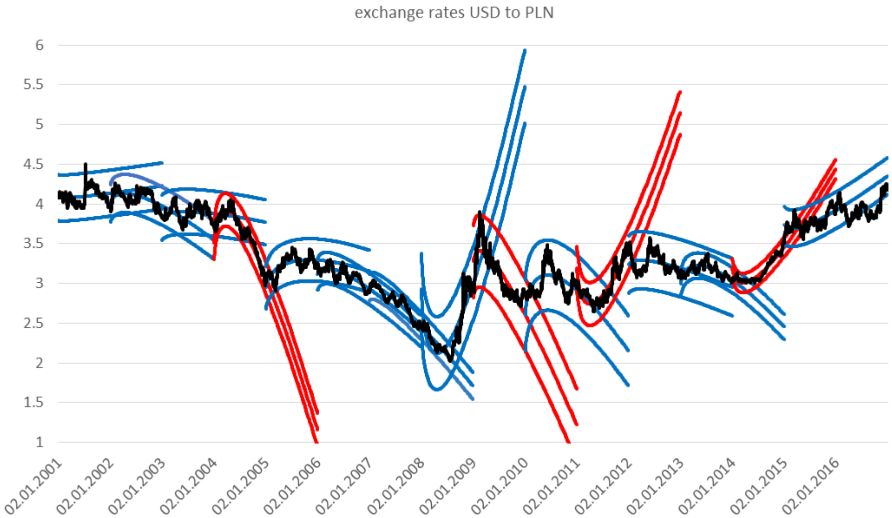

Fig. 3. The exchange rates of USD in 2001-2016 period with its theoretical value and a range $\langle \hat{x}_t - 3\sigma, \hat{x}_t + 3\sigma \rangle$ determined in procedure I on the basis of the annual observation with a one-year forecast period (Source: own work)

6. Summary

In this work, the exchange rates of 13 currencies in the 2001-2016 period were analysed. The fractal dimensions of the financial time series of the foreign currencies in 2001-2015 period and one-year periods during 2001-2015 were calculated. The value of the fractal dimension for a given currency in a given period enables quantitative specification of the irregularities of the exchange rate in that period. The fluctuations of the exchange rates are similar for all considered currencies. Furthermore, the models defined by the use of the fractal dimension describing the behaviour of the given exchange rates were proposed. It turns out that the proposed form of the model reflects the actual currency exchange rate in the estimation period accurately, however, not always within the considered prediction period, especially when the lengths of the prediction and estimation periods are similar. In the case where the model construction time is significantly longer than the model verification time, the fractal analysis predicts the future course of the exchange rates of a given currency. It was observed that the model construction time, especially the length of the study period, is critical in forecasting.

In conclusion, the fractal dimension was applied in modelling the behaviour of the exchange rates, i.e. highly noisy data. The obtained results are very satisfactory, therefore the procedures presented in the paper might be used with different time-series data, not only from the financial domain.

References

[1] H.O. Peitgen, H. Jürgens and D. Saupe, "Chaos and Fractals New Frontiers of Science", *New York: Springer-Verlag*, 1992.

[2] B.B Mandelbrot, "How long is the coast of Britain? Statistical self-similarity and fractional dimension, " *Science*, vol *156*, pp. 636–638, 1967.

[3] M.R. Schroeder, "Fractals, Chaos, Power Laws: Minutes from an Infinite", *New York: Dover Publications Inc*., 2009.

[4] J. Kudrewicz, "Fraktale i chaos", *Warszawa: Wydawnictwo Naukowo-Techniczne*, 1993.

[5] R.F. Voss, "1/f noise and fractals in economic time series", in *Fractal geometry and computer graphics*, red. J.L. Encarnacao H.-O. Peithen, G. Sakas, G. Englert. New York: Springer, 1992.

[6] A. Fisher, L. Calvet and B.B. Mandelbrot, "The multifractality of the deutsh mark US dollar exchange rates", *Cowles foundation discussion paper,* no 1165*,* pp. 1–77, 1997.

[7] D. Lunga and T. Marwala, "Time Series Analysis Using Fractal Theory and Online Ensemble Classifiers", in A. Sattar, B. Kang (eds) *Advances in Artificial Intelligence*. AI 2006. *Lecture Notes in Computer Science*, vol. 4304. Berlin, Heidelberg: Springer, 2006.

[8] B.B. Mandelbrot, "Fractals and Scaling in Finanse, Discontinuity, Concentration, Risk", *Selecta Volume E. New York: Springer-Verlag*, 1997.

[9] J. Fillol, "Multifractality: Theory and Evidence an Application to the French Stock Market", *Economics Bulletin*, vol. *3*, no. 31, pp. 1–12, 2003.

[10] B.B. Mandelbrot and R. L. Hudson, "The (mis)behavior of markets, A fractal view of Financial Turbulence", *New York: Basic Books*, 2004.

[11] G. Przekota and D. Przekota, "Szacowanie wymiaru fraktalnego szeregów czasowych kursów walut metodą podziału pola", *Badania operacyjne,* no. 3–4, pp. 67-82, 2004.

[12] A. Mastalerz-Kodzis, "Zastosowanie funkcji Höldera w modelu FRAMA", *Studia Ekonomiczne,* Uniwersytet Ekonomiczny w Katowicach, No 159, pp. 73–81, 2013.

[13] J. Ehlers, "Fractal Adaptive Moving Average", *Technical Analysis of Stock & Commodities*, vol 23, 10, pp. 81–82, 2005.

[14] E.E. Peters, "Fractal Market Analysis: Applying Chaos Theory to Investment and Economics", *New York: John Wiley & Sons*, 1994.

[15] J. Moody and L. Wu, "Price Behavior and Hurst Exponents of Tick-By-Tick Interbank Foreign Exchange Rates", *Computational Intelligence for Financial Engineering, Proceedings of the IEEE/IAFE*, 1995.
[16] R. Szóstakowski, "The use of the Hurst exponent to investigate the quality of forecasting methods of ultra-high-frequency data of exchange rates", *Przegląd statystyczny*, TOM LXV, ZESZYT 2, 2018.
[17] P. Kroha and M. Škoula, "Hurst Exponent and Trading Signals Derived from Market Time Series", in *Proceedings of the 20th International Conference on Enterprise Information Systems (ICEIS)*, vol 1, 2018, pp. 371–378.
[18] H. Kowgier, "Kilka uwag o wymiarze fraktalnym Minkowskiego oraz wykładniku Hursta na giełdzie papierów wartościowych", *Studia i Prace Wydziału Nauk Ekonomicznych i Zarządzania*, no 15, 2009, pp. 157–167.
[19] M. Pietrzak, "Wykorzystanie funkcji Höldera w modelowaniu cen spółek na WGPW", *Acta Universitatis Lodziensis, Folia Oeconomica*, no 166, 2003, pp. 63–83.
[20] K.J. Falconer, "Fractal Geometry: Mathematical Foundations and Applications", *West Sussex: John Wiley & Sons Ltd.*, 2003.
[21] F. Morrison, "The art of modeling dynamic systems: forecasting for chaos, randomness and determinism", *2nd ed., New York: Dover Publication*, 2008.
[22] http://www.nbp.pl/home.aspx?f=/kursy/arch_a.html, 27.10.2016

Abdelkader Rouibah[1], Djamel Benazzouz[1] , Rahmani Kouider[2]

INFLUENCE OF PERFORMANCE PARAMETERS ON THE CHOICE OF TOWER SOLAR POWER PLANTS LOCATION: REAL CASE STUDY IN ALGERIA

Keywords: solar tower power plants STPP; DNI; SAM; SM;TES; performance

Abstract

The objective of this paper is the technological analysis of three future solar tower power plants (STPP), which are part of the Algerian energy programme and will be installed in the highlands and the Sahara. The increased production of solar systems is one of the best solutions to meet the needs of the electricity market and reduction of the greenhouse effect. The installation of a solar tower power plants consists of studying several factors of several degrees of freedom. The Direct Normal Irradiation, DNI, is the most important of these factors and its high value increases the performance of the solar power plant.

In this paper, we exploit the performance of the System Advisor Model, SAM, by various simulations based on real data obtained from the meteorological files of the studied sites. The choice of the solar field is a difficult task, as e.g. a choice of Solar Multiple, SM, between 1.4 and 1.6 is suitable for high optical performance with a lower surface of the field, and the starting arrangement must be very close to the optimum configuration, based on the experience obtained from the plants already in operation. The thermal energy storage capacity, TES, is insufficient for the whole night, it covers between 2 and 4 hours, hence it becomes necessary to use an auxiliary energy source. In addition, the interaction between the parameters and performance has led to selecting the optimal configuration of the Concentrated Solar Power, CSP.

1. Introduction

Algeria's commitment to renewable energy has brought global and sustainable solutions to the environmental challenges as well as the problem of preserving fossil energy resources.

Algeria’s highlighted its solar potential as one of the highest in the world (over 2 million km^2 of its territory receives annual daily average insolation of approx. 2,500 kWh/m2) [1, 2] by launching important projects in solar thermodynamics. The renewable energy programme involves the installation of renewable power stations capable of producing 22,000 MW by 2030 for the national market, i.e.

[1] M’Hamed Bougara University, Faculty of Engineering Sciences (FSI), Mechanics Laboratory of Systems and Solids, Boumerdès 35000, Algeria; rouibah_a@yahoo.fr; dbenazzouz@yahoo.fr

[2] Laboratoire de Recherche Modélisation Simulation et Optimisation des Systémes Complexese Réels equipe (SMEN) University of Djelfa, Algeria, kouiderrah1@gmail.com.

more than 37% of national electricity production – while maintaining the export option as a strategic objective, Fig.1 [3]. The world market for solar thermodynamics (CSP) is estimated at 14 GW in 2020 and 72 GW in the 2035 horizon, which constitutes a rapid strong growth compared to the 2012 capacity, amounting to 2.8 GW [4]. This strategic choice is motivated by the immense solar energy potential of "Sahara and High Plateau". This energy constitutes the major axis of the programme, which is devoted to solar thermal energy [5].

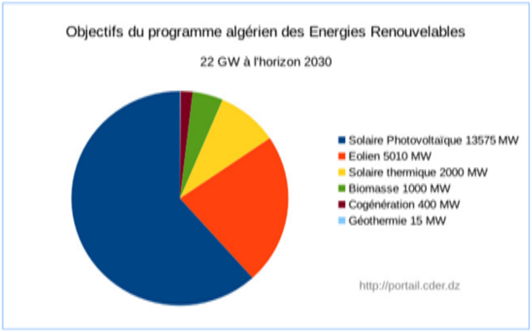

Fig. 1. The new national programme for the development of renewable energy (2015 - 2030) [6]

Solar power systems have a quasi - zero proportional cost: there is no fuel, only expenses (maintenance, guarding, repairs, etc..) which depend very little on the production. However, it incurs substantial investment costs, considerably higher compared to fossil techniques or other renewable energies [7.8].

Since solar energy is insufficiently dense, it is necessary to concentrate it, by means of reflecting mirrors, in order to obtain the operating temperatures enabling the production of electricity. Solar radiation can be concentrated on a linear or point receiver. The receiver absorbs the energy reflected by the mirror and transfers it into a thermodynamic heat transfer fluid [9.10].

The performance of the solar system is measured by its concentration factor. This coefficient evaluates the intensity of solar concentration. Whenever the concentration factor is high, the temperature reached will be high. Linear concentration systems generally have a lower concentration factor compared to point concentrators [11].

The body of literature in the field includes several studies into the feasibility of solar energy. S. Boudaoud et al. [12] carried out a technical and economic analysis of electricity costs and the economic feasibility of tower solar power plants in Algeria. O. Behar et al. [13] evaluated a wide range of clear sky solar radiation models, based on theoretical input parameters for the Algerian climate, in order to choose the best performance estimators of solar energy projects for which meteorological and radiometric measurement stations are not available. S. Mihoub et al. [14], proposed a methodology for optimal designing the configuration of the future Algerian solar tower power plant. The model is expected to minimise the electricity costs (LCOE) and the maximise the annual production of electricity. Given that the optimisation of the solar system performance is necessary for the investigation of future projects planned in Algeria, this paper applies the System Advisor Model (SAM) software to optimise the configuration of the CSP (Concentrated Solar Power). A numerical simulation under SAM, based on the DNI (real and satellite data), is carried out to find the best performance parameters in question (SM, PE, CF, TES ...). Finally, from the interaction of these parameters, the optimal configuration of the CSP is found.

2. Modelling of the central CSP

2.1. The general model of CSP

In a typical configuration, a heat - transfer fluid (salt molten) is heated in the receiver and used to power a conventional steam - turbine power cycle to generate electricity (see Figure3).

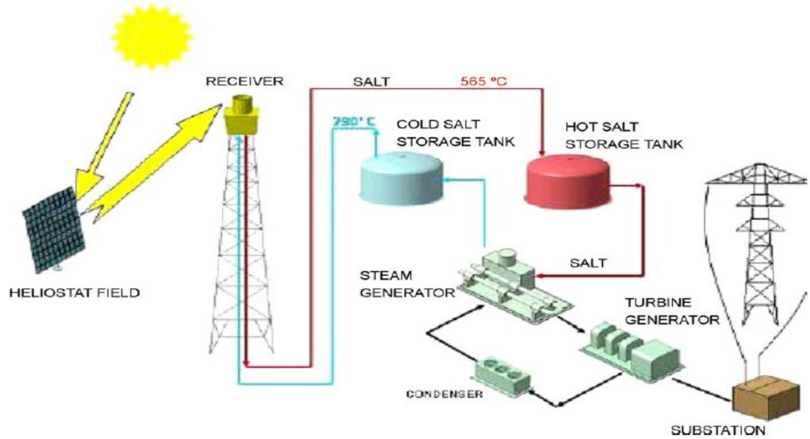

Fig. 2. Illustration of a solar tower power plant of a molten salt

2.2. Evaluation of solar radiation

The solar radiation intensity is an important factor in the evaluation of CSP plants. The direct normal irradiance (DNI) is the amount of direct normal solar radiation received per unit area. There are three techniques to assess the evolution of DNI over time for a given location [15,16]:

- real data
- satellite data.
- a combination of real and satellite data.

3. Modelling the Heliostats Field

3.1. Modelling geometric parameters

Optimisation of the design of the heliostats field is a trade - off between optical performance and cost, which is why this process includes both optical and economic analysis. This implantation can be performed by determining the optimum values of the radial spacing ΔR and the azimuth spacing ΔAZ.

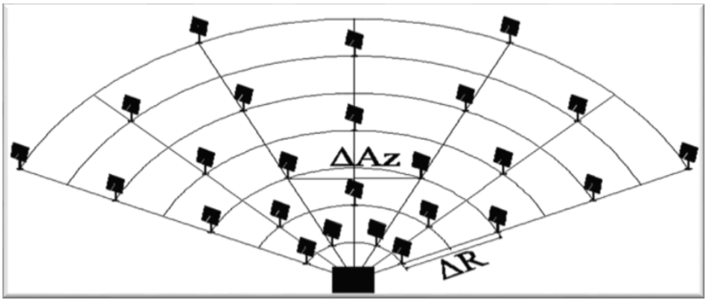

Fig. 3. Implementation of the heliostats field

There are various optimisation procedures to establish these two geometric position parameters. One of the most effective procedures is the radial offset arrangement, shown in Fig. 3. [17]. The evaluation of the radial and azimuthal distance can be evaluated by empirical equations 1 and 2. These parameters also depend on the angle (α) between the heliostat, the ground and the tower as shown in Fig.4 [18.19].

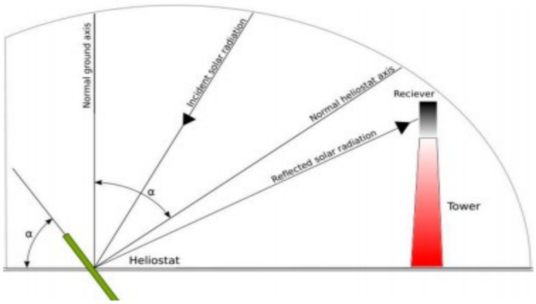

Fig. 4. Representation of the optical angle α

$$\Delta R/HM = 63.0093 - 0.587313\theta + 0.018423909\theta^2 + \cos\phi\,(2.808733 - 0.1480498\theta + 0.001489201\theta^2) \quad (1)$$

$$\Delta A_Z/WM = 2.46812 - 0.0401054\theta + 0.000923594\theta^2 + \cos\phi\,(0.17344593 - 0.009112590\theta + 0.000127610\theta^2) \quad (2)$$

ϕ: Heliostat azimuth angle, 0° is south. θ: Receiver elevation angle from heliostat in degrees.

3.2. Modelling energy parameters

The size of the heliostat field affects the optical performance and depends on the desired power and temperature of the heat transfer fluid at the output.

The total incident thermal energy is given by the following equation (3):

$$Q_h = I_d \times A_h \times N_h \quad (3)$$

such as:

I_d - the direct normal irradiation (DNI); A_h - the surface of the heliostat; N_h - the number of the heliostat.

The efficiency of the field η_h is defined from the following equation (4):

$$\eta_h = \frac{Q_{rec}}{Q_{inc}} = \frac{Q_{rec}}{I_d + A_h + N_h} \quad (4)$$

such as:

Q_{rec} - heat flow of the receiver, Q_{inc} - heat flow of the incident

The efficiency is obtained from the loss due to different factors (Cosine, shading, blocking, overflow, reflection, dispersion) and it is given by the following equation (5) [20].

$$\eta_h = \eta_{cos} \cdot \eta_{omb} \cdot \eta_{bloc} \cdot \eta_{deb} \cdot \eta_{ref} \cdot \eta_{disp} \quad (5)$$

such as:

η_{cos} - loss due to cosine effect; η_{omb} - loss due to shading effect; η_{bloc} - loss due to blocking effect; η_{deb} - loss due to overflow; η_{ref} - loss due to reflection; η_{disp} - loss due to dispersion:

4. Receiver Modelling

The receiver presented in the study is an external model consisting of vertically arranged pipes through which a heat transfer fluid is pumped in the vertical direction. Inside the pipe, three types of heat transfer occur (convection, conduction and radiation). The exchange with the outside is by means of radiation (solar and radiation loss), by convection (loss at the body of the receiver) and by conduction (loss through thermal bridges).

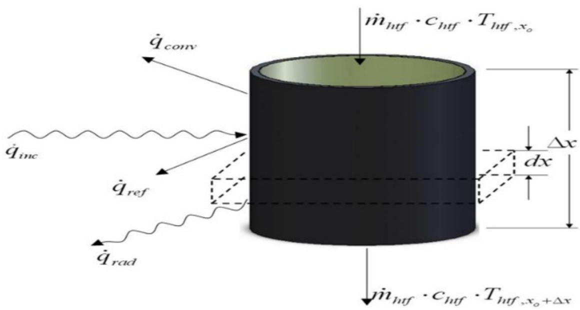

Fig.5. Energy balance of the external receiver [19]

Figure 5 groups together the different heat exchanges of the receiver with the external environment.
The heat flux of the receiver is expressed by (6):

$$Q_{rec} = q_{htf} + q_{conv} + q_{rad} + q_{ref} \tag{6}$$

with:

$$Q_{rec} = S_i . I_d \tag{7}$$

such as:
q_{htf} - heat flow of molten salt; q_{conv} - loss of convection heat flow; q_{rad} - loss of radiation heat flux; q_{ref} - loss of reflection flux; S_i - total surface.
The incidence of solar radiation I_d on the receiver is evaluated by the flux map radiation model.
The distribution of the radiation flux is integrated with (DELSOL 3 algorithm), based on direct radiation from 950 W/m^2 [15.21].

The energy absorbed by the heat transfer fluid (q_{htf}) is given by the following equation (8):

$$q_{htf} = m_{htf} . C_{htf}\left(T_{htf(x+dx)} - T_{htf(x)}\right) = US_i . (T_{st} - T_{htf}) \tag{8}$$

with:

$$US_i = \frac{1}{R_{cond} + R_{conv}} \tag{9}$$

$$R_{cond} = \frac{\ln\frac{D_{ot}}{D_{it}}}{2.\pi.L_t.K_t.N_t} \tag{10}$$

$$R_{cond} = \frac{2}{\pi.h_{htf}.L_t.D_t.N_t} \tag{11}$$

The loss by convection is given by equation (12):

$$q_{conv} = S_i . h_{conv} . (T_{st} - T_{ic-air}) \tag{12}$$

The radiation loss q_{rad} has a negligible value because the absorber shows a high absorption of short waves of solar radiation, the same as for loss by reflection q_{ref}, due to the lower emissivity of the long thermal waves.

5. Modelling Solar Power Plant performance

The performance of a well-configured solar tower system is based on several parameters, such as power generation injected to the grid, incident solar radiation and storage capacity. The capacity factor and the solar multiple are the most important factors characterising the performance of a central solar tower system.

5.1. Capacity Factor (CF)

The ratio of the energy generated by the system in partial time E_{gp} and the energy generated in full-time E_{gf} determines the capacity factor, and is given by equation (13), [22]

$$\mathrm{CF} = \frac{\mathrm{E_{gp}}}{365.24.\mathrm{E_{gf}}} \quad (13)$$

5.2. Solar Multiple SM

The ratio of energy to design point (thermal power produced by the field of heliostatsq_{sf} for different DNI values) and the thermal power required by the power block under nominal conditions q_{pb} determines the Solar Multiple (SM). It is expressed by equation (14) [22]:

$$\mathrm{SM} = \frac{q_{sf}}{q_{pb}} \quad (14)$$

For a system without a storage mode, SM=1

6. Model parameters and meteorological data

6.1. Model parameters

Tab. 1. Location parameters for different regions

Parameter	**Design parameters**	**Djelfa**	**El Oued**	**Béchar**
Location	DNI (W/M²))	1050	750	700
	Latitude (°)	34.68	33.50	31.50
	Longitude (°)	3.25	6.78	- 2.25
	Elevation (m)	1144	69	816

Tab. 2. Characteristics of the components of the solar tower system

Parameter	**Design parameters**	**Value**
Field of heliostats	Surface of the heliostat (m²)	144
Tower and Receiver	Diameter of pipes (mm) Thickness of pipes (mm) Type of pipe material (Stainless steel)	60 1 .25 AISI316
Fluid **Coolant**	HTF type (molten salt) Input Temperature (°C) Output Temperature (°C)	60% $NaNO_3$,40% KNO_3 565 290
Power Block	Design turbine output (MWe) Thermodynamic cycle efficiency (%) Operating pressure of the boiler (bar) Type of cooling capacitor	20 37 100 Air
Energy storage	Type of storage Load storage in full hours	Two tanks 0-12h

6.2. Meteorological data

In this work, the data for calculations were derived from the annual meteorological database, known as the reference year test (TRY) or typical meteorological year (TMY). It consists of measured values which are statistically selected from the annual individual values measured over a long period.

The file formats used are file extensions: TMY2, TMY3, EPW and CSV.

7. Results and discussion

To optimise the performance of the solar tower system for different regions, the solar fields are optimised by the variation of the Solar Multiple (SM) as a function of storage hours (TES), in order to find the optimal dimensions of the system and maximise the production of electricity and the capacity factor of the solar tower system. In our study, we use the System Advisor Model (SAM) software which proved to be among the most suitable tools with respect to our study.

7.1. Region of Béchar

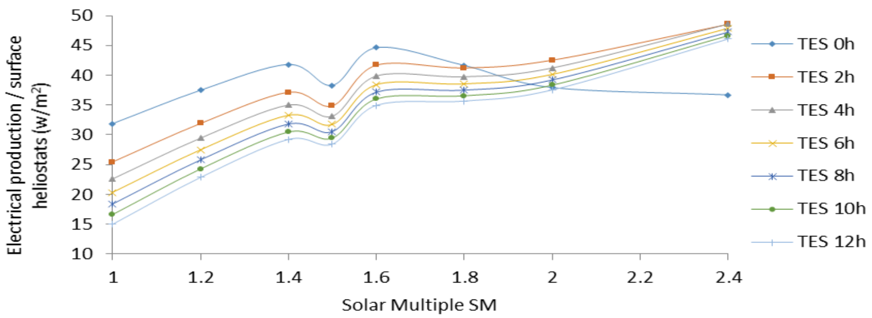

Fig. 6. The solar multiple effect (SM) on electrical production/(the surface of heliostats)m^2 under different values of TES (BECHAR)

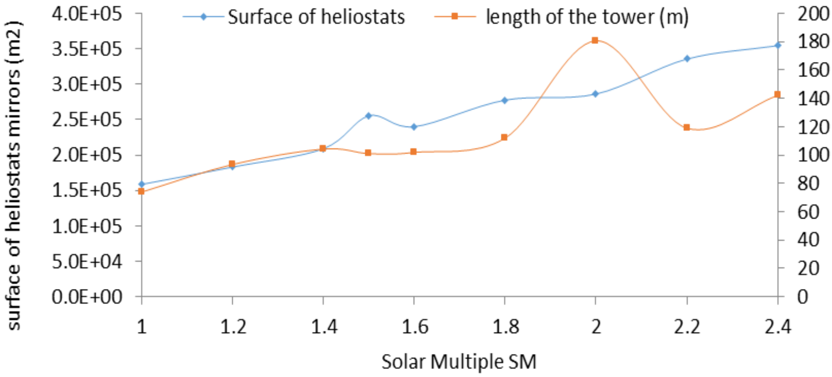

Fig. 7. The solar multiple effect on the surface of the heliostats mirrors (m2) and the length of the tower (m) (BECHAR)

In Figure 6, it can be observed that the electrical production per square meter of heliostat increases proportionally with the SM, except for the decrease recorded in the interval SM = [1.4, 1.5] due to the increase in the surfaces of the heliostats mirrors and the decrease in the length of the tower, which are influenced by the loss due to the effects of the heliostat field as indicated in Figure 7. Beyond SM = 1.6, the increase in the solar field area has no effect on electrical production which converges and increases slightly due to the effects corresponding to the enormous expansion of the solar field and atmospheric attenuation.

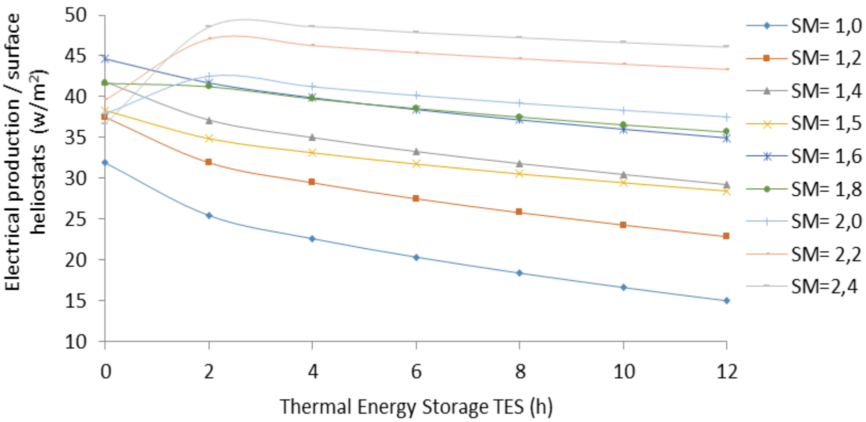

Fig. 8. The effect of TES on electrical production/m² (surface heliostats) under different values of the solar multiple (BECHAR)

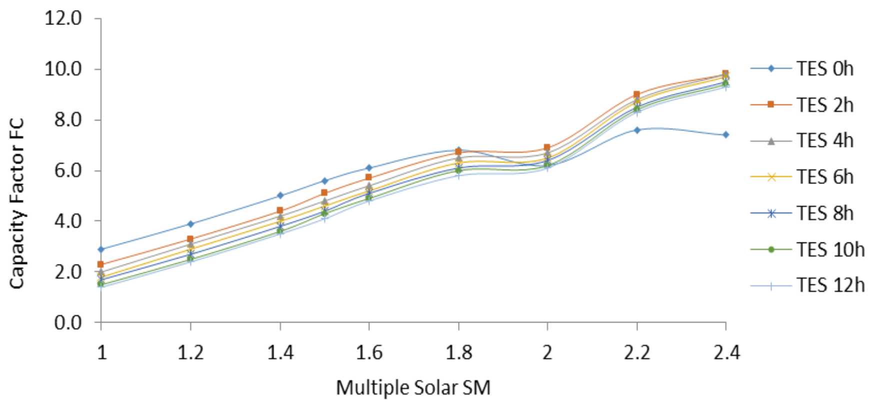

Fig. 9. The multiple solar effect on CF capacity factor under different TES values (BECHAR)

For SM = 2.0, 2.2 and 2.4 the electrical production per m^2 increases to peak at: 42.53 w/m^2, 47.07 w/m^2 and 48.55 w/m^2 for TES = 2h, then it decreases as shown in Figure 8. The configuration of the plant in these values requires a large area, which is economically impractical. Therefore, the electrical production at the start of our system for SM = 1.8 is larger, decreases slightly to TES = 2h and then coincides with the curve corresponding to SM = 1.6.

The capacity factor CF evolves proportionally with the SM. The graphs converge, as shown in Figure 9, except for the graph corresponding to TES = 0h and SM = 2.2, which begins to descend slightly. This decrease is due to the loss of excess of the non-stored energy received by the receiver.

From the above, we can conclude that the optimal point of operation of our system corresponds to the following coordinates: SM = 1.8, TES = 2h and the electrical production is 11.44 GWh/year.

7.2. Region of El Oued

In Figure 10, it can be seen that the electrical production per square meter of heliostat's increases proportionally with the SM, except that there is a decrease recorded in the interval SM = [1.2 1.4] where the length of the tower has exceeded the surface of the corresponding heliostat mirrors, - thus decreasing to 80 m to resume the increase in electricity production in the interval SM = [1.4 1.5], as shown in Figure 11. Beyond SM = 1.5, the curves of electrical production continue parallel to their growth, however, the value of the electrical output remains constant, at SM = 1.2, showing the optimal surface of the solar field.

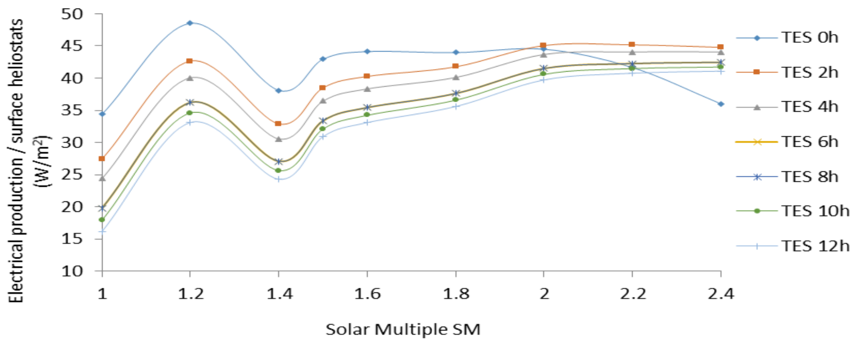

Fig.10. The Solar Multiple effect on electrical production/m^2 (surface heliostats) under different TES values (EL OUED)

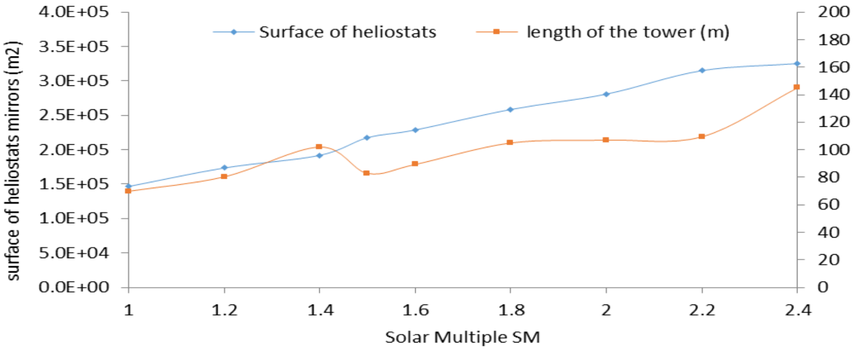

Fig. 11. The Solar Multiple Effect on Surface Mirrors Heliostats (m^2) and Length of Tower (m) (EL OUED)

For SM = 2.0, 2.2 and 2.4, the electrical production per m^2 increases until the peak values: 45.07 w/m^2, 45.18 w/m^2 and 44.79 w/m^2 for TES = 2h then it drops as explained in Figure 12. The configuration of the plant in these values requires a large area of the heliostat field, which is not profitable. Consequently, the electrical production at the start of our system for SM = 1.2 is greater, drops slightly up to TES = 2h and then coincides with the curve corresponding to SM = 1.8.

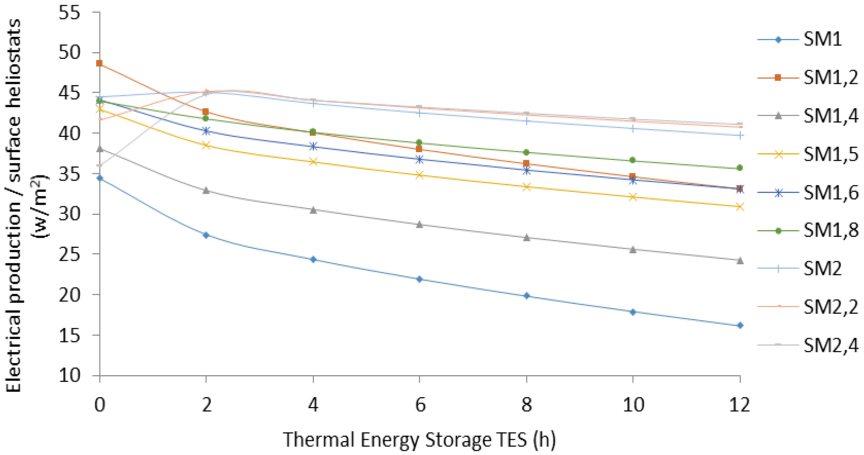

Fig. 12. The effect of TES on electricity production/m^2 (surface heliostats) under different values of solar multiple (EL OUED)

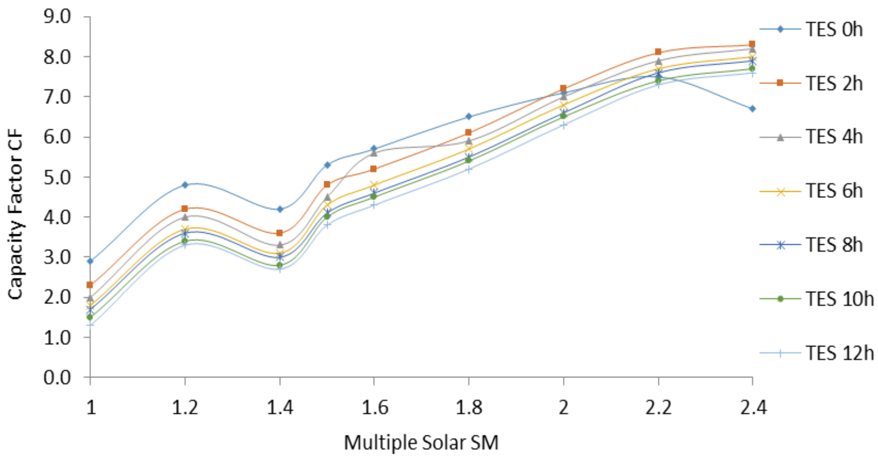

Fig. 13. The solar multiple (SM) effect on capacity factor (CF) under different TES values (EL OUED)

The capacity factor (CF) evolves proportionally with the solar multiple (SM), the curves increase in parallel and tend towards close values, as shown in Figure.13, except for the curve corresponding to TES = 0h and SM = 2.2 which begins to descend slightly due to the loss of excess of the non- stored energy received.

From the above, we can conclude that the optimal point of operation of our system corresponds to the following coordinates SM = 1.2, TES = 2h and the electrical production is 7.4 GWh/year.

7.3. Region of Djelfa

In Figures 14, 15 and 16 the following variations can be distinguished:

- For TES = 0h-4h: the electrical production per square meter of heliostat's increases respectively with SM = 1.2, SM = 1.6 and SM = 2 and subsequently decreases.
- For TES = 6h-12h: the electrical production per square meter of heliostat increases proportionally with the SM to a converging value.
- For SM = 2.0, 2.2 and 2.4: The electricity production per m^2 of heliostat increases proportionally with TES. For the other SM, the electrical production increases until TES = 2h then it decreases. Except for SM = 1.8, the electrical production is viable for TES exceeding 4h. The configuration of our system becomes unprofitable (a large area, large dimensioning of the tower). On the other hand, the starting power of the plant is much better for SM = 1.5 and remains almost stable for TES = 4h.
- The capacity factor (CF) evolves proportionally with the solar multiple (SM, the curves increase proportionally and tend towards close values, except for TES = 0h, 2h and 4h, as in Figure 17.

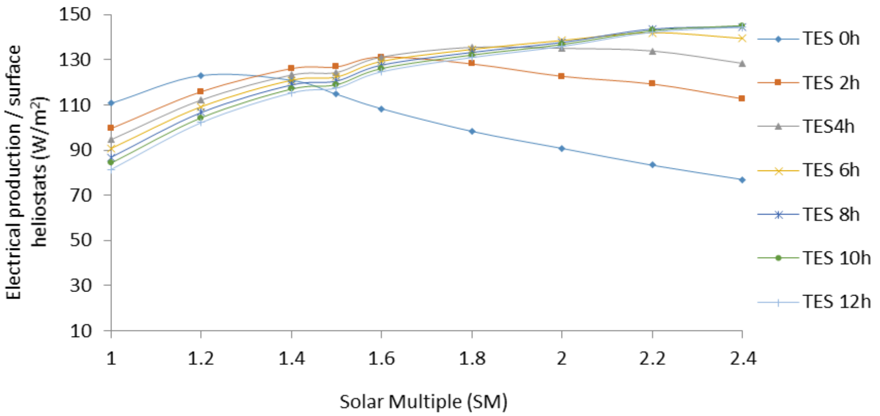

Fig. 14. Solar Multiple (SM) effect on electrical production/m^2 (surface heliostats) under different TES values (DJELFA)

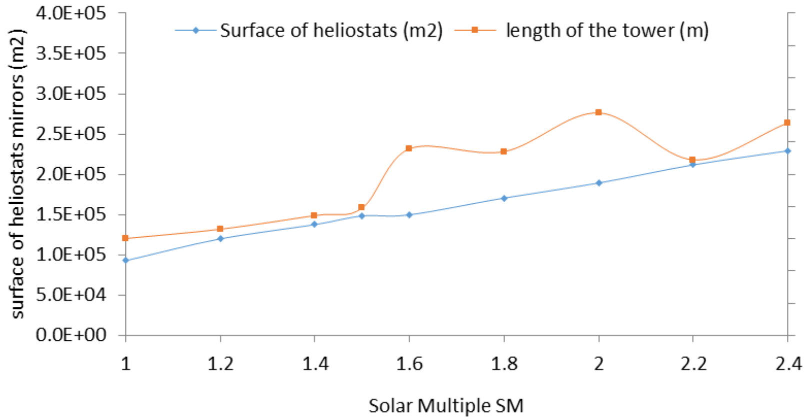

Fig. 15. Solar Multiple (SM) effect on mirror surface heliostats (m^2) and length of the tower (m) (DJELFA)

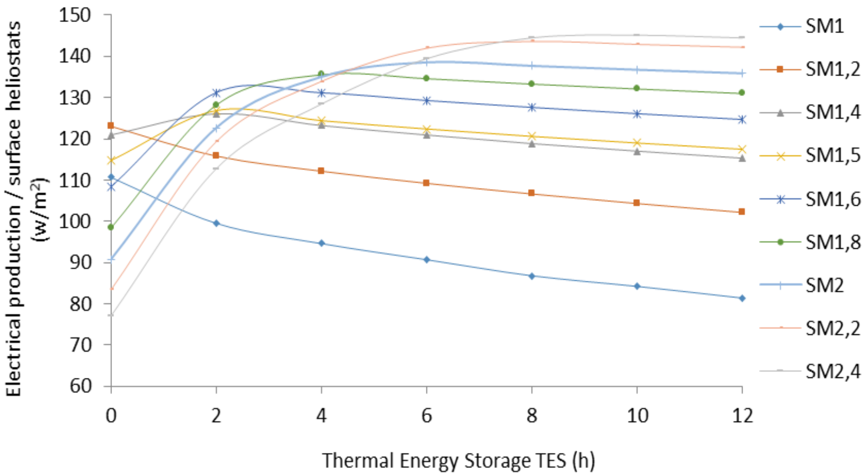

Fig. 16. The effect of TES on electrical production/m^2 (surface heliostats) under different solar multiple values (DJELFA)

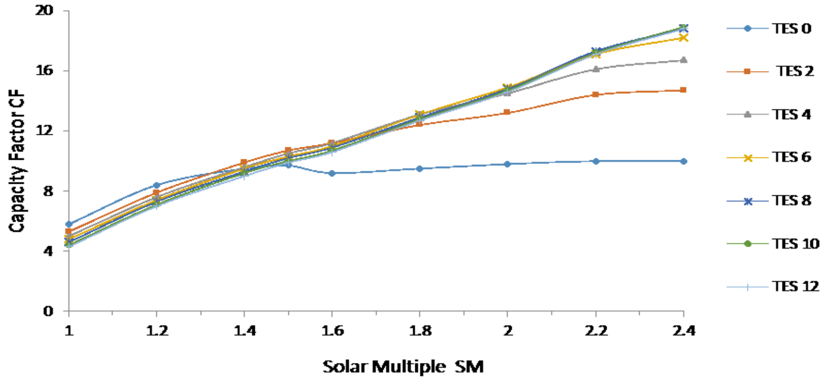

Fig. 17. Solar Multiple (SM) Effect on Capacity Factor (CF) under Different TES Values (DJELFA)

From the above, we can conclude that the optimal point of operation of our system corresponds to the following coordinates SM = 1.5, TES = 4h and the electrical production is 18.45 GWh/year.

Tab. 3. Parameters of the model validation (simulated case location: DjelfaetBatna, Algeria. Planta Solar 20 location: Sanlucar, Andualusia, Spain)

Parameter	Planta Solar 20 (PS20) [23]	Simulated case, scenario 1[12]	Simulated case, scenario 2[12]	Simulated case, our study
Annual DNI (kW h/m2)	1944	1907.30	1907.30	2416.3
Hybridisation (%)	15	0	15	0
Net energy production (GW h/year)	48	18.15	44.40	18.45
Net energy production difference (%)	7.5 (scenario 2 and PS20)			1.6 (scenario 1 and our study)
Annual capacity factor (%)	27	10.6	26	10.5

7.4. Optimisation of the field of heliostats

From the analysis of the optimal points of operation of our CSP system of three regions, presented in the preceding section, we can conclude that the optimal heliostat field corresponds to the solar multiple and storage hours: SM = 1.8, TES = 2h for Becher region; SM = 1.2, TES = 2h for El Oued region and SM = 1.5, TES = 4h for Djelfa region.

The simulation results are shown in Figures 18, 19 and 20.

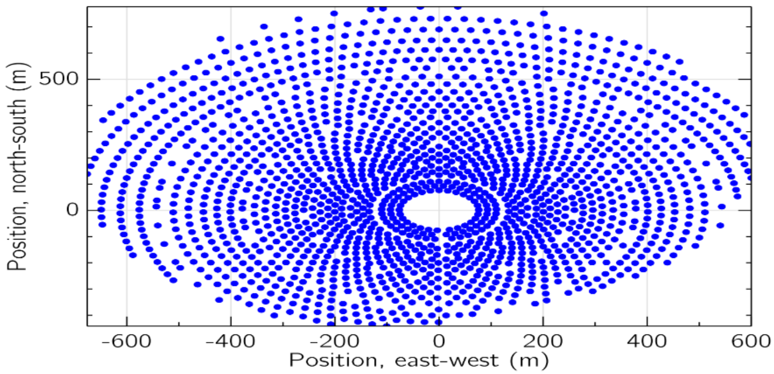

Fig. 18. CSP heliostats field configuration of Béchar region

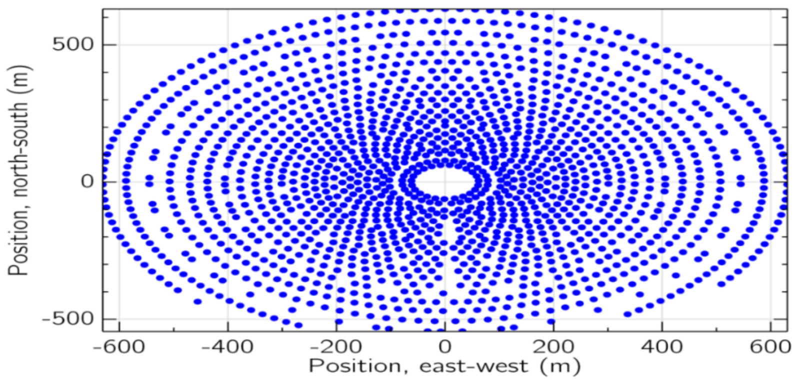

Fig. 19. CSP heliostats field configuration of El Oued region

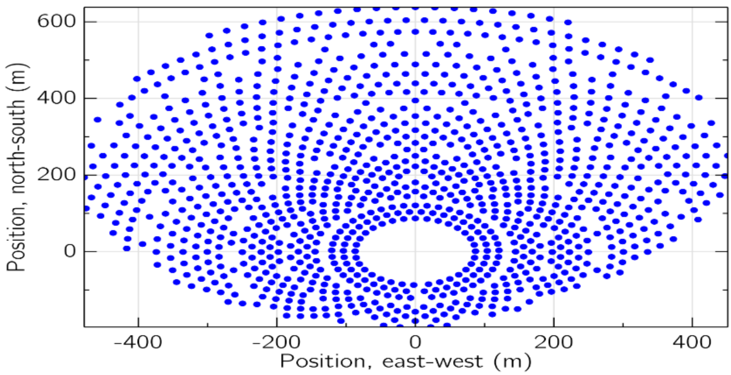

Fig. 20. CSP heliostats field configuration of Djelfa region

8. Conclusion

In this paper, we presented a comparative study of three power stations located in the regions of El Oued, Béchar and Djelfa, which are part of the Algerian energy programme. Each plant is equipped with a molten salt storage mode, the receiver is of external type and the implantation of the field of heliostats that has been defined for an annual production of 20 MW.

The results obtained from different simulations with SAM software, based on real data of the first two regions and those collected by satellite for Djelfa region, lead to the following observations.

- The "DNI" is the fundamental factor of a region choice. A high value of DNI corresponds to a high performance of the solar power plant resulting in high production and storage capacity. Therefore, the study of thermodynamic plants is much more interesting for DNI than GHI' and DHI.
- Satellite meteorological data give higher results (Djelfa) compared to the real data. In this case, the electrical production can be twice as high as in the real data because the latter takes into account atmospheric conditions (cloud, wind, pollution...).
- There is a strong relationship between Solar Multiple (SM), power generation and storage capacity. Higher SM corresponds to higher production and storage capacity. The hours of storage do not cover the whole night, the increase in the number of heliostats and, therefore, the SM factor , is essential for a primary or an auxiliary source of energy to guarantee its permanent activity during all the day.
- The design of a field of heliostats is related to a set of parameters having a large number of degrees of freedom and the influence of these parameters on each other. The starting layout must be very close to the optimum configuration (the height of the tower, the surface of mirrors, dimension of

the receiver...), therefore, a more economical and better-performing heliostat concentrator is much needed.

As prospects for future research, we will use the performance of the Solar Advisor Model (SAM) for integrating financial modelling into actual project models.

References

[1] S. Boudghene; Z. Khiat;, S. Flazi; Y. Kitamura,”A review on the renewable energy development in Algeria: Current perspective, energy scenario and sustainability issues”, *Renewable Sustainable Energy Review,* vol. 16, pp. 4445–4460. 2012.

[2] A.B. Stambouli, “Promotion of renewable energies in Algeria: Strategies and perspectives”, *Renewable Sustainable Energy Review*, vol. 15, pp. 1169–1181, 2011.

[3] Energies Nouvelles, Renouvelables et Maitrise de l’Energie Available online: http:// www. energy .gov. dz/francais/index.php? page=energies - nouvelles - renouvelables - et - maitrise - de - lenergie (accessed on 22 May 2018).

[4] Medium Term RE Market Report, Agence Internationale de l’Energie. 2013. Available online: https: //www.iea.org/publications/ freepublications/publication /2013MTRMR.pdf (accessed on 22 May 2018).

[5] A. Ghezloun; S. Chergui, N. Oucher, “Algerian energy strategy in the context of sustainable development (Legal framework)”, *Energy Procedia*, vol. 6, pp. 319–324, 2011.

[6] Portail Algérien des Energies Renouvelables. Available online: https://portail.cder.dz/spip.php? article4446 (accessed on 22 May 2018).

[7] H.E. Imadojemu, “Concentrating parabolic collectors: A patent survey”, *Energy Conversion and Management*, vol. 36, pp. 225–237, 1995.

[8] B. Hocine Moussa, Thermal Solar Power Plants in Algeria and Desertec Mega project. In Proceedings of the Le 1erés Journées d’Etudes de Mécaniques, Batna, Algeria, 29–30 November 2011.

[9] M.A. Rosen, I. Dincer, “Exergy–cost–energy–mass analysis of thermal systems and processes”, *Energy Conversion and Management*, vol. 4, pp. 1633–1651, 2003.

[10] Adinberg, R., “Simulation analysis of thermal storage for concentrating solar power”, *Applied Thermal Engineering* 31, 3588–3594, 201.

[11] Annuaire de la Filière Française du Solaire Thermodynamique. 2011. Available online: http:// www.enr.fr/ userfiles/files/Annuaires/ 2011171733_ annuairethermo 2011.pdf (accessed on 22 May 2018).

[12] S Boudaoud, A. Khellaf, K. Mohammedi, O. Behar, “Thermal performance prediction and sensitivity analysis for future deployment of molten salt cavity receiver solar power plants in Algeria”, *Energy Conversion and Management*, vol. 89, pp. 655– 664, 2015.

[13] O. Behar, A. Khellaf, K. Mohammedi, “A review of studies on central receiver solar thermal power plants”, *Renewable Sustainable Energy Review*, vol. 23, pp. 12–39, 2013.

[14] S. Mihoub, A. Chermiti, H. Beltagy, “Methodology of determining the optimum performances of future concentrating solar thermal power plants in Algeria”, *Energy,* vol. 122, pp. 801–810, 2017.

[15] M. Ouagued, A. Khellaf, L. Loukarfi, “Estimation of the temperature, heat gain and heat loss by solar parabolic trough collector under Algerian climate using different thermal oils”, *Energy Conversion and Management*, vol. 75, pp. 191–201, 2013.

[16] P. Gilman, N. Blair, M. Mehos, C. Christensen, S. Janzou, C. Cameron, “Solar Advisor Model. User Guide forversion 2.0”, Technical report NREL/TP - 670 - 43704; August 2008. Available online: https://www.nrel.gov/docs/ fy08osti/ 43704.pdf (accessed on 22 may 2018).

[17] B. L. Kistler, “A User’s Manual for DELSOL3. A Computer Code for Calculating the Optical Performance and Optimal System Design for Solar Thermal Central Receiver Plants. SAND86 - 8018. Unlimited release UC - 62a”, 1986.

[18] W. Huang, “Development of an analytical method and its quick algorithm to calculate the solar energy collected by a heliostat field in a year”, *Energy Conversion and Management*, vol. 83, pp. 110–118, 2014.

[19] M. J. Wagner, “Simulation and Predictive Performance Modelling of Utility Scale Central Receiver System Power Plants. Ph.D. Thesis”, University of Wisconsin: Madison, Madison, WI, USA, January 2008.

[20] M. Romero - Álvarez, E. Zarza, “Concentrating solar thermal power. In Handbook of Energy Efficiency and Renewable Energy”, *CRC Press: Boca Raton, FL, USA*, 2007.

[21] Modelling and Calculation of Heat Transfer Relationship for Concentrated Solar Power Receivers. Available online: https://search.library.wisc.edu/catalog /9910121576302121 (accessed on 30 May 2018).

[22] ReGrid: Concentrated Solar Power. (RENAC) Renewables Academy. Schonhauser Alee 10–11.10119. Berlin, Germany. Available online: https://www.renac.de /en/projects/ (accessed on 22 May 2018).

[23] Solar power for a sustainabel world.PS 20 Available from:<http://www.abengoasolar.com/web/en/nuestras_plantas/plantas_en_operacion/espana/PS20_la_mayor_torre_comercial_delmundo.html>.

Daniel Wyrwał[1], Tymoteusz Lindner[2], Tomasz Kapłon[3],

AUTONOMOUS NAVIGATION FOR INDOOR MOBILE ROBOT BASED ON ROS

Keywords: ROS, SLAM, mobile robot, navigation, autonomous, LIDAR

Abstract

Mobile robots are becoming more and more popular in indoor conditions applications. Typical mapping robots are equipped with big, heavy and expensive computing units onboard. In the paper authors attempt to take advantage of the building's infrastructure and present a robot that is not bound by these restrictions. The paper presents a low-cost, high-performance and relatively simple structure for mapping, localisation, and navigation, which is then subjected to experimental verification. The paper describes a system that is divided into two main modules. The first module is the mobile platform with sensors and minimum amount of computing capability. The second module is a high-performance computer performing all calculations related to mapping, localisation and navigation. The robot collects information from the environment and sends it directly to the central computer where mapping and localisation is executed. Subsequently, the central computer sends the processed data to the mobile platform. Because the main processing computer is physically separated from the mobile robot platform, the system is fully modular and one computer may be used to control multiple robots. As a result of the proposed solution, a small, light and inexpensive mobile platform with the capability for navigating through self-created environment map can be built.

1. Introduction

The rapid development of robot technology, autonomous navigation and intelligent mobile robot systems causes that these are being applied in many areas. However, numerous problems must be faced concerning the use of mobile robots. The widespread use of robots makes the authors try to use universal tools for the construction of mobile robots such as a universal operating system. Other popular elements found in mobile robots are LIDAR sensors and odometry systems. One of many examples is ROS-driven wheelchair (Robot Operating System) [1] where the authors proposed a system assisting human operators to avoid obstacles. The

[1] Politechnika Poznańska, Wydział Budowy Maszyn i Zarządzania, Instytut Technologii Mechanicznej, ul. Piotrowo 3, 61-138 Poznań, Polska, daniel.wyrwal@put.poznan.pl
[2] Politechnika Poznańska, Wydział Budowy Maszyn i Zarządzania, Instytut Technologii Mechanicznej, ul. Piotrowo 3, 61-138 Poznań, Polska, tymoteusz.lindner@put.poznan.pl
[3] Politechnika Poznańska, Wydział Budowy Maszyn i Zarządzania, Instytut Technologii Mechanicznej, ul. Piotrowo 3, 61-138 Poznań, Polska, tomasz.z.kaplon@doctorate.put.poznan.pl

next example is a system for walkers that is presented in [2]. This setup is built to help the elderly and individuals with movement disorders as an assistance and rehabilitation tool. This paper presents a "smart" walker that is able to guide the users and navigate in an indoor environment as well as to create a map of the environment and detect the fall of a human. In the same paper [2] authors compared gmapping, hector slam and amcl algorithms as alternative methods for mapping the environment and establish location in a known map. All robots presented in [3]–[11] utilise the Robot Operating System, and almost all of them use LIDAR sensors and odometry data or other systems to determine the position. Unlike in the mentioned study by Cechowicz and Bogucki [4] gyroscope and odometry data showed good results in the determination of the position of a mobile platform in a short period of time. Researchers have shown that all currently-built robots have large dimensions and/or a heavy and expensive computer on board [1], [2], [6], [8] or are deprived of the ability to create a map of the environment to navigate within [4], [9], [10], [12]

This paper proposes a solution consisting in the separation of the robot with the minimum amount of components needed for LIDAR support, motors control and encoders read from a large computing unit, which can be remote from the robot, for example in another room and do it by utilising a Wi-Fi network, which is present in many buildings. Authors found two publications [10], [13] where a system based on wireless communication between ROS nodes was presented. However, the map created with a first presented robot was located in only one room and did not take the advantage of the wireless network. The second publication described a Cloud-Based system where data that was sent to the cloud and was restricted to simple ROS Messages.

2. The system setup

In this section, we present the detailed system design and setup for both the hardware and software components and connections and interactions between components of the system. The proposed solution can optimise the cost of buying and maintaining mobile robots that will work in an indoor environment with a Wi-Fi network.

Our robot platform is based on a popular construction where the entire component is placed on disk driven by two wheels mounted on the sides of a robot and one rear caster wheel. This setup allows the robot to turn around in place as well as move forward, backward and turn during movement. A similar design has been implemented in numerous studies [4], [5], [8], [9], [12], [14], [15]. The robot is shown and described in figure 1.

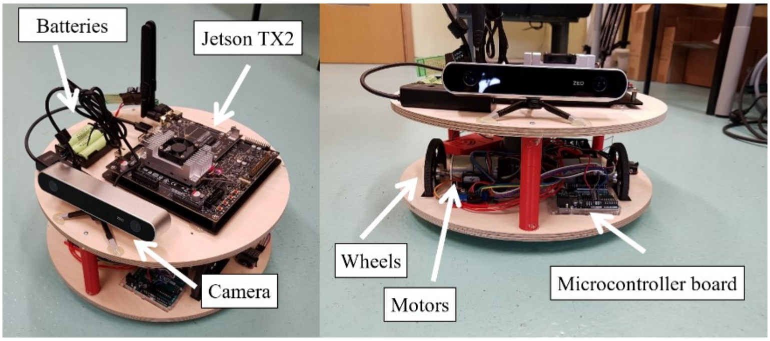

Fig.1. The mapping robot

The scheme of hardware components is presented in figure 2. The system consists of DC motors with incremental encoders and planetary gears, DC motors driver with L298 H-bridge, board with a microcontroller operating the motors and obtaining data from the encoders. Additionally, the platform is equipped with a RPLIDAR A2 device and a Raspberry Pi 3B+ minicomputer to control LIDAR.

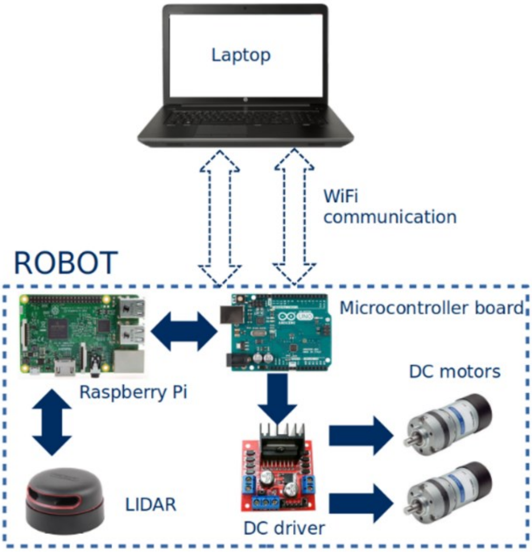

Fig. 2. Hardware scheme of the mapping robot

The platform presented in figure 1 additionally carries a Jetson TX2 board and Stereo Labs 2K ZED camera; however, these components and results that were obtained with them will not be discussed in this article.

There is one additional component that is very important but is not placed physically on the platform - a PC computer. It was resolved that a big and heavy processing computer should not be placed directly on the robot, instead the data would be computed remotely.

3. Robot Operating System

This section presents software components used in the presented robot.

3.1. Robot Operating System (ROS):

ROS [16] is an open-source operating system for robotics. It provides services that are expected from an operating system from hardware abstraction, low-level device control, message-passing and package management. It also provides tools and libraries for obtaining, building, writing and running code across multiple devices. In our mobile system, ROS is used to control different parts of the system such as the LIDAR and microcontroller board, whilst maintaining communication with each other. Moreover, it is used to send and receive data to all components by wire or wirelessly.

3.2. Simultaneous Localisation and Mapping (SLAM)

SLAM is one of the complex problems of robotics. It specifically deals with creating a map of the environment whilst localising the robot and successfully navigating through the environment to reach a desired destination. It is considered a difficult problem due to the fact that for localisation, the robot needs a consistent map. To create a consistent map, on the other hand, it needs accurate determination of its location. The dependence between the map of the surrounding environment and the robot position makes SLAM a difficult problem to tackle. Based on the study comparing two mapping algorithms: gmapping and hector slam with similar results [2], it was resolved that the gmapping algorithm would be employed in the study due to the simplicity of its implementation and the availability of documentation. In the study, the authors used gmapping to create a map and localise itself in it. The data used to create map were obtained from two sources– two encoders on wheels and LIDAR. Odometry was used to provide high rate but inaccurate data about position of the robot and LIDAR corrected the position described by the encoders and provided data for the construction of the environment map.

3.3. System analysis

We propose a system where the complex computation of localisation and mapping is performed on a remote machine. The system puts to use the Wi-Fi infrastructure that is often available in big office buildings. In the proposed system, a PC computer is placed in one room and small mobile platform obtains information from sensors, sends them to the remote PC and receives back the velocity commands without computing complex algorithm. The remote PC has all the information about the robot, such as its position, the map of the environment, the encoder position and LIDAR scans. Subsequently, the PC computes the map and then a global path and a local path, based on the actual position of the robot and the actual LIDAR scan. The whole computation is done on i7-5500 processor and takes 0.2s to compute and align the data with the existing map. It is very difficult and expensive to place platform with this amount of processing power on a small mobile platform. In comparison, Raspberry Pi 3 needs 2 – 5s to compute the same data. Because of that slow computation time, it is impossible to use SBC like Raspberry Pi to run the said SLAM algorithm and the authors abandoned further attempts to use RPi as the main computation unit.

To make the system work, the authors used several ROS packages. The first one was *navigation* [17] package. It was responsible for moving and navigation through the known map. The navigation stack was responsible for calculating the global path and a local path based on the global and local costmap. This package was one of the most complex problems to compute, therefore, it was moved to the remote PC. The *navigation_stack* [17], and the SLAM algorithm were working simultaneously. To compute the map and localise the robot the authors used *gmapping* [18] algorithm. The results of *gmapping, global costmap* and *local costmap* are shown in figure 4.

One of the components on the mobile platform was Raspberry Pi minicomputer that runs Ubuntu MATE operating system, which is a GNU/Linux compilation for ARM processors. Ubuntu was used because it is officially supported by ROS. Packages that run directly on the robot are: *rplidar* [19], *diff_drive_controller* [20] and *rosserial_python* [21]. The first is used to handle LIDAR. The next package was modified to convert commands such as the velocity and turning to the speed of each wheel. The last package was responsible for communication with microcontroller board through the serial port. A simplified diagram of the system is shown in figure 3.

ROS works on the concept of nodes and topics. Nodes are simple programmes and topics are the way to communicate between nodes. Nodes and topics are independent of the programming language. Programmes used by authors are written in C++, C and python. ROS provides the mechanism for the topic to work and it is based on TCP/IP and UDP communication. TCP/IP connection can be established both within one computer and via cable as well as wirelessly. Because of this feature of ROS, authors proposed to utilise Wi-Fi connection. Both the mobile platform and PC was connected to the same Wi-Fi network. *Ros_master* node was run on mobile platform and *ROS_MASTER_URI* was set to IP address of the robot on both PC and robot.

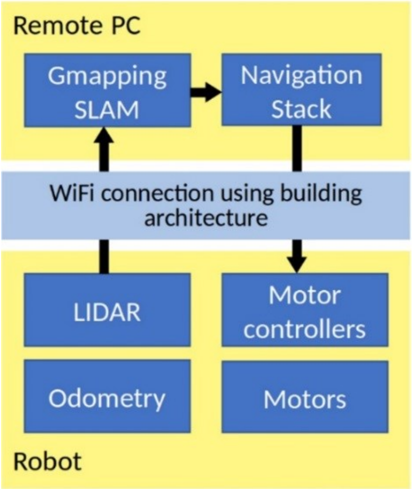

Fig. 3. Simplified scheme of the presented system

4. Results

The robot's task was to move from the starting point to the end designated by the operator in an unknown environment. Along the way, the system had to create a map and avoid obstacles. The designated point has to be either on the known part of the map or the unmapped area. The task is complete when the robot is within 0.5 m of the destination. The environment was the hallway of an office building with a flat floor.

The results of the system work are presented in figure 4. The image on the left shows a simple map that was created on a remote machine and red dots that presents LIDAR data. On the right, the local costmap and the outline of the robot are marked.

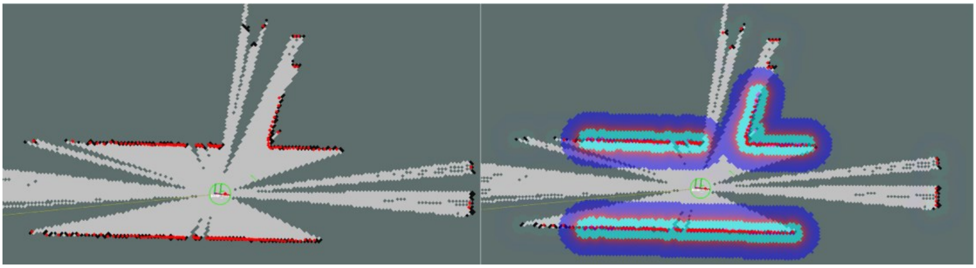

Fig. 4. a) the created map, b) the map witch local and global costmap

The work of all the ROS packages is shown in figure 5, showing a map with walls of the room. Additionally, global and local costmaps are shown. LIDAR data is presented as red dots along the walls. The outline of the robot and its global path are visible.

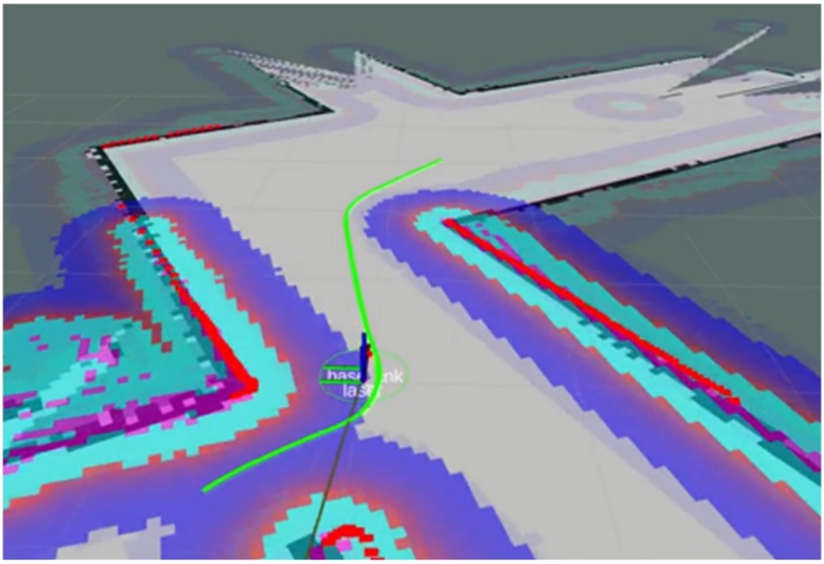

Fig. 5. Visualisation of the moving robot

In figure 6, the 50x40 m map is presented. The place where the PC computing the map was located and the actual position of robot. The maximum distance between the robot and the computer was approx. 70 m through walls, which means it would be impossible to perform without the system proposed by authors.

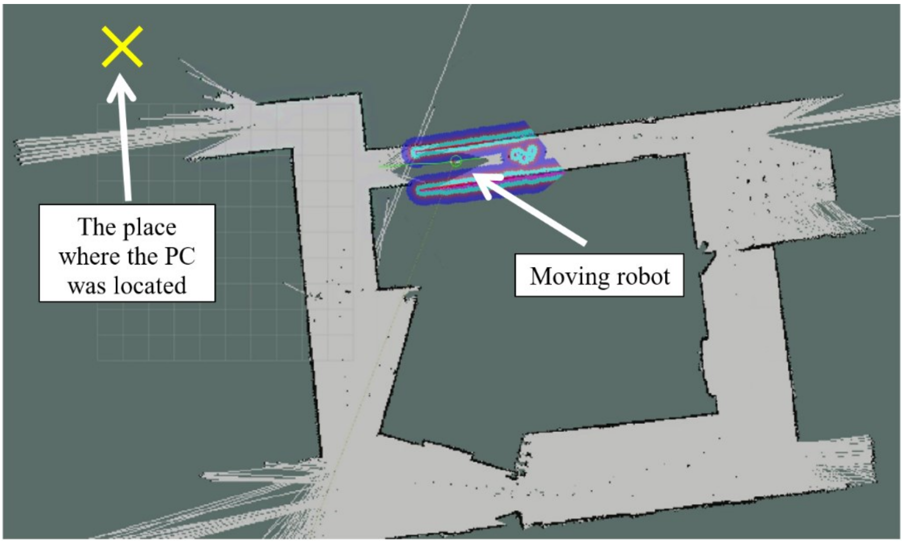

Fig. 6. The floor map of the office building

5. Conclusions and further research

The proposed system that consists of a remote PC and a small mobile platform of limited processing power proved to be a suitable solution for small mobile platforms that are not able to carry out a big and heavy computer that is essential to compute complex SLAM algorithms. The authors utilised the infrastructure of the building Internet network to communicate between the mobile platform and the remote PC. The wireless network utilised by the authors was a standard Wi-Fi network found in big office buildings. Moreover, the system proposed in this article can cooperate in a similar manner with other robots that send data to the main computer.

The proposed system does have certain drawbacks. The stability of the network connection is required for the system to work. Additionally, any delay on the part of the system may prove to exceed the capacity of some real-time applications such as fast-moving robots.

The future research will concentrate on the improvements of the motion detection procedure, as it is crucial for the accuracy and practical applications. One of the example solutions is to use smart MEMS sensors as in different studies [4]. The second improvement the authors will implement is to utilise cameras. Similar construction where presented in other studies [4], [7], [9], [10]. The authors will try to send the data from the camera to a remote PC and send back only minimal information the robot needs to operate. It should reduce the cost of high-performance computers that would no longer be required on robots with computer vision systems.

Acknowledgements

The work described in this paper was funded from 02/22/SBAD/1505.

References

[1] H. Grewal, A. Matthews, R. Tea, and K. George, "LIDAR-based autonomous wheelchair", in *2017 IEEE Sensors Applications Symposium (SAS)*, pp. 1–6, 2017.

[2] P. Kashyap, M. Saleh, D. Shakhbulatov, and Z. Dong, "An Autonomous Simultaneous Localization and Mapping Walker for Indoor Navigation", in *2018 IEEE 39th Sarnoff Symposium*, pp. 1–6, 2018.

[3] N. V. Belov, D. P. Airapetov, B. Y. Buyanov, and V. A. Verba, "SLAM Implementation For Mobile Robots Using Physical Sensors", in *2019 Systems of Signals Generating and Processing in the Field of on Board Communications*, pp. 1–6, 2019.

[4] R. Cechowicz and M. Bogucki, "Indoor vehicle tracking with a smart MEMS sensor", *MATEC Web Conf.*, vol. 252, pp. 02004, 2019.

[5] Y. Cheng and G. Y. Wang, "Mobile robot navigation based on lidar", in *2018 Chinese Control And Decision Conference (CCDC)*, pp. 1243–1246, 2018.

[6] R. Kangutkar, J. Lauzon, A. Synesael, N. Jenis, K. Simha, and R. Ptucha, "ROS Navigation Stack for Smart Indoor Agents", in *2017 IEEE Applied Imagery Pattern Recognition Workshop (AIPR)*, pp. 1–10, 2017.

[7] Z. Li, Y. Xiong, and L. Zhou, “ROS-Based Indoor Autonomous Exploration and Navigation Wheelchair”, in *2017 10th International Symposium on Computational Intelligence and Design (ISCID)*, vol. 2, pp. 132–135, 2017.
[8] X. Liu, X. Luo, and X. Zhong, “Research on simultaneous localization and mapping of indoor mobile robot”, *J. Phys.: Conf. Ser.*, vol. 1074, p. 012099, Sep. 2018.
[9] A. West, F. Arvin, H. Martin, S. Watson, and B. Lennox, “ROS Integration for Miniature Mobile Robots”, in *Towards Autonomous Robotic Systems*, , pp. 345–356, 2018.
[10] J. Wu, C. Lv, L. Zhao, R. Li, and G. Wang, “Design and implementation of an omnidirectional mobile robot platform with unified I/O interfaces”, in *2017 IEEE International Conference on Mechatronics and Automation (ICMA)*, pp. 410–415, 2017.
[11] Y. Wu and Z. Ding, “Research on Laser Navigation Mapping and Path Planning of Tracked Mobile Robot Based on Hector SLAM”, in *2018 International Conference on Intelligent Informatics and Biomedical Sciences (ICIIBMS)*, vol. 3, pp. 59–65, 2018.
[12] J. Montusiewicz and S. Skulimowski, “Multicriteria evaluation of the trajectory of a wheeled mobile robot – a case study”, *MATEC Web Conf.*, vol. 252, p. 09007, 2019.
[13] Q. Gao and H. Cheng, “Design of a CloudROS enabled Mobile Robot”, in *2018 IEEE International Conference on Robotics and Biomimetics (ROBIO)*, pp. 2487–2492, 2018.
[14] S. Gatesichapakorn, J. Takamatsu, and M. Ruchanurucks, “ROS based Autonomous Mobile Robot Navigation using 2D LiDAR and RGB-D Camera”, in *2019 First International Symposium on Instrumentation, Control, Artificial Intelligence, and Robotics (ICA-SYMP)*, pp. 151–154, 2019.
[15] V. Thapa, S. Capoor, P. Sharma, and A. K. Mondal, “Obstacle avoidance for mobile robot using RGB-D camera”, in *2017 International Conference on Intelligent Sustainable Systems (ICISS)*, pp. 1082–1087, 2017.
[16] “Documentation - ROS Wiki.” [online]. Available: http://wiki.ros.org/. [Accessed: 04-Oct-2019].
[17] “navigation - ROS Wiki.” [online], available: http://wiki.ros.org/navigation. [Accessed: 04-Oct-2019].
[18] “gmapping - ROS Wiki.” [online], available: http://wiki.ros.org/gmapping. [Accessed: 04-Oct-2019].
[19] “rplidar - ROS Wiki.” [online], available: http://wiki.ros.org/rplidar. [Accessed: 04-Oct-2019].
[20] “diff_drive_controller - ROS Wiki.” [online], available: http://wiki.ros.org/diff_drive _controller. [Accessed: 04-Oct-2019].
[21] “rosserial - ROS Wiki.” [Online]. Available: http://wiki.ros.org/rosserial. [Accessed: 04-Oct-2019].
[22] M. Aladem and S. A. Rawashdeh, “Lightweight Visual Odometry for Autonomous Mobile Robots”, *Sensors*, vol. 18, no. 9, pp. 2837, Sep. 2018.
[23] K. Asadi *et al.*, “Vision-based integrated mobile robotic system for real-time applications in construction”, *Automation in Construction*, vol. 96, pp. 470–482, Dec. 2018.

Arkadiusz Urzędowski[1], Dorota Wójcicka-Migasiuk[1], Joanna Styczeń[2]

OPTIMISATION OF THE CIVIL STRUCTURE DESIGN PROCESS WITH BIM APPLICATION

Keywords: design optimisation, BIM, CAD, architecture, construction

Abstract

The presented study shows the results of experimental design process of the architectural documentation, for a simplified sample of public building. Two approaches to design with the use of computer tools were presented: computer-aided design and modelling of building information, represented by respective Autodesk programmes: AutoCAD and Revit. The first section presents the practical application of BIM, i.e. tools and differences in working with both approaches in the works on 3D models. The second section presents selected fragments from the modelling process stages, as well as creating technical documentation. The results were discussed in section three to indicate the benefits of the BIM technology: short working time, the ease of use, the system's capability to automatically update the 3D model based on changes introduced in 2D drawings. The presented fragments of the design process show that although working in CAD environment is more laborious, it simplifies the creation of object elements, which are furthermore characterised by a greater detail. Therefore, the assumption that BIM accelerates and optimises the process of design has been justified and extensively confirmed.

1. Introduction

1.1. Building information modelling in practice

Up to the 1980s, designers and constructors had to resolve to the traditional technical drawing method: the rapitographs and paper. AutoCAD-80 for a CP/M-80 computer and AutoCAD-86 for an IBM-Victor 9000 computer, presented at the COMDEX'82 by Autodesk, revolutionised the construction industry. Computer-aided design software tools began to take the market of 2D drawings and 3D models. In the second half of the 1980s, Autodesk was considered one of the most dynamically growing companies in the thriving software industry.

In mechanical engineering, SolidWorks company, founded in 1993, was the first to offer a widely available 3D CAD system working in the Windows environment and on a PC platform. This enabled the constructors to carry out an efficient process of modelling machine parts and assemblies. Thanks to this

[1] Lublin University of Technology, Fundamentals of Technology Faculty, 38 Nadbystrzycka St., 20-618 Lublin, Poland, a.urzedowski@pollub.pl

[2] Lublin University of Technology, Civil Engineering and Architecture Faculty, 40 Nadbystrzycka St., 20-618 Lublin, Poland, j.styczen@pollub.pl

approach, among others, it was possible to improve the process of generating 2D documentation based on three-dimensional models, and visualisation of modelled components [1].

In construction, the capabilities of 3D modelling were, however, largely insufficient as to effectively improve the work of designers from across industries. Building Information Modelling (BIM) is a digital representation of physical and functional characteristics of a facility. BIM and similar technologies feature more than just 3D (width, height, and depth) as they may encompass further dimensions, such as 4D (time), 5D (cost), and even 6D (as-built operation). The underlying idea of the system is to focus data around a single source of information, also referred to as a Common Data Environment. Thus, a project would revolve around reports, drawings and models contained in the Common Data Environment. Everything would be better-organised and better-planned. Essentially, it became more important to spend additional time planning so that the execution could be done seamlessly and with no time waste. One of the biggest advantages of working with BIM is avoiding collisions [2]. The idea of many designers working on one model, supervised by the project manager, is a solution that eliminates the overlap between the drawing of particular construction parts and installations in one place. Furthermore, this approach allows implementing the newest technologies for the analysis and presentation of the three-dimensional models, including Virtual Reality (VR) or 3D printing [3].

The first documented use of the term "model building information" appeared in a 1992 paper. The acronym BIM denoting "Building Information Modelling" was first used by Jerry Laiserin in works from the beginning of the 21st century. Parallel to the development of the BIM idea, many platforms supporting design software were developed. Laiserin, in consultation with major software providers (Autodesk, Bentley Systems and Graphisoft), accounting for over 90% of the US market (in 2002), introduced the BIM as systematisation of the most recent possibilities of software-supported design in construction.

There are currently four levels under which Building Information Modelling can be classified. At Levels 0 and 1 there is either a lack of BIM or an over-reliance on different systems of data. In April 2016, the UK Government mandated compliance with BIM Level 2 in order to fund any public sector construction project. At Level 2 there is a structure to the data for a built asset which requires collaboration across the supply chain. BIM Level 3 will be defined and targeted once the construction industry has achieved compliance with Level 2. As of April 2016, all UK government construction suppliers tendering for centrally-procured government projects must be working at BIM Level 2. Virtually all objects for the London Olympics were designed with the use of BIM [4], and in addition, all government projects in the USA should be developed in BIM as well.

Fig. 1. Visualisation of a community centre building in Wierzbica. The South-West view

The project documentation implemented in this paper contains a reconstruction of a village community centre building in Wierzbica – Fig. 1. The building was erected in the 20th century as a one-storey building, without a basement, in traditional technology with brick walls. The structural layout of the building has remained unchanged since its erection. The building's dimensions are approx. 12.2 x 18.2 m and it is made of full silicate brick, concrete blocks on cement and lime mortar. The wall thickness is approx. 42 cm and 24 cm. Ceilings - WPS prefabricated slabs laid on steel beams IPN 140 and 2xC180, approximate spacing 115 cm. Non-plastered walls from outside; from the inside plastered with cement. The foundation walls with a cavity below the existing ground level approx. 130 cm, width of foundation walls approx. 40-45 cm. Roof truss structure – wooden, in a rafter system, roofing – flat plate. The project included the modernisation of the existing building. A new roof truss was designed – a gable roof sloped at 30-58%. The roof is covered with a standing seam plate. The external walls of the building have been lifted to one level. The entire building was insulated with materials which fulfilling the requirements of thermal conditions for buildings.

1.2. Modelling tools

There is a wide variety of commercially-available CAD and BIM software. However, the most popular manufacturer is Autodesk, hence AutoCAD 2019 and Revit 2019 have been chosen for the sake of the article. AutoCAD has been immensely popular among the majority of companies in the construction industry for many years all over the world. This is a leading product of Autodesk, which has been constantly developed for 39 years. It enables preparing the technical documentation on a plane and modelling in the three-dimensional space. AutoCAD programme contains various work areas, including drawing and description, standard version or 3D modelling. Each is equipped with tools dedicated to working in a selected area. However, all commands and functions for drawing, modifying and modelling are available in relevant workspaces [5].

Autodesk Revit is a building information modelling application for architects, landscape architects, structural engineers, mechanical, electrical and plumbing engineers, designers and contractors. The original software was developed by Charles River Software, founded in 1997, renamed Revit Technology Corporation in 2000, and acquired by Autodesk in 2002. Extensive software capabilities, as well as compatibility with drawings performed in AutoCAD and other CAD programs are among the key factors deciding of its popularity in the design industry.

1.3. The designing process: AutoCAD v Revit

AutoCAD and Revit represent two completely different approaches to modelling. Instead of designing with a ruler and a pen, AutoCAD allows drawing 2D lines representing real elements, hence the term Computer-Aided Design. In contrast, in Revit designers build 3D components equipped with real-life information, hence the term Building Information Modelling [6]. In AutoCAD, each element must be drawn separately: it has to be worked on a plan then on a façade or a section. The advantage of this approach is that processes can be somehow unrestrained because the drawings are not linked to each other.

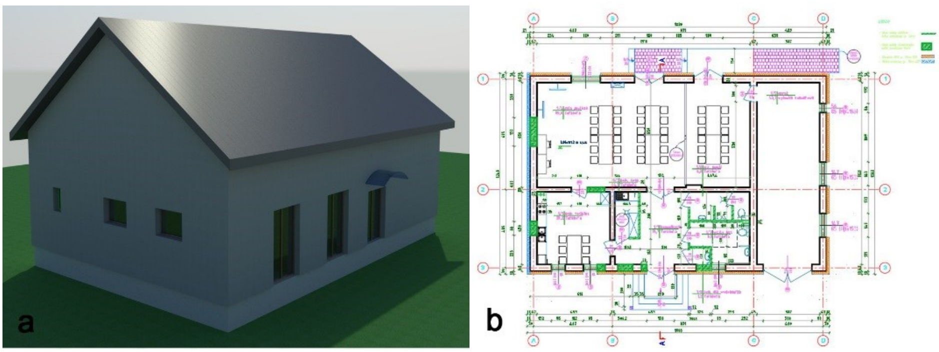

Fig. 2. a) Designed building 3D model, during working at AutoCAD. North–East view b) Ground floor plan, drawn in AutoCAD

In general, designing processes require considering all the facets of the building simultaneously. That is because whatever is done in a plan is generated in the design of any façade, section, or 3D view. As a result, the approach it forces to follow during the designing process resembles that of architects', who always take the project as an indivisible whole. Furthermore, modifications are almost always manual and time-consuming in AutoCAD, whereas any new adjustment in Revit will be incorporated into every single view, thus preventing the disruption of last-minute discrepancies. In AutoCAD, processes are quite "linear," involving a constant back and forth between all the parties [7]. Revit's advantage consists in the structural, mechanical, and electrical models being all linked to the main architectural model to detect and track any clashes between the elements in real-time. AutoCAD follows linear coordination involving a constant back and forth between all associated groups. On the other hand, Revit has an advantage as all models can be linked to the central architectural model, so as to keep track of real-time clashes between them.

2. Methods

The modelling is much faster in Revit, although working in AutoCAD is not an excessively complicated process. Modelling three-dimensional solid features begins with creating a two-dimensional sketch that defines a portion of the shape of parts. Sketching involves creating lines, arcs, circles, and dimensions, which resembles drawing in any CAD programme. In the 2D project, it is possible to create geometry in any sequence necessary. The 3D modelling sequence resembles the creation of a physical part, and the creation of one feature usually depends on the previous one. This feature hierarchy allows tracking the meaning of the geometry [8].

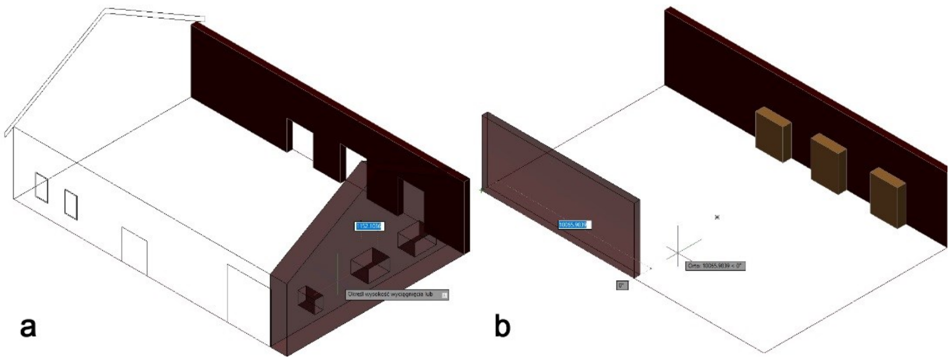

Fig. 3. Modelling three-dimensional solid features in AutoCAD a) with a two-dimensional sketch b) with polysolid command

The technique used for creating designing assemblies is known as the top-down design (or skeletal modelling) – Fig. 3a. The modelling process begins with sketches that represent a certain (or all) parts of the assembly. Individual parts of models are then created using geometries from a single sketch in the context of the assembly model. Assembly models may be also created using the bottom-up approach (Fig. 3b), in which previously modelled components are put together to represent the final assembly. When the assembly of components is complete, the traditional three-view drawing can be created. Both the effect of the drawing and modelling approaches result in a familiar engineering drawing [9]. In the 2D approach, the drawing captures the physical information needed to create the part.

In the solid modelling approach, the drawing is one of several uses for the created model.

The Revit and AutoCAD examples represent a completely different approach to designing. In the Autodesk's BIM environment, the work is based on ready-made 3D models grouped into families. This approach allows seamless placing multiple models in the workspace and setting connections between them. The formatting of elements within families is largely limited by their authors.

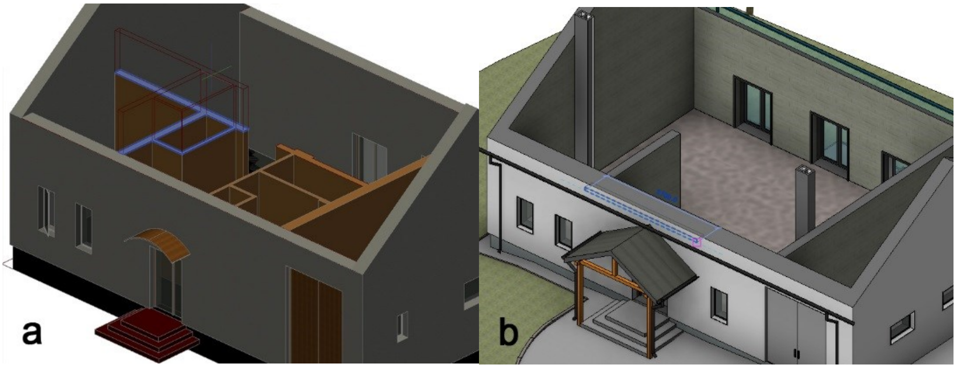

Fig. 4. Modelling walls - processes in Revit and AutoCAD

The portal is officially supported by Autodesk and contains 394,911 BIM objects from 1,414 producers. The number of resources is growing in response to the demand of manufacturers who require that their parts are modelled to become available for architects, contractors and installers representing various industries (who place them in projects, thus promoting their companies). However, each user of the Revit programme can model libraries with the use of available standard environment. Working with this programme starts by insertion of the axis and reference levels of the construction objects. Users select the type of plan from: structural plans, floor plans or ceiling plans (Fig. 5). At any time, it is possible to add additional axes and levels, which can be combined by parametric constraints with selected objects. By inserting additional family models, the designer selects the sizes, colours, textures, materials or layers. The user interface includes a feature inaccessible for AutoCAD – a project browser. It enables switching between plans, 3D views, elevations, sections, renderings, schedules, sheets, legends or families [11].

Each view is a drawing or a model, which can be independently modified in terms of dimensioning or view, and in addition preparing for printing from the sheets. However, the biggest advantage of working with this programme are dynamic changes, implemented in parallel in all drawings and models of a project. Regardless of the number of views a given project is divided into, the smallest change will be compiled in all elements, including statements, materials, schedules or detail views. This is the most , the invaluable feature of Revit for contractors who can modify the project in real time, by removing the created sections, prepare statements of materials and bill of quantity for subsequent parts of the works [12]. With Revit, site managers and investors can follow the progress and timeliness of construction. Other construction process stakeholders, including at later stages users or managers of construction facilities have access to the project. This is the reason, why BIM technology is often not only mentioned in the 3D aspect, but also 4D – scheduling, 5D - estimating, 6D - sustainability, or 7D – facility management applications [13].

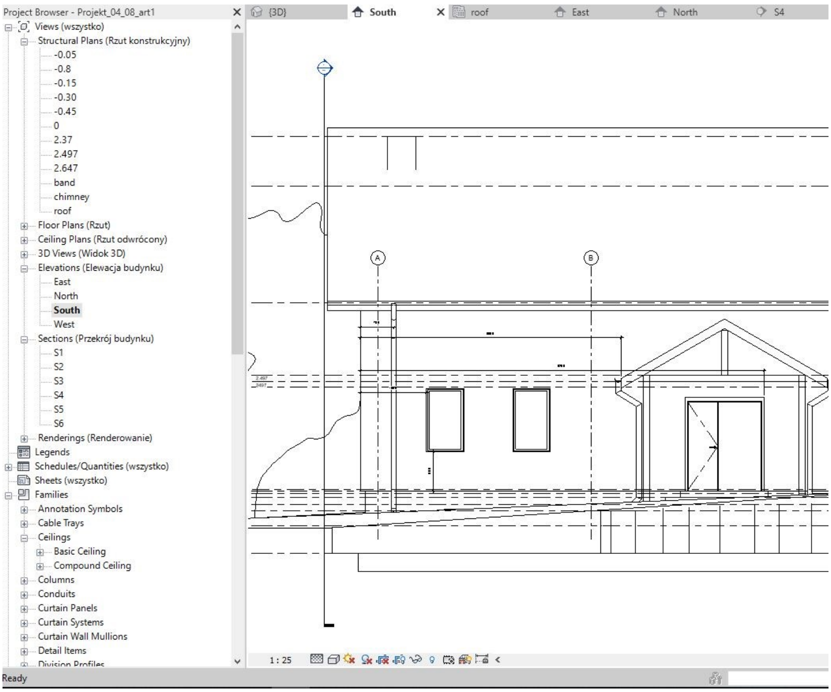

Fig. 5. Working with Revit project browser

3. Discussion of results

Based on the object model, Revit automatically creates (Fig. 6) plans, 3D views, elevations, sections, renderings, schedules, sheets, legends, families etc. Each change in a selected place triggers change in all others. Fig. 6 shows the views in the neighbouring windows of the programme: 6a – ground floor plan, 6b - section A-A, 6c - rendered 3D view, 6d - 3D view. The images show the process of modifying the driveway and the sidewalk around the building, which is a subordinate area of the terrain model. In the view of the neighbouring open windows, after selecting the terrain model in the ground floor plan, the remaining views are also edited. The terrain model is represented by highlighting purple lines. Even the slightest change in the shape of the envelope will be included in the whole project. The only exception is the view in Fig. 6c, which is a rendered 3D project and it is represented by a raster graphics image. Prior to rendering, the user can decide to export or save the image to a project, which will be available under the names saved in the project browser under Renderings. This is the next advantage of Revit over AutoCAD, as in the latter the rendered images may only be exported to external files.

Fig. 6. Working in 4 adjacent open windows in Revit (modifying the driveway and the sidewalk around the building)

Table 1 presents the material quantity prepared in Revit. The user decides about the data given in subsequent columns and rows of the table, most of which is imported from the family models, while e.g. descriptions and other information can be filled directly in the table. The table can be created from the ranges available in the tabs: fields, filter, sorting/grouping, formatting, appearance and it takes less than 1 minute. The programme provides tools that allow creating lists with material take-off properties in a considerably wide range, such as: assembly code, cost, description, family, level, manufacturer, model, type, mark, image, unit weight etc. In AutoCAD this process is much longer because, it is obligatory to introduce quantities by hand, which involves tedious creating and formatting the table, counting, dimensioning of inserted elements, and filling in the cells.

Source: Own work with Revit.With respect to AutoCAD, it can be extremely time-consuming to draw design details, which is why building material manufacturers share their drawings to simplify designers work and limit it to customising drawings. Given that the design templates rarely directly reflect the manufacturer's adopted solutions, each drawing requires a lot of time. It is possible to map such views based on a 3D model. However, it requires a designer to consider a very detailed approach to modelling at an early stage of the project, which may prove to be worthless in AutoCAD. In Revit, due to families of walls, windows, stairs, etc, which already contain detailed models, views of any detail are generated instantly and the depth or extent of their visibility can be modified at any time. This is another solution that can extremely speed up and facilitate the designer's work. Fig. 6a. presents a fragment of the part modelling section through the foundation substructure, flooring and wall in a shaded view, generated in 5 clicks in Revit.

Tab. 1. A section of material quantity in Revit

<MATERIAL QUANTITY>				
A	B	C	D	E
Category	Family and type	Amount	Material: Name	Material: Volume
Doors				
Doors	Drzwi_1S_wejsciowe2: 100x200	1	Szkło	0.00 m³
Doors	Drzwi_1S_wejsciowe2: 100x200	1	Domyślne okno	0.17 m³
Doors	Drzwi_1S_rama_drew: 80x200	1	Domyślne okno	0.08 m³
Doors	Drzwi_1S_rama_drew: 80x200	1	Domyślne okno	0.08 m³
Doors	Drzwi_2S_przeszklone: 140x200	1	Szkło	0.01 m³
Doors	Drzwi_2S_przeszklone: 140x200	1	Domyślne okno	0.14 m³
Doors	Drzwi_1S_rama_drew: 80x200	1	Domyślne okno	0.07 m³
Doors	Drzwi_1S_rama_drew: 80x200	1	Domyślne okno	0.07 m³
Doors	Drzwi_1S_rama_drew: 80x200	1	Domyślne okno	0.07 m³
		9		0.70 m³
Floors				
Floors	Floor: Strop z wylewką	1	Ocieplenie / bariery	5.94 m³
Floors	Floor: Strop z wylewką	1	Żelbet - wylewany	17.82 m³
Floors	Floor: Strop z wylewką	1	Beton - wylewka pia	5.94 m³
Floors	Floor: Żelbet 15 + Wylewka 5	1	Żelbet - wylewany	18.74 m³
Floors	Floor: Żelbet 15 + Wylewka 5	1	Beton - wylewka pia	6.25 m³
Floors	Floor: Żelbet 15 + Wylewka 5	1	Żelbet - wylewany	16.48 m³
Floors	Floor: Żelbet 15 + Wylewka 5	1	Beton - wylewka pia	5.49 m³
		7		76.67 m³
Furniture				
Furniture	Ławka_1: Ławka_1	1	Gus Modern Return	0.00 m³
Furniture	Ławka_1: Ławka_1	1	Gus Modern Return	0.06 m³
Furniture	Garden_Bench_6052: 6'	1	Drewno - brzoza	0.04 m³

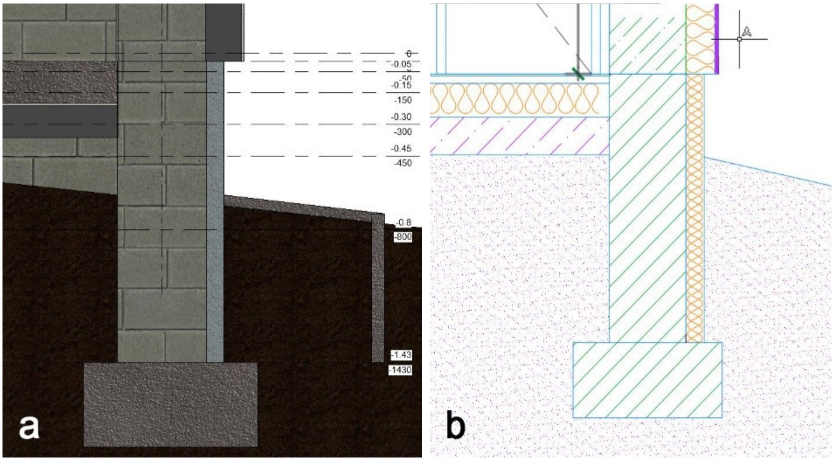

Fig. 8. Detail of building foundations made in a) Revit b) AutoCAD

In Revit environment, certain inconveniences were also encountered as in the case of certain functionalities, and two that are particularly problematic in Revit, AutoCAD proves easier in operation. The first aspect is the difficult user-programme communication. The Revit interface is not equipped with a command line, therefore, the knowledge of command functionality is required, even though the subsequent steps are displayed in the lower-left of the programme’s interface (Fig. 9a). The user must predict sequences of events, which to a certain extent requires memorising the programme sequences. In AutoCAD, each step of the user is monitored and described by the programme in the command line, from which the user can call further commands (Fig. 9b). The second advantage of AutoCAD is the ability to draw and configure simple, non-parameterised geometrical figures that can be modified with considerable freedom. The designer is thus not limited to imported available family models. Achieving a similar level of freedom in Revit environment requires expert knowledge of the interface and family methodology creation. In addition, making small changes to the drawings can be faster, however, the designer must remember to enter them in each drawing. As mentioned earlier, in Revit, a single chosen drawing or model view needs to be modified to take effect in other views.

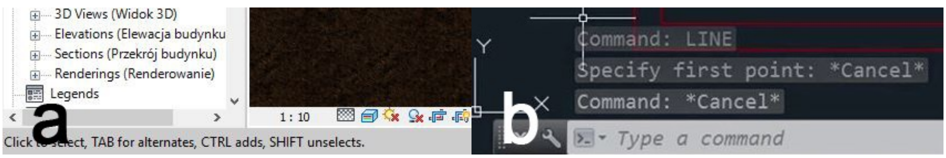

Fig. 9. The view of a communication module: a) Revit, b) AutoCAD

The simple building construction was selected as an example of civil structure design optimisation with a BIM application. In this case, the time spent on the project process is relatively short, and the time savings amounted 32 h, i.e. 31%. The time of preparation of 3 floor plans, 4 elevations, 2 sections and building a 3D model with terrain, the imposition of materials and textures were counted. The total working time for Revit was 73h, and for AutoCAD 105h. Dimensioning and preparation for printing were not included. Given the capabilities of Revit, in the case of larger projects, e.g. 250 h of AutoCAD, the time gain would save 77.5 h. Therefore, employing BIM brings measurable profits in the form of saved work hours and money.

In the reported analysis, default programme settings were used to enable the comparison and description of authoritative results. The presented example covers only the architectural industry, but it can be assumed that in other industries: construction, electricity or water and sewage supply, these profits can be even greater. In addition, in real conditions, the entire project would be supervised by a manager, ensuring that design conflicts and errors would be avoided.

4. Conclusions

Elimination of collisions, high accuracy of projects and extensive benefits of working with a parameterised building model are but a few features determining the increasing popularity of tools for working in BIM across industries. As demonstrated in the paper, the methodology of working with the programme is not intuitive and requires the designers previously working in the AutoCAD environment to reset their habits, e.g. regarding models for generating floor plans, elevations or sections being imported or modelled from object families.

The paper presents the results of a comparative analysis of building information modelling standard and working in the computer-aided design environment. Dynamically generated views allow instant modification and customisation of the entire project in real time. Working on a small building allowed indicating the full spectrum of benefits and advantages of BIM technology. The results show that application of the BIM standard can optimise the civil structure designing process, which is particularly beneficial with respect to: dynamic introduction of changes in all drawings and models, simplified process of generating material quantity, drawing construction details, shortening designing time. however, the BIM approach involves certain inconveniences at work compared to the AutoCAD programme, such as the lack of a command line and the inability to quickly draw simple geometric figures.

Although the scope of the works reported in the paper was limited to the modelling process for the architectural industry in BIM technology, the gains in work time amounted to 31%. In subsequent studies, authors will present research results into the possibilities of cooperation between designers from different industries, collision elimination and project management in the BIM environment. This area, even in commercial applications, is not widely implemented due to high knowledge requirements.

References

[1] B. Hardin, D. McCool, “BIM and construction management: proven tools, methods and workflows”, *John Wiley & Sons*: *Indianapolis*, 2015

[2] A. Makarewicz, S. Korga, W. Rosa, “The types of computer graphics and their application at different levels of knowledge”, *Advances in Science and Technology Research Journal.* vol. 9(28), pp. 149–152, 2015.

[3] J. Szulżyk-Cieplak, A. Duda, B. Sidor, “3D printers – new possibilities in education”, *Advances in Science and Technology Research Journal,* vol. 8(24), 96–101, 2014.

[4] A. Vysotskiy, S Makarov, J. Zolotova, E. Tuchkevich, “Features of BIM Implementation Using Autodesk Software”*, Procedia Engineering,* vol. 117*,* pp. 1143–1152, 2015.

[5] D. Kasznia, J. Magiera, P. Wierzowiecki, “BIM w praktyce : standardy, wdrożenie, case study”*, Wydawnictwo Naukowe PWN: Warszawa*, 2018.

[6] J. P. Carvalho, L. Bragança, R. Mateu, “Optimising building sustainability assessment using BIM”, *Automation in Construction,* vol. 102, pp. 170–182, 2019.

[7] A. Jaskulski, “AutoCAD 2019/LT2019/Web/Mobile+: kurs projektowania parametrycznego i nieparametrycznego 2D i 3D”, *Wydawnictwo Naukowe PWN: Warszawa*, 2019.

[8] J. Montusiewicz, K. Dziedzic, M. Barszcz, “Komputerowa grafika inżynierska: ćwiczenia do programu AutoCAD 2013. Cz. 1.”, *Wydawnictwo Politechniki Lubelskiej: Lublin*, 2013.

[9] J. Czepiel, “AutoCAD: ćwiczenia praktyczne 3D”, *Wydawnictwo Politechniki Śląskiej: Gliwice*, 2012.

[10] S. P. Zotkin, E. V. Ignatova, A. I. Zotkina, “The Organization of autodesk revit software interaction with applications for structural analysis”, *Procedia Engineering,* vol. 153, pp. 915–919, 2016

[11] A. Vysotskiy, S. Makarov, J. Zolotova, E. Tuchkevich, “Features of BIM Implementation Using Autodesk Software”*, Procedia Engineering*, vol. 117, pp. 1143–1152, 2015.

[12] K. Szajrych, J. Fijka, W. Kozłowski, “Revit Architecture. Podręcznik użytkownika”, *Helion: Gliwice*, 2010.

[13] P. Singh, A. Sadhu, “Multicomponent energy assessment of buildings using building information modelling”*, Sustainable Cities and Society*, vol. 49, 2010.

Małgorzata Plechawska-Wójcik[1], *Stanisław Skulimowski*[2], *Dawid Podstawka*[3], *Wojciech Plak*[4], *Patryk Piętal*[5]

ANALYSIS OF HUMAN PHYSIOLOGICAL REACTIONS IN VARIOUS CONDITIONS OF PSYCHOMOTOR ACTIVITY

Keywords: psychomotory activity, galvanic skin response, physical effort, pulse, anova test

Abstract

The aim of the work is to analyse human physiological reactions by using the authors' measurement system. The research was carried based on a procedure designed to consider various conditions of psychomotor activity, including short movie, a set of pictures, a live spider and cycling. The response of participants to individual stimuli was measured with the use of a measuring band with a set of appropriate sensors such as a galvanic reaction sensor, heart rate sensor, thermometer, and accelerometer.

The research described in the paper concerned emotions and reactions to phobias, stress, fear and physical effort. Analysing these reactions allows to better understand the relationship between content that is noticeable with the senses such as sight, hearing, physical effort and the specific reaction of the human body to these stimuli.

Research procedure covered specific test scenarios prepared to trigger specific reactions. Results show, that the most informative features were these selected from galvanic skin reaction sensor and heart rate sensor.

1. Introduction

For centuries, efforts have been made to better understand the structure and functioning of the human body. The measurement of psychophysical activity has been present in scientific research in various fields for many years. Given the technical limitations, it had been originally based on surveys and observations of the person examined. Nowadays however, the progress of technology and the emergence of innovative measurement techniques provide a broader view of the emotions experienced [2]. There is an extensive body of literature related to

[1] Lublin University of Technology, Institute of Computer Science, Nadbystrzycka 36B, 20-618 Lublin, Poland, m.plechawska@pollub.pl
[2] Lublin University of Technology, Institute of Computer Science, Nadbystrzycka 36B, 20-618 Lublin, Poland, s.skulimowski@pollub.pl
[3] Lublin University of Technology, Institute of Computer Science, Nadbystrzycka 36B, 20-618 Lublin, Poland, podstawka.dawid@gmail.com
[4] Lublin University of Technology, Institute of Computer Science, Nadbystrzycka 36B, 20-618 Lublin, Poland, kalpw@wp.pl
[5] Lublin University of Technology, Institute of Computer Science, Nadbystrzycka 36B, 20-618 Lublin, Poland, logun@o2.pl

emotion modelling [1] [3]. In their work [3] Chandler and Cornes overview biometric techniques applicable in measuring emotions, including: fingerprints, iris and facial recognition, skin conductivity (GSR) and facial thermography. So far, the developed measurement techniques are but partially successful and the question remains which of them can provide the most useful information for a respondent's survey, ensuring the least possible interaction with the user, while at the same time measuring a matter as esoteric as emotions [1]. A different analysis [4] focused on analysing the application of electrocardiogram as a tool for clinical diagnosis. The authors present a new approach to ECG data analysis based on autocorrelation (AC) and discrete cosine transform (DCT). The study, conducted on two sets of public databases, shows that ECG data might be successfully applied to monitor psychomotor activity.

In the literature ECG is widely applied in research on human physiological reactions. It is used to detect stress [5] or investigate pain-related characteristics [6]. It is also popular in cognitive workload analysis [7 8].

ECG was also proved to be useful as a new biometric modality for the recognition of human identity [9 10 11].

Physical activity testing is becoming an increasingly visible and common research tool, nevertheless, the effort of measurement is often hampered by the challenge of using relevant, reliable measures that also fit into a given research project. The assessment of motor activity is a multidimensional construct and, therefore, there is no measure that can evaluate all aspects of an activity. Researchers need to approach the choice of activity measurement with a clear concept of what type of data they intend to collect [12]. Another paper [13] discusses the benefits of physical activity monitoring and presents the overview of physical activity measuring techniques including traditional self-report questionnaires and direct observation as well as methods based on different devices such as accelerometers, pedometers, heart-rate monitors and armbands. What is more, the paper discusses the quality of physical activity measurement depending on such factors as age, gender, body weight or psychiatric and medical co-morbidities of responders.

2. Research

The research hypothesis put forward in the study reported in this paper is: It is possible to construct a low-cost intelligent armband, tracking the human body in various conditions of psychomotor activity.

2.1. Research parameters

In order to determine the research parameters for the examination of the psychomotor activity of the human body, authors used the scientific field of psychophysiology, which deals with the study of mutual relationships between the physiological and psychological domain. It focuses on the study of relationships between emotions, behavioural patterns in relation to brain function and changes in consciousness [14]. From the point of view of the psychophysiology of an organism, the following parameters were used to analyse the physiological reactions of a human being in various conditions of psychomotor activity:

1. galvanic skin reaction (GSR) - a measure of changes in the electrical resistance of the skin, which depends on the degree of its hydration mostly caused by the activity of sweat glands controlled by the sympathetic system. The examination of the galvanic reaction of the skin enables tracking: the emotions experienced, the degree of loss of mineral components, spontaneous reactions of the body [15, 16].
2. heart function - a measure of heart rate with the ECG (electrocardiography). It is a graphical representation of the electrical activity of the heart muscle. ECG measurement allows to: supervise the work of the human body, diagnose diseases of the human body, determine the efficiency of the body during an exercise test, examine the accompanying emotions and detect spontaneous reactions of the body [17].
3. body vibrations - this is possible based on the analysis of two variables: (1) an acceleration of the body, determined by means of an accelerometer, whose task is to measure linear and angular acceleration, and (2) an angular position determined by means of a gyroscope - based on the principle of momentum preservation by measuring the angular velocities of an object rotating around one of the axes: X, Y, Z. In our study, the focus is on measuring body vibration because of the complexity of measuring physical activity [18], the purpose of research, and the conditions for conducting experiments.
4. skin temperature [19] - human skin surface temperature is one of the basic terms used in thermodynamics and is defined as a state of thermodynamic equilibrium. Measuring the temperature of the human body under the influence of the external environment allows us to see reactions to stimuli such as stress and fear, during which an increase in the temperature of the human body surface is expected [20].

2.2. Description of the system

The main aim of the study was to determine the objective physiological response in different psychomotor conditions. The use of the authors' measuring system ensured objectivity in the form of a personal survey and relies only on the individual reactions of respondents concerning their sensations. This measuring system consists of (1) a wristband (figure 1A) with a built-in system and (2) a desktop application.

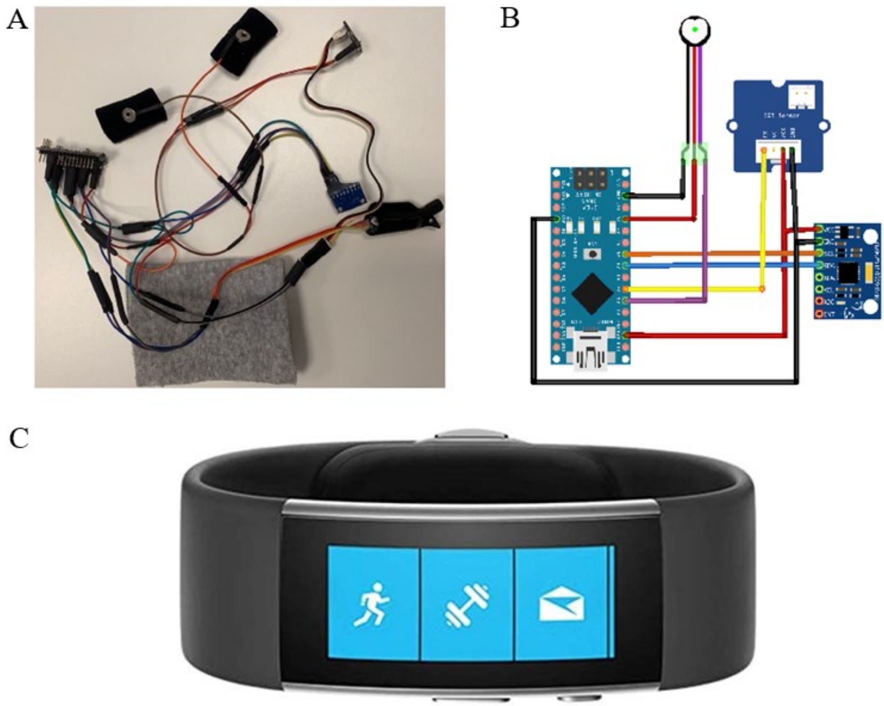

Fig. 1. Measuring Systems: Measuring Band (A), Wiring Diagram of Measuring Band (B), Microsoft Band 2 (C)

The wristband consists of:

- Arduino Nano used as the main control unit is a platform based on the ATmega168 microcontroller, clocked at 16 MHz, with built-in support for both analogue and digital input/output circuits.
- The MPU6050 accelerometer with a built-in temperature sensor and gyroscope for recording of movement and temperature data. It is connected to the microcontroller via a bidirectional TWI (Two Wire Interface) bus. The sensor is attached by connecting the analogue port 4 with the data line, the analogue port 5 with the clock line, and the 3.3 V power supply from the microcontroller with the sensor [14].
- The Galvanic Reaction Sensor manufactured by Seeed Studio is powered by 3.3V via the analogue port 2 and the power supply from the microcontroller. It uses two electrodes - attached to the heart and middle finger - measuring skin conductivity in the form of voltage.
- The heart rate sensor in the form of the clip to the index finger.

All wristband components connections are shown in figure 1.B The GSR readout is expressed as an Om (Ohm) resistance unit.

The application connects with the wristband and saves the measurements to the database while creating a live graph of the read data.

In order to compare and verify the results obtained, the authors used the Microsoft Band 2 (figure 1.C) - a commercial product reading similar parameters such as: pulse, galvanic reaction, location of the body or its temperature. It was chosen because of the authors' earlier experience with this device in the area of conducting scientific research involving the measurement of physiological functions [21]. GSR measurement was expressed as a unit of mV (skin tone). Both in the case of the original measurement system and the Microsoft Band 2 band, the pulse reading was expressed in BPM unit (beats per minute).

2.3. Research scenarios

In order to trigger specific reactions, special test scenarios had been developed. The first one was a prepared family cartoon, during which the respondent was unexpectedly interrupted by the graphics depicting a horror movie character and a loud scream (figure 2). The first part of the cartoon was calm and neutral. This type of film allowed us to examine the so-called background of a given respondent, i.e. to conduct a study of the reaction of the organism in a calm and natural environment. Pop-out graphics with sound allowed us to examine the reaction to stress and fear.

Fig. 2. A shot from a fairy tale and a shot depicting a scene with a "negative emotional charge"

In the second part of the experiment, the participants were presented with a series of photos. The series contained:

- images commonly considered relaxing (figure 3),
- images described as drastic,
- images similar in content to the first series, allowing for calming and relaxing.

Images used in the research were taken from the IAPS database [22].

This purpose of the slide show was to examine the difference in the reception of content that evokes different emotions on the psychomotor level.

Fig. 3. Composition of four "pleasant" photos

An additional stimulus used in this part of the study was to place a terrarium with a live *Brachypelma vagans* spider in front of the tested person (figure 4). The spider was shown after the last series of photos was displayed. During the presentation, information about the toxicity of its venom and aggressiveness was given to the participant. Subsequently, the respondent was encouraged to take the spider in hand. In order to intensify the emotions, the respondent was informed about the way in which the spider attacks and the consequences related to it. In the end, the terrarium was never opened during the research; after all, the aim of the experiment was not the reaction to the touch but the very sight of the spider.

Fig. 4. Spider Brachypelma vagans

The third part of the experiment consisted in examining the reaction of the human body to physical effort in the form of cycling while listening to music and without external stimuli (figure 5). For this purpose, the study was conducted twice on each of the following of respondents with a break of at least 48 hours to eliminate the impact of the first attempt.

Fig. 5. Selected respondents during cycling

Two series of measurements were carried out, covering the same factors except for one - without and with music. The other factors were identical: the same duration of the effort of 5 minutes. This time it was divided into five periods. The 5-minute duration of the study was divided into 5 periods:

- the respondent had to maintain a constant speed of 6 km/h for 90 seconds,
- maintaining a constant speed of 15 km/h for 120 seconds,
- reducing the speed to the initial 6 km/h in 60 seconds
- acceleration of the test to the maximum speed that can be achieved by the tester and holding it for 15 seconds,
- gradual decrease in the speed until a complete stop in 15 seconds.

2.4. Research group

The research was conducted on people of similar ages between 22 and 25 years old. The number of examined persons was 15. The subjects were 5 women and 10 men. In addition, as the experiment with the film was characterised by the greatest ease of measurement and its results believed to be the most promising, in this case, 10 additional subjects were put to test, 3 women and 7 men respectively.

The study was carried out on respondents who considered themselves to be inherently frightened, and those who considered themselves to be difficult to frighten. Moreover, the study group included both people terrified of spiders and those who own or used to own spiders.

2.5. Conduct of the study

During the early attempts at the experiment, the heart response sensor was located at the wrist with other sensors, but as it emerged, the clip to the index finger effectively extended the range of values read by the sensor, thus providing greater accuracy.

During the development of the results, the main emphasis was put on the analysis of GSR sensor readings. The GSR readings were combined with heart rate readings. The latency was determined by comparing the results with GSR and accelerometer readings. The GSR values read with a specially-designed measuring system were compared with the values obtained from Microsoft Band 2. In a similar way, the heart rate read with the Microsoft band was compared with the heart rate calculated with the readings obtained with the authors' measuring system. The temperature readings served as an additional parameter and were not taken into account. The measurement readings were carried out at a frequency of 49 Hz. In this way, the data processed were subjected to statistical analysis and statistical tests.

During the analysis of the results for particular research scenarios, detailed values were not given because for the analysis of the research aimed to specify the trends among the examined persons, rather than to analyse the changes in individual values.

3. Test results

The process of developing the measurements was divided into four sections, which described a case of a selected person for a research scenario based on a film with a scene with a negative emotional charge and a summary of the results of all respondents for each scenario.

3.1. Summary of GSR waveforms

Below (figure 6) a list of sensor readings is presented: GSR, thermometer and accelerometer on one chart for the research scenario of a film with a scene with a negative emotional charge.

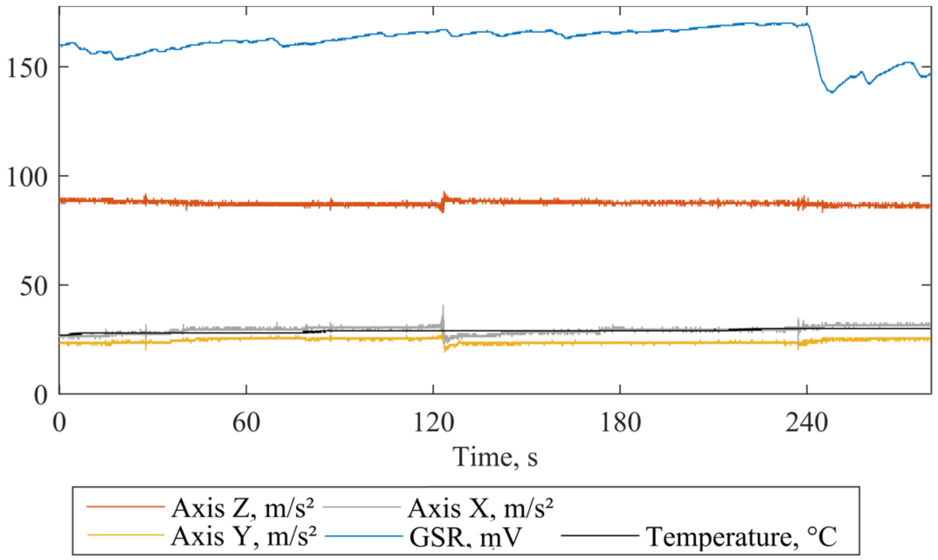

Fig. 6. Summary of GSR waveforms, temperature and accelerometer for the selected test subject

For most of the measurement time, the graphs were stable. However, special attention should be paid to the relationship between accelerometer readings and GSR sensor measurements. On 240 seconds of the measurement there was a scene with a negative emotional charge in the film, which caused a movement of the respondent's hand, which was noted on the accelerometer chart. Immediately after the recorded hand movement, there was a sharp drop in GSR readings. In this way, at the further stage of the development of the results, latencies for stimuli were determined.

3.2. Summary of heart rate measurement

The course of heart rate readings was determined using the Gauss function. Below (figure 7) the approximation of the heart rate for the collected measurements is presented. The black dot indicates the average heart rate at the time of recording the heartbeat, while the blue line shows the heart rate waveform adjusted by the Gauss function.

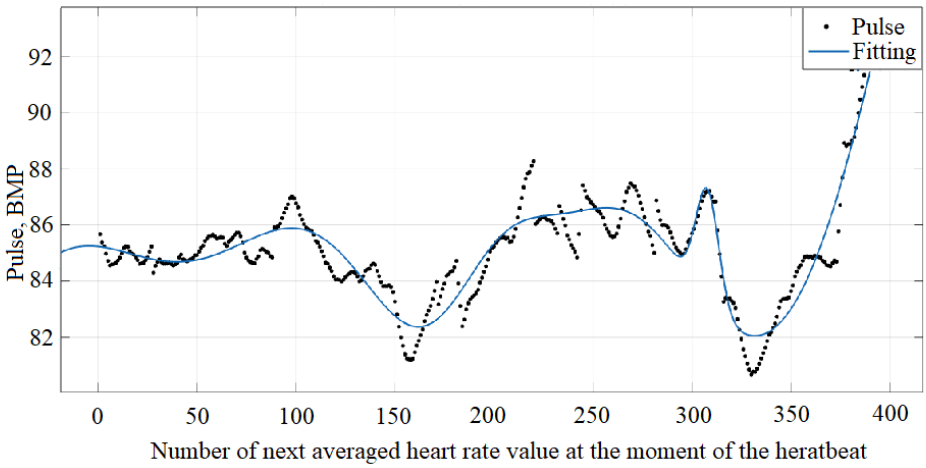

Fig. 7. Summary of heart rate measurement and heart rate adjustment

The presented fragment of the diagram (figure 7) shows a sudden drop and then an increase in heart rate, which indicates an external stimulus, which was a scene with a negative emotional charge in the film.

3.3. Comparison of results from the authors' measurement system and Microsoft Band 2

In the first section, the heart rate and GSR readings from the authors' measurement system were compared with those from Microsoft Band 2 (figure 8).

In the course of the test, clear and extensive disproportions in the values of readings are noticeable, but the course of the variability of graphs overlaps, which is marked on the distance from 240th second to the end of the graphs. This proves the correctness of the implementation of the heart rate monitor in the authors' measurement system.

GSR charts of the authors' measurement system and Microsoft Band 2 (figure 9) are characterised by different waveforms. In the case of the authors' measurement system, an increase in the value in time is noticeable, while for Microsoft Band 2 a decrease in the value in time was noted. Apparently, measurement disproportions may have been caused by a different location of the sensors. In the case of our measuring system, the GSR sensor was placed on the fingers, while the Microsoft Band 2 wristband was placed on the wrist of the same hand. In addition, the authors' measuring system analyses the conductivity of the skin while Microsoft Band 2 measures the skin resistance. In both analysed cases, however, there is a sudden breakdown of the diagrams immediately after 240th second, which proves the occurrence of an external stimulus. The antagonistic character of the graphs and the observed reaction at the same time to the scene of a negative emotional charge in the film testify to the correct implementation of the GSR sensor in the authors' measurement system.

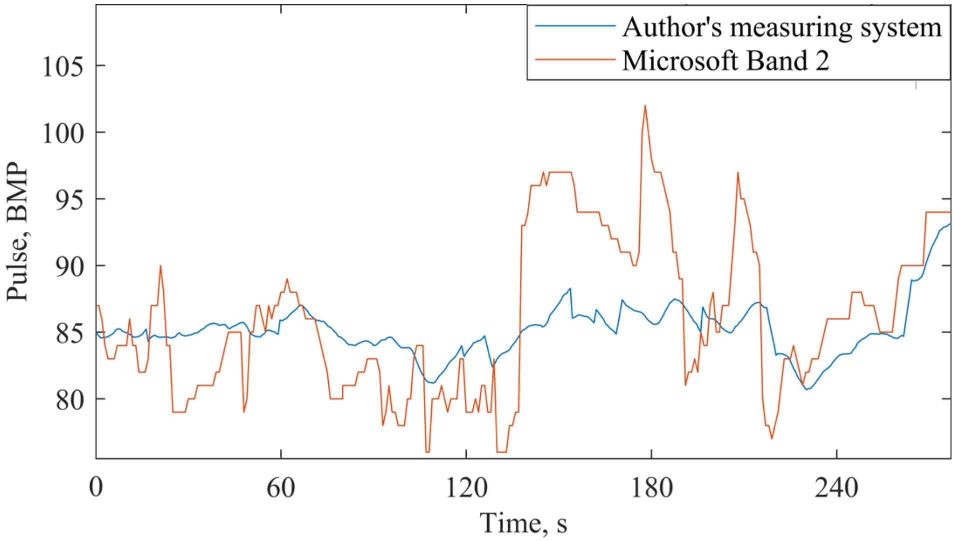

Fig. 8. Summary of the pulse rate for the authors' measurement system and Microsoft Band 2

The graphs show Ohm and mV units respectively. While Microsoft Band 2 operates with the Ohm unit, The authors' measurement system examines this parameter by expressing its value in the mV unit. It is caused by the fact that the GSR sensor used in the authors' measurement system is connected to the Arduino Nano microcontroller which can return values only in V.

During the analysis of the next section, on the basis of the received data, correlation coefficients were calculated to verify the relationships between the measuring systems. Due to the highest number of examined subjects, the most reliable results were obtained in the scenario of a film with a scene containing a negative emotional charge. In other cases, the correlations do not show clear results, most likely due to the insufficiency of data, stemming from difficulties in reading some of it from the Microsoft Band 2 wristband. Moreover, disproportions in the results of the differences in correlation could be caused not only by the same reading but also by the conditions of readings, which include the time of the study.

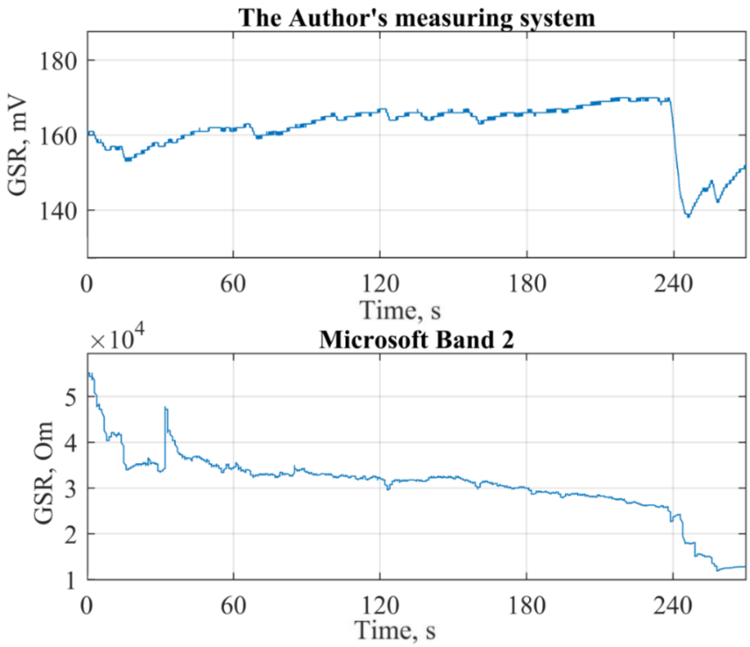

Fig. 9. Summary of the GSR readings of the authors' measurement system with Microsoft Band 2

Using the Student's t-test, the results of mean heart rate and GSR values before and after the occurrence of the stimulus between the measurement systems were compared, producing information regarding the absence of statistically significant differences. Because statistically there were no differences in the results between measurement systems, it proves the correct implementation of the authors' measurement system.

In order to statistically analyse the results obtained for the first section of the research, the Student's t-test was performed for a set of pairs of comparative data.

3.4. Results of ANOVA test

For the remaining sections, the statistical test of ANOVA was used to examine the relationship between the mean heart rate and GSR values for particular scenarios. The results between the bands were also compared. Similarly to the Student's t-test, the results showed that the differences are not statistically significant.

In other cases, the ANOVA method was used because of the higher number of comparative data after 4, 8, 16 series, respectively.

The diagram in figure 10 shows that for each series the median remains at a similar level. Series 3 and 4 are characterised by much larger measurement fluctuations compared to series 1 and 2. The largest measurement range is found in series 4.

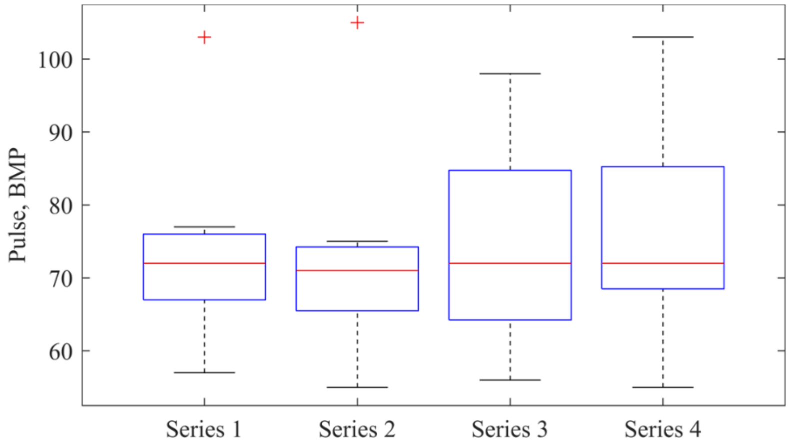

Fig. 10. Average heart rate values in consecutive measurement series for the authors' measuring system

Analysing the graph in figure 11, it can be observed that for the first three series the median remains at a similar level, whereas for the fourth series the value of the middle interval decreased. Series 1 and 2 are characterised by much greater measurement fluctuations in relation to series 3 and 4.

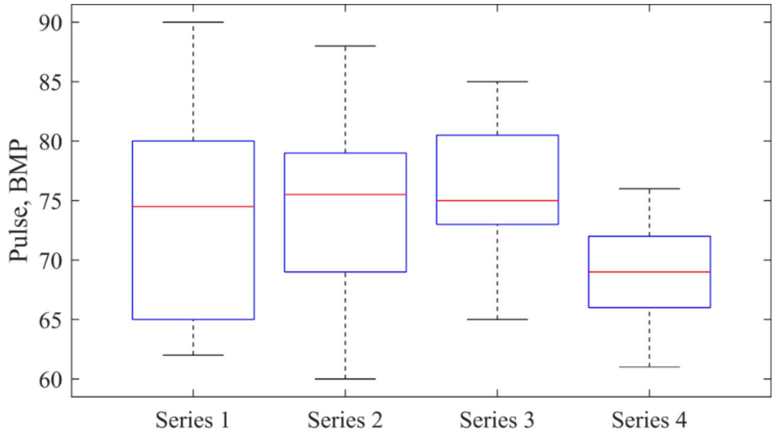

Fig. 11. Average heart rate values in the consecutive measurement series for Microsoft Band 2

The diagram in figure 12 shows that in each of the series for cycling effort the median remains at a similar level. Moreover, measurement ranges in most series are maintained at a similar level except for series 3 and 4, larger measurement ranges are visible.

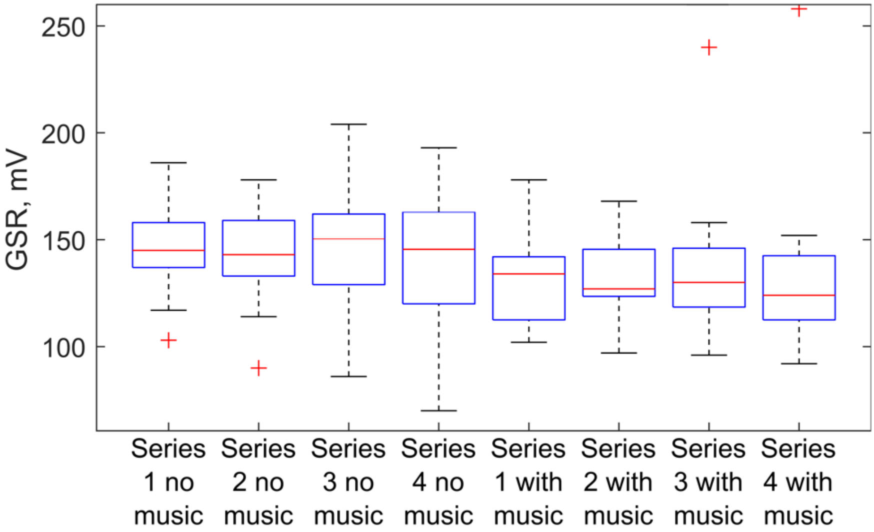

Fig. 12. Average GSR values in subsequent measurement series for the authors' measurement system

Fig. 13 shows a comparison of the average GSR values of the subsequent cycling effort series with music and without an external stimulus for the Microsoft Band 2.

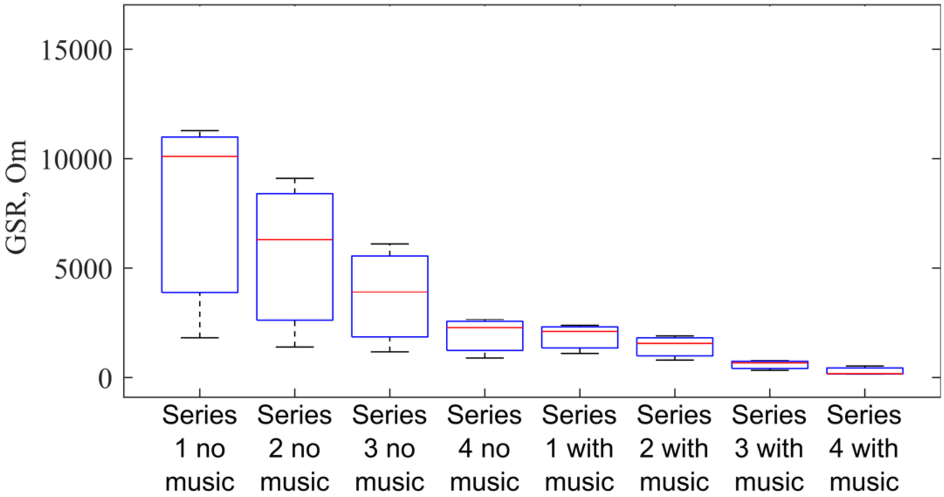

Fig. 13. Average GSR values in the following series of measurements for Microsoft Band 2

The chart (figure 13) shows a clear downward trend. With each subsequent series the median value decreases. In addition, for each subsequent series the measuring range is reduced.

4. Conclusions

The statistical research showed that in most cases the differences in each of the test series for both measuring systems are not statistically significant. A notable statistical difference occurs only in the case of comparison of GSR measurement before and after the stimulus for the film and the bike with music. The detected differences are visible and, on the basis of organoleptic assessment, it is possible to determine the moment of the stimulus occurrence and the change of the body's reaction to the stimulus. Unfortunately, from the point of view of statistics, they size of data is too small to be statistically significant. The correlation coefficients determined that due to a larger number of conducted studies, the most important coefficients were obtained in the case of a film scenario with a negative emotional charge. In other cases, the results proved to be inconclusive.

It was observed and proved that the location of the heart rate sensor is critical for the correctness of the reading. In the original version of our measurement system, the sensor was placed on the wrist. However, during the examination, it was revealed that more readable readings were obtained by placing the sensor on the fingertip.

Comparing the results between the measuring systems by the statistical methods, it emerges that in almost no case are there any statistically significant differences, which proves the correctness of the implementation of the authors' measuring system. The results from the statistics suggest that the system is at least as accurate as Microsoft Band 2 in terms of the parameters tested; nevertheless, neither system is sufficient to examine the statistically significant difference in all the tested cases. The research proved that it is possible to construct an intelligent band at a low cost, which allows tracking the human body in various conditions of psychomotor activity, which therefore proved the validity of the hypothesis.

However, there is a need to carry out further testing on a larger research group in order to highlight individual differences. On selected respondents the effects of the applied stimuli are visible, nevertheless, in most cases, it turned out to be insufficient to show statistically significant differences.

Acknowledgement

Drastic images have been removed from the article because of the possible negative impact on sensitive readers.

References

[1] Mauss, I.B., Robinson, M. D., "Measures of emotion: A review", *Cogn Emot*, 23(2), pp. 209–237, 2009, doi number: 10.1080/02699930802204677

[2] A. F. Bobick, A. Y. Johnson, "Gait Recognition Using Static, Activity-Specific Parameters", *Proceedings of the 2001 IEEE Computer Society Conference on Computer Vision and Pattern Recognition, IEEE*, pp. 423–430, 2001, doi number: 10.1109/CVPR.2001.990506

[3] C. Chandler, R. Cornes, "Biometric Measurement of Human Emotions", *Proceedings of Conference: Asia Pacific Institute of Information Technology*, pp. 164–168, 2011.

[4] Y. Wang, F. Agrafioti, D. Hatzinakos, K. N. Plataniotis, "Analysis of Human Electrocardiogram for Biometric Recognition. Hindawi Publishing Corporation EURASIP, *Journal on Advances in Signal Processing*, 2007, doi number: 10.1155/2008/148658

[5] I. Mohino-Herranz, R. Gil-Pita, J. Ferreira, M. Rosa-Zurera, F. Seoane, "Assessment of mental, emotional and physical stress through analysis of physiological signals using smartphones", *Sensors*, vol. 15(10), pp. 25607–25627.

[6] Y. Chu, X. Zhao, J. Han, Y. Su, "Physiological signal-based method for measurement of pain intensity", *Frontiers in neuroscience*, vol. 11, 279, 2017.

[7] E. Haapalainen, S. Kim, J. F. Forlizzi, A. K. Dey, "Psycho-physiological measures for assessing cognitive load", *In Proceedings of the 12th ACM international conference on Ubiquitous computing* , pp. 301–310, ACM, 2010.

[8] R. Matthews, N. J. McDonald, P. Hervieux, P. J. Turner, M. A. Steindorf, "A wearable physiological sensor suite for unobtrusive monitoring of physiological and cognitive state", *In 2007 29th Annual International Conference of the IEEE Engineering in Medicine and Biology Society* , pp. 5276–5281, IEEE, 2007.

[9] L. Biel, O. Pettersson, L. Philipson, P. Wide "ECG analysis: a new approach in human identification", *IEEE Transactions on Instrumentation and Measurement*, vol. 50, no. 3, pp. 808– 812, 2001.

[10] J. M. Irvine, B. K. Wiederhold, L. W. Gavshon, S. A. Israel, S. B. McGehee, R. Meyer, M. D. Wiederhold, "Heart rate variability: a new biometric for human identification", *Proceedings of the International Conference on Artificial Intelligence (IC-AI '01)*, pp. 1106–1111, Las Vegas, Nev, USA, June 2001.

[11] S. A. Israel, J. M. Irvine, A. Cheng, M. D. Wiederhold, B. K. Wiederhold, "ECG to identify individuals", Pattern recognition,vol. 38(1), pp. 133-142, 2005.

[12] F.W.cBooth, M. V. Chakravarthy, E. E. Spangenburg, "Exercise and gene expression: physiological regulation of the human genome through physical activity", *The Journal of Physiology*, vol. 543(Pt 2), pp. 399–411, 2002, doi number: 10.1113/jphysiol.2002.019265

[13] L. G. Sylvia, E. E. Bernstein, J. L. Hubbard, L. Keating, E. J. Anderson, "Practical Guide to Measuring Physical Activity", *Journal of the Academy of Nutrition and Dietetics*, vol. 114, no. 2, pp. 199–208, 2014, doi number: 10.1016/j.jand.2013.09.018

[14] E. S. Epel, A. D. Crosswell, S. Mayer, A. A. Prather, G. Slavich, E. Puterman, W. B. Mendes, "More than a feeling: A unified view of stress measurement for population

science. Frontiers in Neuroendocrinology", *Elsevier*, vol. 49, pp. 146–169, 2018, doi number: 10.1016/j.yfrne.2018.03.001

[15] M. Sharma, S. Kacker, M. Sharman, "A Brief Introduction and Review on Galvanic Skin Response. International Journal of Medical Research Professionals", *Ibn Sina Academy of Medieval Medicine & Sciences*, vol. 2, no. 6, pp. 13–17, 2016, doi number: 10.21276/ijmrp

[16] W. Boucsein, "Electrodermal Activity", *Springer Science & Business Media*, New Jork, 2012.

[17] K. A. Nixon, V. Aimale, R. K. Rowe, "Spoof Detection Schemes, Handbook of Biometrics", *Springer*, pp. 403–423, 2008, doi number: 10.1007/978-0-387-71041-9_20.

[18] F. W. Booth, M. V. Chakravarthy, E. E. Spangenburg, "Exercise and gene expression: physiological regulation of the human genome through physical activity", *The Journal of Physiology*, 543(Pt 2), pp. 399–411, 2002, doi number: 10.1113/jphysiol.2002.019265.

[19] B. R. Shmaefsky, "Anatomy & Physiology: A Case Study Approach", *USA, Emc Pub*., 2007.

[20] R. A. Carlstedt, M. Balconi, "Handbook of Sport Neuroscience and Psychophysiology", *Routledge,* 2018.

[21] S. Skulimowski, M. Badurowicz, "Wearable sensors as feedback method in virtual reality anti-stress therapy", *2017 International Conference on Electromagnetic Devices and Processes in Environment Protection with Seminar Applications of Superconductors (ELMECO & AoS), IEEE*, 2018, doi number: 10.1109/ELMECO.2017.8267716.

[22] P. J. Lang, M. M. Bradley, B. N. Cuthbert, "International affective picture system (IAPS): Affective ratings of pictures and instruction manual", *Technical Report A-8. University of Florida*, Gainesville, FL, 2008.

Naqibullah Daneshjo[1], Jana Naščáková[2], Erika Dudáš Pajerská[3]

METHODOLOGICAL PROCEDURES APPLIED TO MANUFACTURING SYSTEMS DESIGN

Keywords: manufacturing systems, design, implementation, production

Abstract

Designing manufacturing processes and systems is a complex multi-level system influenced by a large number of factors. Designing requires deep analysis of targets, ways of preparing and implementing complex and robust manufacturing systems, assessing the impact of important factors, and integrating the knowledge of many branches of science and individual divisions. The target of each design is to optimally reduce design processes while keeping the required quality and minimising costs.

1. Introduction

Project tasks of designing new production can be successfully managed only by consistently applying the CAx systems throughout the project design solution chain, all the way to their practical implementation. Various modelling techniques and tools and optimisation and simulation theories are used. The aim is to improve the concept of the final model prior to implementation. In addition to general project methodologies, special approaches to innovating the CIM-type systems, flexible production, customer-oriented production, etc. are currently under development.

The role of the virtual stage of designing is to determine the basic structural elements of the system, their relations and functions, which corresponds in empirical methodologies with the so-called conceptual solution (designing). The structural design stage addresses detailed system specifications up to the level of project documentation.

Higher innovation targets, presented by modern production technologies and production systems, put high demands on design preparation. These demands can be satisfied only by adequate development of design activities and their organisation into productive information and knowledge systems ensuring design

[1] University of Economics in Bratislava, Faculty of Business Economics with seat in Košice, Department of Commercial Entrepreneurship, naqibullah.daneshjo@euke.sk
[2] University of Economics in Bratislava, Faculty of Business Economics with seat in Košice, Department of Commercial Entrepreneurship, jana.nascakova@euke.sk
[3] University of Economics in Bratislava, Faculty of Business Economics with seat in Košice, Department of Commercial Entrepreneurship, erika.dudas.pajerska@euke.sk

quality. Designing modern facilities of mechanical engineering production based on the principles of customer manufacturing is currently affected by the development of the market dynamics in all areas. The success of modern strategies of engineering production is based on the application of new approaches and design methods. Project tasks of designing new production can be successfully managed only by consistently applying the CAx systems throughout the project design solution chain all the way to their practical implementation. Various modelling techniques and tools and optimisation and simulation theories are employed [9, 12]. The aim is to improve the real concept of the final model before its implementation. In addition to general project methodologies, special approaches to innovating the CIM-type systems, flexible production, customer-oriented production, etc. are currently under development. From the computer support point of view, the greatest progress has been made in these modern methodological aspects of production design.

2. Production system model and methodological procedures of designing

The structure of production systems includes technological, handling and control subsystems. Their versatility, flexibility and other parameters of the internal structure enable their technological customisation as required to fit virtually any scenario. Production systems can be defined by potential functions with respect to the implementation of technological processing, handling of object of productions, tools and preparations, and information processing functions. At the same time, specific technical subsystems and mutually interacting changes in these subsystems can be defined as $V_{(S)}$ models, based strictly on the general theory of systems, which often poses problems with interpretation. Therefore, it is more efficient to start from a narrowed theory of technical systems [2, 3].

The system definition $V_{(S)}$ is based on the theory of technical systems and the system of understanding the production processes. The core positions of the model stem from the solutions published in the original papers. The compositional model $V_{(S)}$ /1/ and the system characteristics have been defined with ($V_{(S)}$) / 2 / as follows:

Tab. 1. The compositional model and system characteristics [10, 14]

<table>
<tr><td>$V_{(S)} = \langle O, T, \Omega \rangle$ /1/</td><td>$s\,(V_{(S)}) = \langle C, F, S \rangle$, /2/</td></tr>
<tr><td>$O = \{O1, O2, . , Oa\}$
$T = \{T1, T2, . , Tb\}$
$\Omega = \{\Omega_1, \Omega_2, . , \Omega_c\}$</td><td>$C = \{C1, C2, □ Cd\}$
$F = \{F1, F2, □ , Fe\}$,
$Ci = \{Cis\ Cis\ Cit\}$ ∪ ∪</td></tr>
<tr><td colspan="2">O − set of operands Oi (object of productions) in $V_{(S)}$ on which the required transformations are performed (transformation of the semi-finished into a finished product)</td></tr>
<tr><td colspan="2">T – a set of Tj operators executing transformations on operands (active elements of the production system ensuring changes in shape, properties,</td></tr>
</table>

position, composition, etc.) and activities complementary to these changes (information processing, storage, etc.),
Ω set of transformation processes Ω_k running in the $V_{(S)}$ – (technological, handling, control and other processes)
C set of targets for which $V_{(S)}$ is created
F – set of behaviours, or of the manners of functional activity $V_{(S)}$
S – structure $V_{(S)}$ expressed by the set of internal links

3. The production system creation methodology

Modern designing has to adapt quickly to changing requirements for continuous product innovation, manageable variety of variants, meeting unpredictable customer requirements, reduced product lifecycle, responding to significant sales fluctuations, etc. Preparing the production system for possible changes is no longer economically viable. The main principle of production systems adaptability is the capability to allow for rapid revision of organisation and technology at low investment costs [4, 13, 15].

The system procedure for creating production systems is illustrated in figure 1. The system is created in four stages:

1. Building a data and knowledge base needed for system creation and detailed analysis of the same.
2. Assembling a virtual model – system structure.
3. Assembling a structural model – detailed project documentation.
4. Implementation in real production premises.

In the model, the sequence of stages or sub-stages of the creation process is symbolically expressed as the feedback related to fine-tuning and changes to solution as a gradual reduction of the level of abstraction.

For the sequence of V(S) creation formulated in this way, the correspondence of the system model V(S) with the internal substages of virtual design V(S) can be expressed as follows:

a) Entities $0i \in V(S)$ and entities $Ci \in s(V(S))$ correspond to the design stage of goal determination or selecting an object of production. Upon deeper analysis, questions may arise about the internal priorities between setting objectives and selecting objects of production. In conceptual applications, the starting goals are considered those that are the springboard for modernisation of the existing production – the object of production. System approach operates with the dualism of both entities.
b) Entities $\Omega j \in V(S)$ and $Fj \in s(V(S))$ correspond to the stage of designing operations and operating procedures of manufacturing systems. This aspect is fully compliant with the theory of production processes.
c) Entities $Tj \in V(S)$ and $Sg \in s(V(S))$ correspond to project activities of selecting production equipment, determining spatial layout, and so on.

These relationships create a framework according to which various partial design methods V(S) can be integrated into the system concept and, at the same time, they uncover areas unaccounted for, covered by intuitive procedures in designing [5, 16].
The role of the virtual stage of designing is to determine the basic structural elements of the system, their relations and functions, which is known in empirical methodologies as the conceptual solution (designing). The structural design stage addresses detailed system specifications up to the level of project documentation.

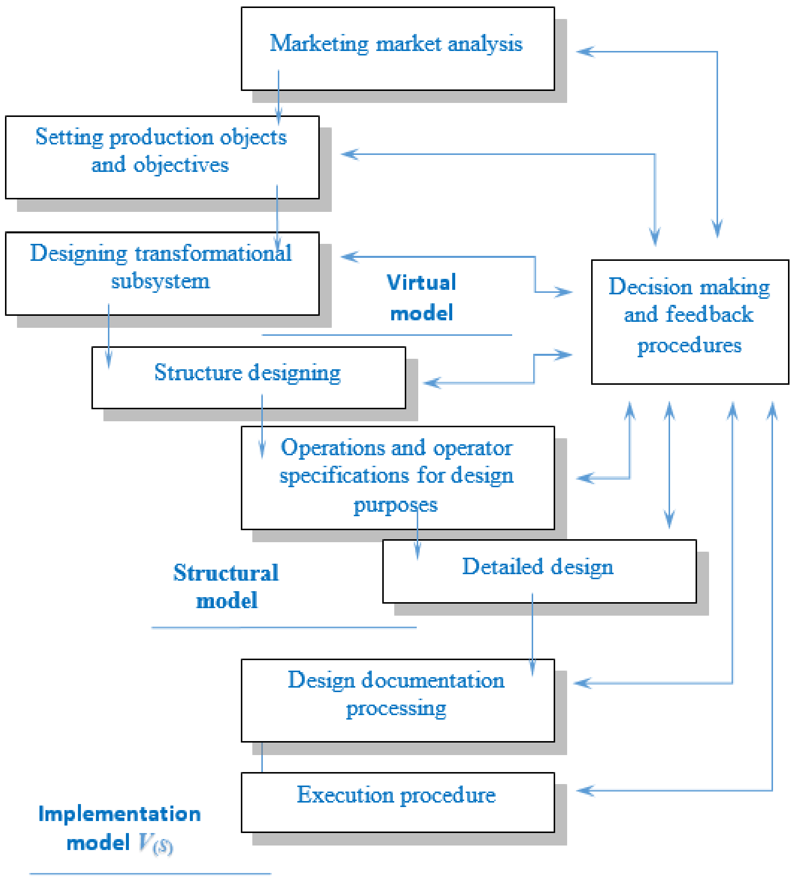

Fig. 1. The production system creation methodology

The importance of designing target functions in production systems stems from their diversity and the changes required in product manufacturing. The basic structuring of objectives results from the possibility of integrating production systems into higher system units. In the hierarchical understanding of production processes, the systems of greater complexity are superior to the systems of lower complexity. The implementation of superiority in the descending order of social, economic, production and internal goals can be recommended in case of full adoption of new production technologies and their implementation in practice.

4. Structure of production goals in production systems design

For the general development of social orientation of production, it is important that the priority of social goals and their quantitative assessment are not impaired in the stage of project preparation. Adding product value is necessitated by the increasing competition in the global market. This is achieved by shortening the innovative creation cycles and starting up new products, using new knowledge, customising the product to customer requirements through its modifications, short delivery times, etc.

Analyses of targets at the level of production systems are currently well outlined in terms of both scientific knowledge and design practice [2, 7, 10]. Definition of production goals such as productivity, production process continuity, stability, reliability, quality, etc. is known from the theory of production processes, and with some modifications, can be applied to the customer-oriented production. The basic structure of production goals in designing production systems is shown in figure 2:

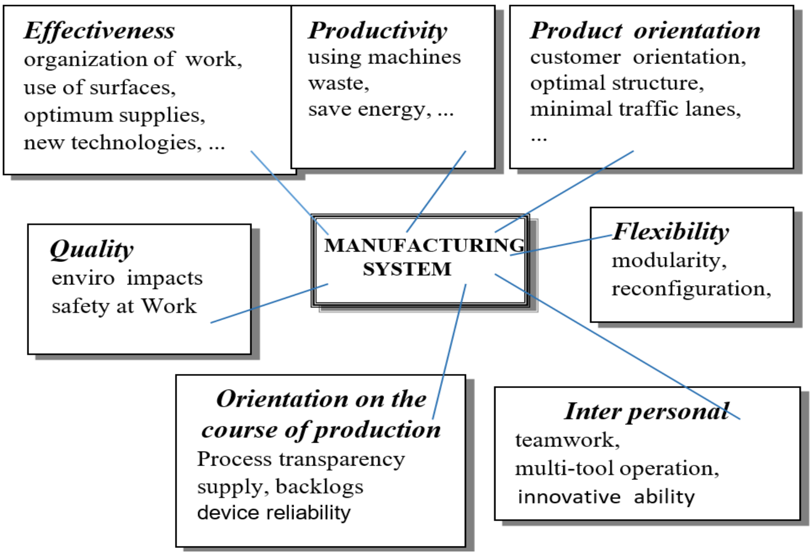

Fig. 2. Structure of production goals in production systems design

More significant differences in technical objectives V(S) may be caused during the process of determining the level of flexibility and automation. The priority of elasticity V(S) arises from its relation to the competitiveness of the production demonstrated by manufacturing products according to customer requirements [8, 10].

The analysis of constraints affecting the objects of manufacturing can be based on a progressive evaluation of the selection function:

$$R(b_i) = \begin{cases} 0 \\ 1 \end{cases} B = \{b_1,\ b_2\ ,\ \ldots,\ \ b_n\},$$

where:
R decisive selection function,
bi *i*-te constraint of V(S),
R(bi) = 0 - V(S) lacks the assumption of meeting the bi constraint,
R (bi) = 1 V(S) is assumed to meet the bi constraint,
n number of constraints considered.

It holds that the objects of production are suitable for V(S) if each R(bi) = 1 when i = 1, … n. In practice, it is expedient to arrange the sets of constraints in such a manner that lower index restrictions have greater negative value R(bi) probability. The objects of production are typically the source of the highest number of constraints.

The concept of the said system allows for the incorporation and use of previously developed design methodologies and procedures. The following activities are important for production:

- Profiling activities focused on objects of production, production processes and production system structures.
- Methods and techniques for creating and optimising methods and structures of manufacturing operations.
- Methods and techniques for synthesis of production systems – general method structures, construction and modernisation models, interface solutions, spatial problems solutions, material and information flows, etc.
- Implementation procedures and knowledge from experimental activities, following the theoretical and knowledge base of the area under study.

A material model may be represented by a machine-robot-product system, or a self-service machine the product. Another level in this hierarchy is achieved by adding control functions to the technological processing and handling system. In this way, a production module can be created as a system having the structure and parameters of technological, handling and control compatibility. It allows for the creation of production systems with their own structure and parameters. An important aspect, however, is the system compatibility between the technological, handling and control devices. The shape of the construction model is that of a pyramid (figure 3).

The design of production workstations, systems and clusters, taking into account specific technical and organisational and economic conditions, uses new methodological procedures and activity algorithms. In this process, valid regulations and classical design rules must be observed with respect to certain specific conditions, different methodological and algorithmic procedures [1, 10, 13]. From the content point of view, when designing manufacturing workstations, systems and clusters, it is necessary to ensure the processing of a set of functions according to their technical specifications.

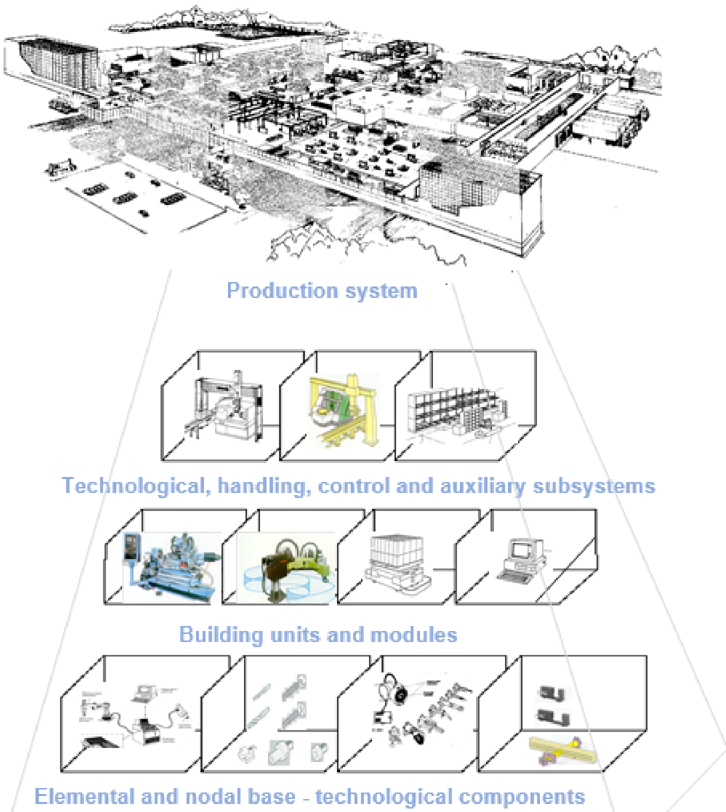

Fig. 3. The pyramidal structure of the production system creation

5. Conclusion

Design types of production workstations, systems and clusters are a significant reference solution that is applicable to the given manufacturing conditions, bringing benefits in the form of elimination of design shortcomings, in particular in terms of cost, time of preparation and implementation or in terms of competitiveness. Type-specific production workstations, systems and cluster designs must be expressed in the design documentation in such a way as to ensure the technical feasibility of their implementation under given conditions. Therefore, it is necessary to consider the clarity of the solution and its information completeness as an important factor in the design of the project documentation.

Production workstations, systems and clusters are made up of a number of elements and units of technological processing, operational and inter-operational handling and storage, control, interconnection and the like. At the same time, production workstations, systems and clusters generally include production units capable of executing a coherent part of the production process. Production systems can be grouped into more complex units (production departments, operations, plants) only if the following principle applies, i.e. that the number of their mutual relations is greater than the number of relations in entirety. The theory of clustering building elements and units of manufacturing workstations and systems is rooted in the principle of recurrent development elaborated in systemology. The base-level structure is homogeneous and is defined as an element. The next higher unit is made up of this element plus another element of the same or new quality. Thus, a complex, multi-level system can be gradually built this way.

The philosophy of innovative, varied, and interactive designing is based on the assumption that the production system solution takes place in three stages:

- An initial set of variants of the production system solution is proposed in accordance with the agreed objectives. Various methods for determining solution variants (analytical, morphological, hierarchical generation, use of reference solutions, etc.) can be used. For less complex tasks, intuitive ways of variant generation, based on reference type-specific patterns, can be used.
- Feasible solutions are defined. Inappropriate variants of the production system solution are excluded, either based on intuitive or logical and mathematical methods.
- The optimal variant of the production system solution is chosen in the final stage. The decision-making methods or optimisation criteria are applied. The optimal variant can be obtained as a result of comparative methods (reference projects), based on simulation activity, etc.

Segmentation can be accomplished in two basic ways: vertically – i.e. the vertical segmentation is based on individual types of the products manufactured, or horizontally – segments are formed horizontally within the vertical segments, i.e. the number of steps in the production process is reduced and so is the product complexity.

The choice of an optimal concept for the solution of the spatial structure of the production system is proposed based on the application of the methodological methods of production segmentation. Segmentation is a form of application of group principles to production, and in particular, it enables execution of the production systems' progressive cellular structures.

Acknowledgement

This work has been supported by the Scientific Grant Agency of the Ministry of Education of the Slovak Republic (Projects VEGA 1/0251/17 and KEGA 026EU-4/2018)

References

[1] N. Daneshjo, E. Danishjoo, "General Course of Failure Distributions at Complex Machineries", *TEM Journal*, vol. 6(1), pp. 17–21, 2017, https://doi.org/10.18421/TEM61-03.

[2] J. Kovač, V. Rudy, J. Kováč, "Methods for the design of production processes. Specifics of designing production systems. Edition of professional and scientific literature", Košice, p. 326, 2017.

[3] D. Plinta, M. Krajcovic, "Production system designing with the use of digital factory and augmented reality Technologies", *Advances in Intelligent Systems and Computing*, vol. 350, pp. 187–196, 2016.

[4] H. P. Wiendahl, J. Reichardt, P. Nyhuis, "Handbook Factory Planing", *Berlin Heidelberg: Springer-Verlag*, 2015.

[5] M. Buckova, M. Krajcovic, M. Edl, "Computer simulation and optimization of transport distances of order picking processes", *12th Internacional scientific conference of young scientists on sustainable, modern and safe transport Book Series: Procedia Engineering*, vol. 192, pp. 69–74, 2017.

[6] M. Hammer, "The Superefficient Company", *Harvard Business Review*, vol. 79(9), p. 84, 2001.

[7] T. E. Vollmann, W. L. Berry, D. C. Whybark, "Manufacturing Planning and Control Systems", *New York, NY: Irwin/McGraw-Hill*, 1997.

[8] P. Bubeník, E. Bubeníková, P. Korbel, P. Nagy, "Information Technology for Business Practice", *Žilina: Edis*, ŽU in Žilina, 2004.

[9] N. Daneshjo, K. Repková Štofková, L. Bednárová, M. Danishjoo, "Marketing and management information system and research system", *San Antonio, Texas, USA: FedEX Office Print & Ship Center, Huebner Oaks Center*, p.288, 2016.

[10] N. Daneshjo, V. Rudy, K. Repková Štofková, A. Mareš, J. Kováč, A. Jahnátek, J. Krivosudská, N. Šmajda, J. Rusnák, "Intelligent industrial engineering - innovation potential", *San Antonio Texas, USA: FedEx Print & Ship Center*, p. 297, 2018.

[11] J. Dobránsky, E. Ragan, N. Daneshjo, "Determination of technological parameters limit values on planned experiment, proposal for following products from thermoplastics qualitative parameters", *Engineering Review*, vol. 29(2), pp. 45–51, 2009.

[12] N. Daneshjo, M. Majernik, "Logistics of experimenting with strengthening the surface layers of machine parts", *Modern Machinery (MM) Science Journal*, vol. October, pp. 1178-1184, 2016, https://doi.org/10.17973/MMSJ.2016_10_201699.

[13] M. Kováč, J. Kováč, "Integrated Production", *Košice: ES VŠT*, 1990.

[14] J. Kováč, V. Rudy, J. Kováč, "Automation of production. Edition of scientific and professional literature", *Košice: SjF TU in Košice*, 2016.

[15] V. Modrák, "Contribution to Designing Structural Changes in Manufacturing Processes", *Košice: FTT TU in Košice*, 2001.

[16] A. Mareš, "Techniques for shortening the time of design of assembly processes and systems", *Košice: SjF TU in Košice*, 2006.